EPSC Abstracts
Vol. 10, EPSC2015-18, 2015
European Planetary Science Congress 2015

Titan's temporal evolution in stratospheric trace gases near the poles

A. Coustenis (1), D. Jennings (2), R. Achterberg (2, 3), G. Bampasidis (1, 4), P. Lavvas (5), C. Nixon (2), N. Teanby (6), C. Anderson (2), V. Cottini (2), F. M. Flasar (2)

(1) LESIA, Observatoire de Paris, CNRS, UPMC Univ. Paris 06, Univ. Paris-Diderot, 92195 Meudon, France, (athena.coustenis@obspm.fr, +33145077720), (2) NASA/Goddard Flight Center, Greenbelt, MD, USA, (3) Department of Astronomy, Univ. of Maryland, USA, (4) National & Kapodistrian University of Athens, Faculty of Phys., Astrophys., Astron. & Mech., Greece, (5) GSMA, Univ. Reims, France, (6) School Earth Sci., Univ. Bristol, UK

1. Context/Data

We analyze spectra acquired by the Cassini/Composite Infrared Spectrometer (CIRS) at high resolution from October 2010 until September 2014 in nadir mode. Up until mid 2012, Titan's Northern atmosphere exhibited the enriched chemical content found since the Voyager days (November 1980), with a peak around the Northern Spring Equinox (NSE) in 2009. Since then, we have observed the appearance at Titan's south pole of several trace species for the first time, such as HC_3N and C_6H_6, observed only at high northern latitudes before equinox. We investigate here latitudes poleward of 50°S and 50°N from 2010 (after the Southern Autumnal Equinox : SAE) until 2014.

2. Methodology

In this paper we extend previous work focusing on trace gases in Titan's stratosphere with emission signatures probing essentially the 100-400 km altitude range. We have been monitoring such emissions since the beginning of the Cassini mission in the focal plane 3 (FP3) of CIRS covering the spectral range from 600 to 1100 cm^{-1} (Coustenis et al., 2007, 2010, 2013; Bampasidis et al., 2012). Focal plane 4 (FP4) is used to extract the temperature profiles from the methane emission in the band centered at 1305 cm^{-1}. We use a radiative transfer code (ARTT) that we apply to CIRS spectral averages corresponding to data from flybys of Titan until 2013, binned over 10° in latitude for both medium (2.5 cm^{-1}) and higher (0.5 cm^{-1}) resolutions mostly from nadir observations. In analyzing the spectra, we search for variations in temperature and composition at northern (around 50°N), equatorial and southern (around 50°S) latitudes. Our code uses the most recent spectroscopic databases.

3. Results

The warming in the North from February until September 2014 is about 6 K, whereas at about the same period of time, the South has become another 12-15 K colder in the stratosphere, totaling about a 40 K drop in temperature within 4 years since 2010. The temperature profiles at 70°S for the period in time from 2010 to 2012 are compatible with those found by Achterberg et al. (2008, 2011) and Vinatier et al. (2015) from limb-viewing observations in the stratospheric region that we probe here and show again a decrease in temperature by about 10 K (Fig. 1). Similarly, their mid-latitude southern and northern profiles, as well as the thermal profiles close to 70°N do not exhibit large variations, as also found here and with compatible trends.

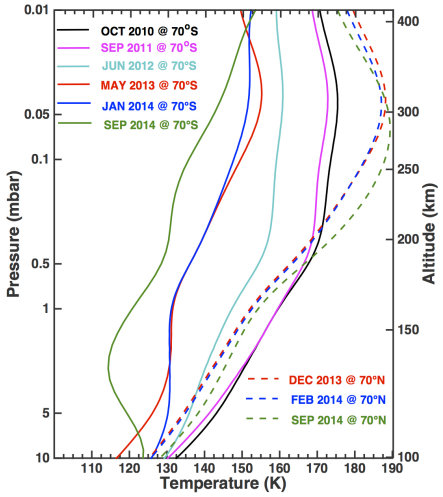

Figure 1: temperature variations in the South (From Coustenis et al., 2015)

For some of the most abundant and longest-lived hydrocarbons (C_2H_2, C_2H_6 and C_3H_8) and CO_2, the

evolution in the past 4 years at a given latitude is not very significant within error bars especially until mid-2013. In more recent dates, these molecules show a trend for increase in the south. This trend is dramatically more pronounced for the other trace species, especially in 2013-2014, and at 70°S relative to 50°S. These two regions then demonstrate that they are subject to different dynamical processes in and out of the polar vortex region. For most species, we find higher abundances at 50°N compared to 50°S, with the exception of C_3H_8, CO_2, C_6H_6 and HC_3N, which arrive at similar mixing ratios after mid-2013.

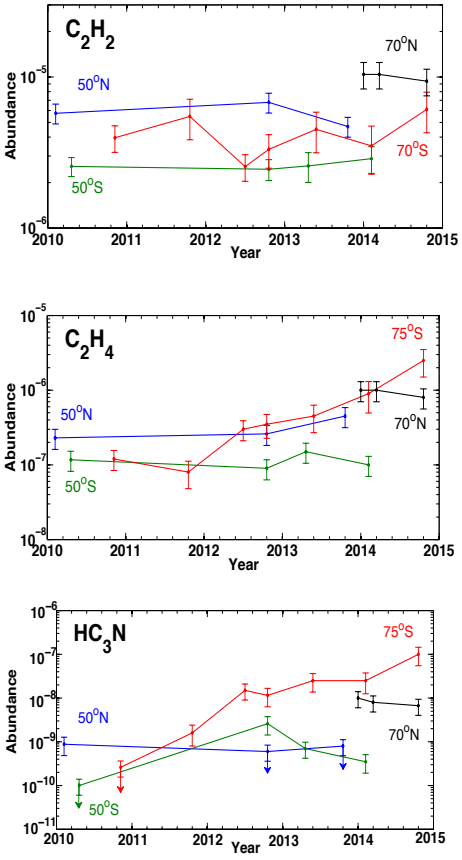

Figure 2: Examples of variations of the abundances of gases in Titan's stratosphere close to the south pole (adapted from Coustenis et al. 2015).

While the 70°N data show generally no change with a trend rather to a small decrease for most species within 2014, the 70°S results indicate a strong enhancement in trace stratospheric gases after 2012 (Fig. 2). The 663 cm^{-1} HC_3N and the C_6H_6 674 cm^{-1} emission bands appeared in late 2011/early 2012 in the south polar regions and have since then exhibited a dramatic increase in their abundances. At 70°S HC_3N, HCN and C_6H_6 have increased by 3 orders of magnitude over the past 3-4 years while other molecules, including C_2H_4, C_3H_4 and C_4H_2, have increased less sharply by 1-2 orders of magnitude). This is a strong indication of the rapid and sudden build-up of the gaseous inventory in the southern stratosphere during 2013-2014, as expected as the pole moves deeper into winter shadow. Subsidence gases that accumulate in the absence of ultraviolet sunlight, evidently increased quickly since 2012 and some of them may be responsible also for the reported haze decrease in the north and its appearance in the south at the same time (Jennings et al., 2012a,b).

The recent enhancement in gases and haze at the South Pole is probably the result of the seasonal reversal of atmospheric circulation (Teanby et al., 2012). While the situation at the equator seems stable, it needs monitoring at both poles.

Acknowledgements

The authors acknowledge the support of the ESA/NASA Cassini mission funds through the CNES program.

References

[1] Achterberg R., et al., Icarus, 211, 686-698, 2011.
[2] Bampasidis et al., ApJ 760, 144, 8 p., 2012.
[3] Coustenis, A., Bézard, B., Icarus,115, 126-140, 1995.
[4] Coustenis, A., et al., Icarus, 161, 383-403, 2003.
[5] Coustenis, A., et al., Icarus, 189, 35-62, 2007.
[6] Coustenis, A., et al., Icarus, 207, 461-476, 2010.
[7] Coustenis, A., et al., Astrophys., J. 799, 177, 9p., 2013.
[8] Coustenis, A., et al. Icarus, submitted, 2015.
[9] Jennings, D. E., Anderson, C. M., Samuelson, R. E., et al., ApJ, 754, L3, 2012a
[10] Jennings, D. E., Anderson, C. M., Samuelson, R. E., et al., ApJ 761, L15, 2012b
[11] Teanby, N., et al., Nature 491, 732-735. 2012.
[12] Vinatier et al., Icarus, 2015.

EPSC Abstracts
Vol. 10, EPSC2015-73, 2015
European Planetary Science Congress 2015

Two-face nature of cosmic bodies: saturnian satellites, Earth, Mars, the Moon, Ceres

Kochemasov G.G.
IGEM of the Russian Academy of Sciences, Moscow, kochem.36@mail.ru

These global color mosaics of Saturn's moons were produced from images taken by NASA's Cassini spacecraft during the first ten years exploring the Saturn system.*(Images credit: NASA/JPL-Caltech/Space Science Institute/Lunar and Planetary Institute).* The most obvious feature on the maps is the difference in color and brightness between the two hemispheres. The darker colors on the trailing hemispheres (on the left side of the images) are thought to be due to alteration by magnetospheric particles and radiation striking those surfaces. The lighter-colored leading hemispheres are coated with icy dust from Saturn's E-ring, formed from tiny particles ejected from Enceladus' south pole. These satellites are all, supposingly, being painted by material erupted by neighboring Enceladus.

Some corrections are necessary for these explanations. The first theorem of the wave planetology [1] states: "Cosmic bodies are dichotomous". This is due to warping action of the fundamental wave warping moving in keplerian orbits with periodically changing accelerations celestial bodies. All experience of cosmic explorations of numerous bodies shows that a two-face appearance or dichotomy really is their typical trait. Normally, the uplifted rugged hemisphere is opposed by the subsided relatively smoothed one. The best-studied examples are Earth, Mars, Ceres (Fig. 7) Thus, the painting action of Enceladus is an additional action superimposed on already existing tectonic dichotomy - an ubiquitous morphologic feature. It is true, that the source of tiny icy particles is Enceladus; that is why it is less color dichotomous (whitened) than other icy satellites (Fig. 1-6). Uplifted cracked and fissured (rugged) hemispheres often are darker - some lighter but darker under decomposition substance is coming up. This is not the case for Iapetus and probably for Enceladus degassing light toned material. Uplifted hemispheres are more rugged, cracked, and cratered than the opposite pressed in hemispheres. Normally pressing – diminishing radius is a reason for forming denser formations in these tectonic blocks (preserving angular momentum considerations; look at Earth, Mars). In the saturnian satellites cases darker substance could be less dense than water ice or presents very thin veneers originating from satellite depths due to very deep cracks (Diona, Rhea). In much more wave warped Iapetus the darker and presumably denser material already fills hemispheric depression. If the bright leading hemisphere explanation is acceptable for the nearest to Enceladus bodies (1, 3), it is not properly understood for the distant ones (4, 5, 6) where the brightness is even stronger. A soot covering the uplifted hemispheres is a possible explanation for the observations The soot originates under decomposition of light C-containing chemicals. The pressed in hemispheres could be filled with relatively dense salted water.

-	**Color maps of:**	**Radius, km:**	**Orbital period, days**
	1 - Mimas, PIA18437	197	0.94
	2 – Enceladus, PIA18435	251	1.37
	3 – Tethys, PIA18439	524	1.89
	4 - Diona, PIA18434	559	2.74
	5 – Rhea, PIA18438	765	4.52
	6 – Iapetus, PIA18436	718	79.33

Images credit: NASA/JPL-Caltech/Space Science Institute/Lunar and Planeetary Institutte

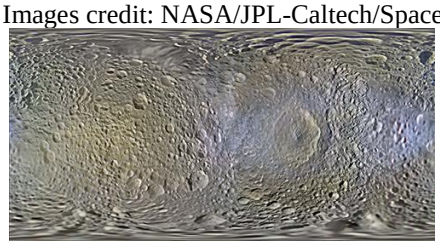
1 Mimas

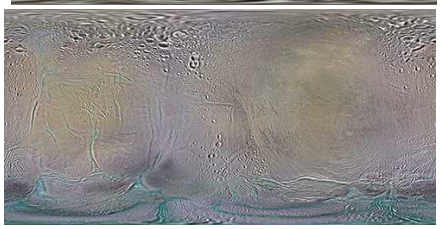
2 Enceladus

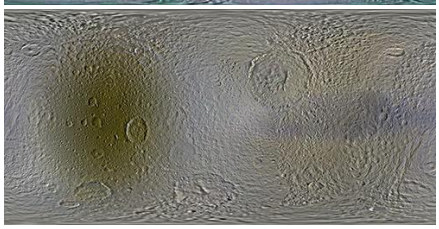
3 Tethys

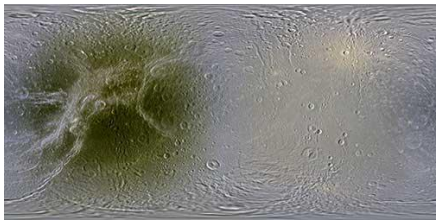
4 Diona

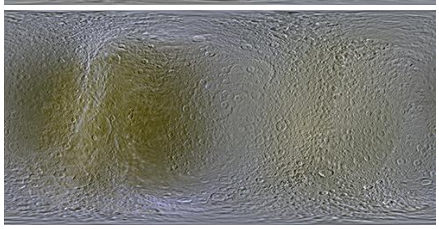
5 Rhea

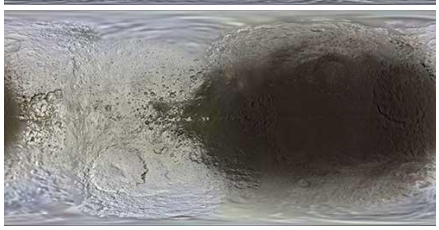
6 Iapetus

Fig.7. Ceres, pia19063_main.png

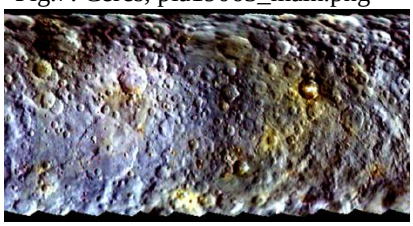

References: **[1]** Kochemasov G.G. (1999) Theorems of wave planetary tectonics // Geophys. Res. Abstr., v.1, #3, 700

EPSC Abstracts
Vol. 10, EPSC2015-76, 2015
European Planetary Science Congress 2015

The evidences of latitudinal asymmetry of the ammonia absorption on Saturn

V.Tejfel, A,Karimov, N.Bondarenko, G.Kharitonova
Fessenkov Astrophysical Institute, Almaty, Kazakhstan, (tejf@mail.ru)

Abstract

450 zonal CCD-spectrograms, recorded by scanning the disk of Saturn during its equinox at the beginning of 2009, were processed to find the variation of the absorption band of ammonia NH3 647 nm. This band overlaps with the short-wavelength wing of the absorption band of methane CH4 667 nm, therefore, to highlight the ammonia absorption spectra were used Uranus and laboratory spectra of methane. It was found that ammonia absorption is enhanced in the northern hemisphere of Saturn, as well as relatively weak bands of methane in contrast with stronger CH4 bands [1]. It may indicate on the North-South asymmetry in the density of the deeper parts of the ammonia cloud layer of Saturn .

1. Introduction

The ammonia absorption bands in the visible part of the spectrum of Saturn is much weaker than that in Jovian spectra (Figure 1). They overlap with bands of methane and the selection ammonia absorption so is quite complicated.

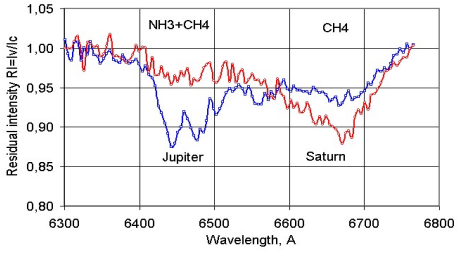

Figure 1: The absorption NH3+CH4 band in the spectra of Jupiter and Saturn

This research was directed to identify possible latitudinal variations of the NH3 absorption Saturn in the equinox 2009 period when both hemispheres of the planet are in equal conditions of lighting and visibility.

2. Observations and processing.

In early 2009 the observations of Saturn were carried out with 0.6-m telescope and diffraction spectrograph SGS . For one night 5-6.01.2009 at the Earth saturnocentric declination -0.8 deg there were recorded 5 series of zonal CCD-spectrograms by scanning the Saturn disk from the south pole to the north. Each scan consisted of 70 spectrograms, so that were received and processed 450 spectra corresponding all latitudinal zones of the planet (Figure 2). To extract the absorption band NH3 647 free of ammonia absorption spectra of Uranus, Saturn's rings were used as well as the calculations based on the laboratory spectra of methane absorption [2].

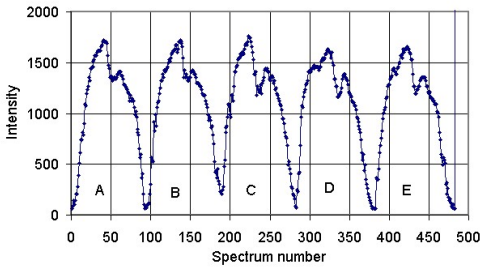

Figure 2: The intensity south-north profiles pf Saturn's spectral scans

.As a result of the spectrograms processing and analysis the atlases pf spectral ratios of individual zones of Saturn's disk to the region in the equatorial zone of the planet were prepared. We also calculated the pairwise spectra ratios for symmetric zones of the northern and southern hemispheres.

3. The hemispheric differences of the NH3 absorption

Analysis of all graphs atlas shows that absorption in the band NH3 647 nm is enhanced in the northern temperate latitudes in comparison with the southern temperate latitudes. Absorption of methane in relatively weak bands is also increased in the northern hemisphere, but, as shown in Figure 3, the ratio of residual intensities RI647 / RI675 in the northern temperate zone is some smaller than in the southern temperate zone. This means an increasing of the NH3 absorption in northern hemisphere.

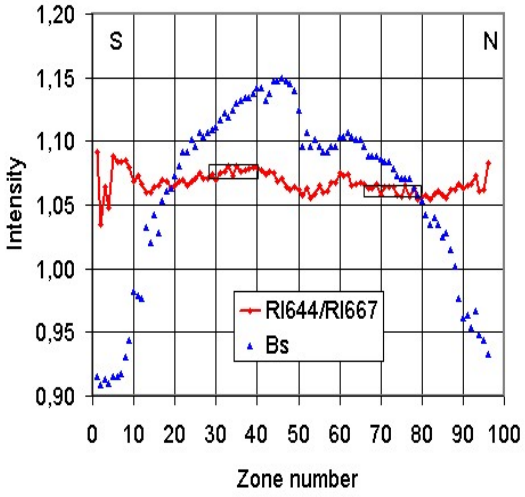

Figure 3: The ratio of residual intensities at 644 and 667 nm for Saturn's zones from South to North.

The ratio of latitudinally averagedon profiles of the absorption bands for the southern and northern hemispheres (RIn / RIs) shows the same result (Figure 4).Although the depth of the ammonia absorption band is considerably less than the depth of long-wave part of CH4 band, it is seen that this ratio for NH3 band indicates a greater difference than the ratio in the region of the pure methane absorption.

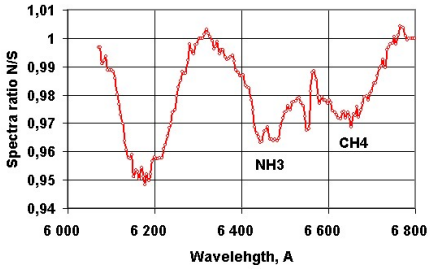

Figure 4: The ratio N/S for latitudinally averaged band profiles

4. Conclusion

The results show that the increased NH3 absorption in Saturn's northern hemisphere coincides with the increase of relatively weak CH4 absorption bands, observed also in the northern hemisphere. At the same time stronger absorption band of methane, for example, 725 nm band, the similar hemispheric difference is not detected. This may be due to a decrease of the volume density and the aerosol scattering coefficient on the large effective optical depths by raising the temperature. In the upper part of the cloud cover the difference in density of the cloud layer apparently absent or much less pronounced. The temperature measurements in the upper troposphere Saturn at the pressure of about 500 mb [3] shows a even decrease in the northern hemisphere, as compared with the south temperate latitudes.

References

[1]. Tejfel V.G. , Karimov A.M., Kharitonova G.A., Kirienko G.A ,Vdovichenko V.D. The hemispheric differences in the methane and ammonia absorptions on Saturn near last equinox in 2008-2010 .Bulletin AAS,Vol.. 42. - P.1021. , 2010

[2]. Dick, K. A.; Fink, U. Photoelectric absorption spectra of methane CH4, methane and hydrogen H2 mixtures, and ethane C2H6 J. Quant. Spectrosc. Radiat. Transfer, Vol.. 18, P. 433-446 ,1977.

[3]. Fletcher, L.N., Achterberg, R.K., Greathouse, T.K., Orton, G.S et al. Seasonal change on saturn from Cassini/CIRS observations, 2004–2009. Icarus, Vol.208 PP. 337–352, 2010.

EPSC Abstracts
Vol. 10, EPSC2015-82, 2015
European Planetary Science Congress 2015

The major circulations in Jupiter's North Tropical domain

John H. Rogers (1), Gianluigi Adamoli (2), Hans-Jörg Mettig (2), Michel Jacquesson (2), Marco Vedovato (2)
(1) British Astronomical Association, Burlington House, Piccadilly, London, UK; (2) JUPOS team.

1. Introduction

Jupiter's North Tropical domain covers the North Equatorial Belt (NEB: cyclonic) and North Tropical Zone (NTropZ: anticyclonic). Here we analyse ground-based amateur images from 1997 to 2015 with data from the JUPOS project, to describe the nature and behaviour of the major circulations therein, both cyclonic (dark brown ovals, called 'barges') and anticyclonic (white ovals, AWOs). Arrays of these circulations typically appear about a year after a NEB broadening event, which occurs every 3-5 years. Most of the circulations disappear between these cycles. The only one which has persisted through the whole period is a very bright AWO called White Spot Z (WSZ) [1].

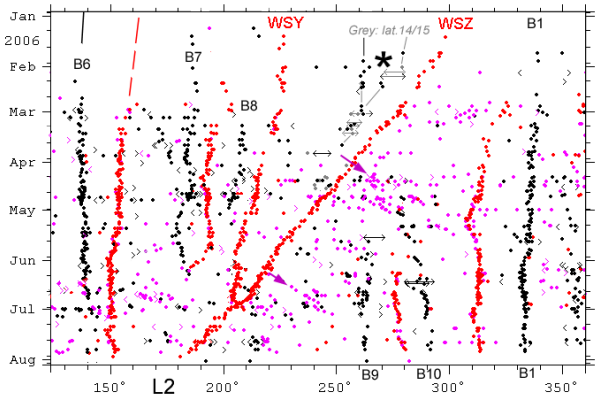

Figure 1. Excerpt from JUPOS chart of longitude vs time for N. Tropical spots. Red, white spots, lats.+18/+21 (AWOs); mauve, white spots, lats.+15/+18 (some on retrograde jet, arrowed); black, dark spots, lats.+15/+18 (barges). Note rapid drift of WSZ, its merger with WSY, merger of two small barges (asterisk), & origin of new barges among retrograding spots following WSZ.

2. White spot Z, the long-lived AWO

WSZ is a great AWO at 19ºN (Fig.2). But when the NEB is narrowed so that WSZ is in the N. Tropical Zone, its oval form is often obscured by a pale grey streak, whereas a tiny, bright white spot appears on its N edge. During the great NTBs jet outbreaks in 2007 and 2012, WSZ became dark grey.

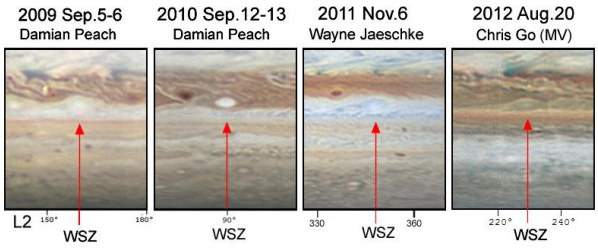

Figure 2. Views of WSZ, 2009-2012, from cylindrical-projection maps. The map labelled (MV) was made by Marco Vedovato. Note the variations in width of the NEB and in the appearance of WSZ. South is up in all figures.

WSZ almost always has a faster drift than other AWOs in the domain, and lies slightly further north. Its dominant nature is evident from its powerful effects on barges and AWOs that it approaches. In its early years, it eliminated other spots preceding it; later it more usually accelerated them to its own speed, 'pushing' them ahead of it and sometimes causing them to merge with other spots further ahead. After the great northern upheaval of 2012, it accelerated to an exceptionally rapid speed, and collided with an AWO preceding it in early 2013.

Six months later, WSZ had become strongly methane-bright, which is unprecedented for these AWOs. Then it gradually acquired a reddish tint, also unprecedented (first reported by C. Go), which persisted as the oval brightened in early 2014, though the colour remained weak. The colour and methane-brightness faded away again by early 2015. We suspect that the partial merger in 2013 intensified the circulation of WSZ, leading to a gradual thickening of its cloud cap, which then became reddish as well. Red colour is seen intermittently in the largest and longest-lived anticyclonic ovals in several domains on Jupiter [2], including oval BA which reddened 6 years after forming by a triple merger, and some seen historical-ly in the same latitude as WSZ, so WSZ could in future become a Little Red Spot.

3. Zonal drift profile and zonal wind profile

The variation of east-west speed with latitude has been plotted for defined spots (Zonal Drift Profile, ZDP, from ground-based observations) and for small-

scale cloud textures (Zonal Wind Profile, ZWP, from spacecraft). As in most domains, the ZDP coincides with the ZWP for prograding speeds but is systematically 'blunter' for retrograding speeds, i.e. the barges and AWOs are only partially entrained by the NEBn retrograde jet. The full speed of the NEBn retrograde jet is only occasionally detected (Fig.3). It was detected in 2006, following WSZ and following a rifted region, where it probably comprised a disturbed wake; and in 2011/12 when the NEB was fading, perhaps allowing the jet to be more visible in the absence of confounding disturbance around it.

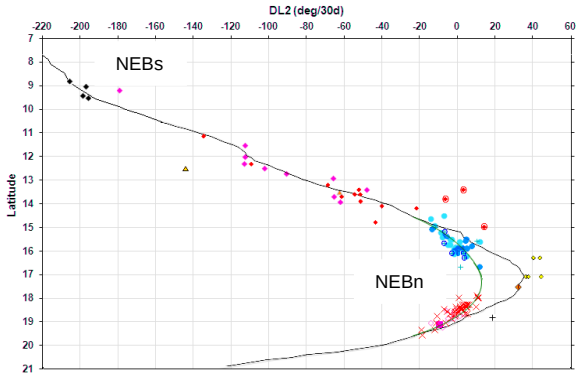

Figure 3. Zonal Drift Profile for NEB, 2005 and 2006, with the Cassini ZWP for comparison. Red symbols: bright spots; blue symbols: dark spots. The ZDP (green curve) diverges from the ZWP at positive (retrograding) drift values.

4. Origins of barges

New barges and AWOs appear circum-globally after a NEB broadening event, and more locally in the sector following WSZ, and sometimes in the wake of a turbulent cyclonic sector ('rift'). It is conjectured that they arise from instability of the NEBn retrograding jet. In 2006, small spots were visible in the NEBn jet up to 30-40° following WSZ, and at that point, new barges and AWOs were appearing. One such barge was observed forming from successive retrograding dark brown streaks. These were probably ripples on the retrograding jet, perhaps forming where the speed or turbulence of the jet dropped below a critical value, and amplifying into an eddy. Eventually, as the incipient circulation drifted beyond the end of the wake, it became a stable barge. More commonly, new barges just appear imperceptibly within the turbulence of the NEB, but the process observed in 2006 could be operating on a smaller scale.

5. Collisions between pairs of ovals

Mergers between barges are quite common. The first three were described in [3]. Others have occurred since [4], and typically followed much the same course, with the two barges in slightly different latitudes sliding together with initial overshoot but without obvious disturbance, although sometimes a small white spot appeared briefly.

Collisions of WSZ with other AWOs have occurred in 2006 (twice) and in 2012/13, always when WSZ was moving exceptionally fast. We have also recorded 5 collisions between other pairs of N. Tropical AWOs [1]. In the well-observed cases, there is only a partial merger. The leading oval ('A') shrinks as it squeezes along the S edge of the following oval ('B'); then they usually can be seen to spiral together, but only partially; in every case, part of oval A continues or re-emerges following the surviving oval B, as a slow-moving small white cloud which only lasts for a few days or weeks before disappearing. The surviving oval sometimes shows signs of instability or methane-brightness in the days during and after the interaction. Although the mergers appear to be incomplete, the observations do not constrain how much of the energy and vorticity of oval A is transferred to the surviving oval B.

Acknowledgements

Thanks are due to all observers, who are listed on the JUPOS website (http://jupos.org) and in our final apparition reports. This study exemplifies the contributions which amateurs can make in support of the JUNO mission.

References

[1] Rogers J.: 'White spot Z: its history and characteristics, 1997-2013.'
http://www.britastro.org/jupiter/2013_14report03.htm

[2] Rogers J.H., Adamoli G. & Mettig H-J.: 'Jupiter's high-latitude storms: A Little Red Spot tracked through a jovian year.' J.Brit. Astron.Assoc. vol. 121, pp.19-29; 2011.

[3] Rogers J.H., Mettig H-J., Cidadão A., Sherrod P.C., and Peach D.: 'Merging circulations on Jupiter: observed differences between cyclonic and anticyclonic mergers.' Icarus vol. 185, pp.244-257; 2006.

[4] Rogers J.H.: 'Interim report on Jupiter, 2012 Aug-Dec: Appendix 2: NEBn: Dynamic interactions of spots.'
http://www.britastro.org/jupiter/2012_13report09.htm

EPSC Abstracts
Vol. 10, EPSC2015-89, 2015
European Planetary Science Congress 2015

Seasonal evolution of tropospheric H_2 on Titan from the Cassini CIRS investigation

R. Courtin and the CIRS Team
LESIA, CNRS – Observatoire de Paris, Meudon, France (regis.courtin@obspm.fr)

Abstract

Far-infrared Titan spectra obtained with the Composite Infra-Red Spectrometer on the Cassini spacecraft have been analyzed to study the latitude distribution of H_2 in the troposphere, as well as its temporal evolution over the period from March 2007 to August 2014. This analysis shows that the previously observed distribution, characterized by a 30%-70% enhancement at high Northern latitudes, has become more symmetrical since Equinox. Hence, the reversed pole-to-pole Hadley cell circulation established shortly after Equinox has been effective in equilibrating the H_2 mole fraction in both polar regions, although not effective enough to produce a reversal of the polar enhancements probably because of a long time constant for the transport of air masses from the stratosphere to the troposhere.

1. Introduction

Earlier in the Cassini orbital mission, measurements obtained between March 2006 and February 2007 with the CIRS instrument on Cassini revealed that the tropospheric H_2 mole fraction was enhanced by 30%-70% at high Northern latitudes compared to the global mean value of 0.1% [1]. Based on the vertical profile of H_2 inferred from the tropospheric and thermospheric mole fractions [2] and the dynamics associated with the Titan atmospheric circulation [3, 4], it was concluded that the North polar enhancement was the result of transport of H_2-rich stratospheric air masses down to the tropospheric levels by the descending branch of the pole-to-pole Hadley cell located over the North pole during Northern winter.

Additional CIRS measurements acquired from March 2007 until August 2014 have been analyzed to study the evolution of that previously-observed latitude distribution across the Equinox epoch, when a reversal of the pole-to-pole Hadley cell circulation was expected, and indeed observed.

2. The CIRS data set in 2007-2014

We have selected a total of 43,640 CIRS spectra measured at a resolution of 2.5 cm^{-1} with the FP1 focal plane operating in the 10-600 cm^{-1} range. These data were separated into three periods: P1 from March 2007 to June 2009 (21,638); P2 from July 2009 to Feb. 2011 (5297); and P3 from Dec. 2011 to Aug. 2014 (16,705), corresponding to the Titan targeted encounters T25-to-T57, T58-to-T74, and T78-to-T104, respectively. Furthermore, the data were binned into appropriate latitude bins: 8 bins for P1; 4 bins for P2, and 10 bins for P3.

3. Results

From each selection of spectra, the H_2 mole fraction was determined by fitting the observed contrast of the H_2-N_2 dimer feature S(0) centred at 355 cm^{-1}. In a first step, a global mean was derived for each time period for the sake of comparison with that determined earlier in the mission. These values are respectively $(0.96\pm0.14)\times10^{-3}$ (P1), $(0.87\pm0.30)\times10^{-3}$ (P2), and $(1.14\pm0.25)\times10^{-3}$ (P3), in good agreement with the earlier value of $(0.96\pm0.24)\times10^{-3}$ [1].

The latitude distributions of H_2 derived for the three time periods, and that derived earlier in the mission (P0) are shown in Figure 1.

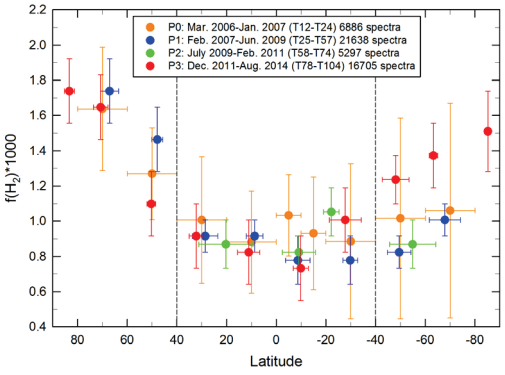

Figure 1: Latitude distribution of H_2 in four different periods extending from March 2006 to August 2014.

Only the data selections obtained in periods P0, P1, and P3 contain spectra measured at high latitudes. However, the results of Figure 1 reveal that the previously-observed enhancement over the North polar latitudes has not evolved significantly, whereas a similar enhancement has appeared over the South polar regions, making the overall latitude distribution more symmetrical with respect to the equator.

Hence, the reversed pole-to-pole Hadley cell circulation established shortly after Equinox has been somewhat effective in equilibrating the H_2 mole fraction in both polar regions. But contrary to what is observed in the case of several minor species, notably hydrocarbons and nitriles, the magnitude of the H_2 enhancement in the South is all but dramatic. This is probably due to the long time it takes to transport upper stratospheric H_2-rich air masses to tropospheric levels where the CIRS measurements are relevant, i.e. in the 0-30 km altitude range.

4. Summary and Conclusions

Titan far-infrared spectra obtained with the CIRS instrument between March 2006 and August 2014 show that the latitude distribution of tropospheric H_2 has evolved from a pre-Equinox situation characterized by a North polar enhancement to a more symmetrical one with enhancements in both polar regions, whereas the low- and mid-latitude regions do not show any significant variation.

These results tend to confirm the influence of the pole-to-pole Hadley cell circulation that affects the latitude distributions of most minor species on Titan. The reversal of that circulation shortly after Equinox is the most probable cause of the more symmetrical pattern observed for H_2, although the more subdued increase now observed in the South would imply longer time constants than for hydrocarbons and nitriles. Over the long term, such a characterization of the seasonal evolution of all minor species will certainly bring more insights into the temporal aspects of the atmospheric dynamics on Titan.

References

[1] Courtin, R., Sim, C. K., Kim, S. J., and Gautier, D.: The abundance of H_2 in Titan's troposphere from the Cassini CIRS investigation, Planetary and Space Science, Vol. 69, pp. 89–99, 2012.

[2] Strobel, D. F.: Molecular hydrogen in Titan's atmosphere: Implications of the measured tropospheric and thermospheric mole fractions, Icarus, Vol. 208, pp. 878–886, 2010.

[3] Hourdin, F., Talagrand, O., Sadourny, R., Courtin, R., Gautier, D., and McKay, C.P.: Numerical simulation of the general circulation of the atmosphere of Titan, Icarus, Vol. 117, 358–374, 1995.

[4] Hourdin, F., Lebonnois, S., Luz, D., and Rannou, P., Titan's stratospheric composition driven by condensation and dynamics, Journal of Geophysical Research, Vol. 109, E12005, 2004.

EPSC Abstracts
Vol. 10, EPSC2015-101, 2015
European Planetary Science Congress 2015

Thermal anomaly on Mimas surface: Implications on its regolith structure

C. Ferrari and A. Lucas
Laboratoire AIM Paris-Saclay, Université Paris-Diderot CEA/Irfu CNRS/INSU, F-91191 Gif-sur-Yvette

Abstract

Thanks to the Cassini CIRS infrared spectrometer, Howett et al. [1] have discovered a large scale thermal anomaly on the surface of Saturn satellite Mimas. This anomaly translates into a dichotomy in thermal inertia between leading and trailing faces of this synchronous icy satellite: the leading face (region R_2) exhibits a high thermal inertia, $\Gamma = 66 \pm 23$ J/m^2/K/s$^{1/2}$, compared to the trailing one (region R_1), where $\Gamma < 16$ J/m^2/K/s$^{1/2}$. The pattern appears to be well correlated with a color anomaly (Schenk et al. [2]) in visible light, also observed on other Saturn moons. It may be due to the alteration of their leading face by a focused bombardment of highly energetic electrons. This is thought to increase the contact between regolith grains by gluing them, improving thus the thermal conductivity or decreasing porosity.

We wish here to interpret this dichotomy as a change in porosity p or in grain size R of the upper layers of a porous regolith of icy grains. The thermal model developped in this purpose includes heat transfer by conduction through the solid phase and contacts and by radiation through the pores, both processes happening in parallel. The solid conduction is limited by the reduced area of contacts between grains, so that the effective conductivity K_S of the regolith is much smaller than the bulk conductivity of grains, K_B, and may become, even at low temperatures (T~80-100K), comparable to the radiative conductivity K_R. We test analytical models currently used in the field to express the relationship between conductivities, grain size R and porosity p. The thermal inertia writes as:

$$\Gamma(T,p,R) = \sqrt{(K_S + K_R)(1-p)\rho_0 C(T)} \quad (1)$$

We combine and compare expressions proposed by Breitbach and Barthels [3] or Gundlach and Blum [4] for K_R and models of contact conductivities by Gundlach and Blum [4], Gusarov et al. [5] or Johnson [6] for K_S.

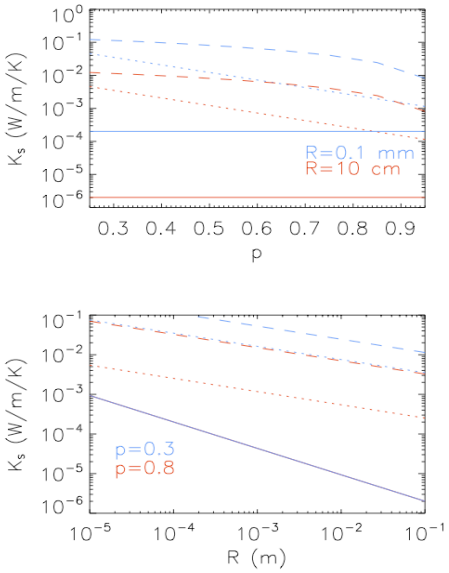

Figure 1 – Effective solid conductivity K_S of an icy regolith at T=80K (**Top**) as a function of porosity p & size R from Johnson ([6], full line), Gundlach and Blum ([4], dot line) and Gusarov et al. ([5], dashed line) models. (**Bottom**) As a function of grain size R.

The effective solid conductivity K_S is expressed as a function of both Hertz factor h and factor ϕ, which translates the influence of the porosity p, i.e. $K_S = h\phi K_B$. The effective conductivity K_S estimated by [4] is, at low porosity, at least 2-to-4 orders of magnitude larger than Johnson theory [6], of the order of 0.01 to 0.1 W/m/K (Fig. 1). At larger porosities, this difference scales down to 1-to-2 orders of magnitude, about 0.001 W/m/K. Johnson [6] provides a conductivity independent of porosity p, decreasing with $R^{-2/3}$ instead of $R^{-1/3}$ for the other two, which remain close and mainly differ in their dependence to the porosity.

The radiative conductivity K_R scales linearly with grain size, i.e. $K_R = 8RF_E\sigma T^3$ where F_E is an exchange factor and σ the Stefan constant. The temperature dependence of mechanical and thermal properties of water ice is included. It increases with porosity, as a higher fraction of pores favours radiative transfer. For 10-cm-sized particles it ranges between about 0.01 W/m/K for p=0.3 and 0.4 W/m/K for p=0.9 at T=80K. The Gundlach and Blum's estimation is more sensitive to porosity than Breitbach and Bartels'one but both exhibit similar trend with porosity. The heat transfer is found to be radiative for grains larger than a few mm whereas solid conduction dominates for smaller ones.

Finally a Monte-Carlo approach is coupled with the thermal model to infer plausible values for p and R in both R_1 and R_2 regions, given their thermal inertias. Three typical solutions appear while combining the different models (Figure 3):

- either grains in both regions are sub-cm-sized and regoliths differ in porosities, >80% for R_1 and <60% in R_2 and solid conductivity dominates (Figure 3, top),
- or R_1 & R_2 regions differ in grain size, R_1 being very porous but still dominated by solid conduction between sub-cm grains, while R_2 is dominated by radiative conduction between large grains, with a porosity hard to constrain (Fig. 3, top),
- or the conductivity by contact is very low ([6], Fig. 3, bottom), heat transfer is mainly radiative, the effect of size is dominant over porosity, both regions differ because of grain sizes, the grains in the bombarded region being cm-sized compared to sub-mm sized grain in the trailing R_1 region.

We intend to study CIRS data in detail to take into account actual temperatures or diurnal temperature transient regimes and possibly constrained more strictly regolith properties of both regions.

Acknowledgements

This work is supported by CNES National Space Agnecy and Commissariat à l'Energie Atomique et aux Energies Alternatives (CEA).

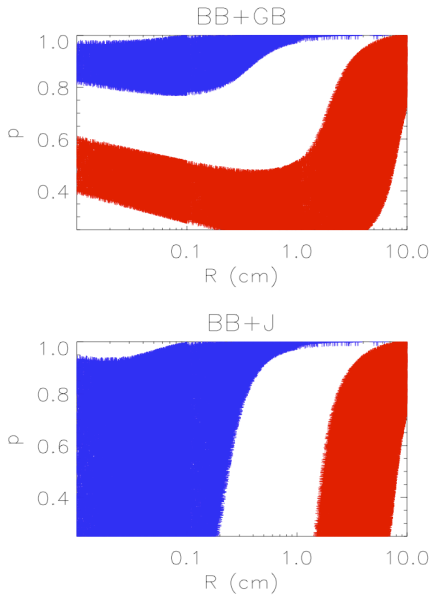

Figure 3 – Typical constraints on porosity p and grain size R for the leading face (R_2, red) and the trailing face (R_1, blue) of Mimas given their thermal inertias: **(Top)** assuming [3] for K_R and [4] for K_S **(bottom)** or [6] for K_S.

References

[1] Howett, C. et al., 2011. A high-amplitude thermal inertia anomaly of probable magnetospheric origin on Saturn's moon Mimas. Icarus, 216, 221-226.
[2] Schenk, P., et al. 2011. Plasma, plumes and rings: Saturn system dynamics as recorded in global color patterns on its midsize icy satellites. Icarus 211, 740–757.
[3] Breitbach, G., Barthels, H., 1980. The radiant heat transfer in the high temperature reactor core after failure of the after heat removal systems. Nucl. Technol. 49, 392–399.
[4] Gundlach,B., Blum, J., 2012. Outgassing of icy bodies in the Solar System - II: Heat transport in dry porous surface dust layers. Icarus 219, 618-629.
[5] Gusarov, A.V., et al. 2003. Contact thermal conductivity of a powder bed in selective laser sintering. Int. J. of Heat and Mass Transfer, 46, 1103-1109.
[6] Johnson, K. L., 1985. Contact Mechanics. Cambridge University Press, Cambridge.

EPSC Abstracts
Vol. 10, EPSC2015-104, 2015
European Planetary Science Congress 2015

Consequences of large impacts on Enceladus' core shape

J. Monteux (1), G.S. Collins (2), G. Tobie (3) and G. Choblet (3)
(1) Laboratoire Magmas et Volcans, Université Blaise Pascal, CNRS, IRD, Clermont-Ferrand, France, (2) Impacts and Astromaterials Research Centre, Department of Earth Science and Engineering, Imperial College London, (3) Laboratoire de Planétologie et de Géodynamique, CNRS, Nantes, France (j.monteux@opgc.univ-bpclermont.fr)

Abstract

The intense activity on Enceladus suggests a differentiated interior consisting of a rocky core, an internal ocean and an icy mantle. However, topography and gravity data suggests large heterogeneity in the interior, possibly related to significant core topography. In the present study, we investigated the consequences of collisions with large impactors on the core shape. We performed impact simulations using the code iSALE2D considering large differentiated impactors with radius ranging between 25 and 100 km and impact velocities ranging between 0.24 to 2.4 km/s, which are representative of impact events during the end of Enceladus' accretion. Our results show that if enough energy is available, part of the Enceladus' core is excavated which leads to a negative topography anomaly surrounded by a small positive anomaly. Among the icy mantle and the rocky core porosities, only the second one influences the post-impact rocky core shape. However, its influence as well as the influence of a thick sub-surface water ocean is less significant compared to the impact velocity or the impactor radius. Hence, constraining precisely the rocky core morphology is more likely to inform on the late accretionary conditions (i.e. impact velocity and impactor size) than on the internal structure and mechanical behaviour of Enceladus.

1. Introduction

Despite its small size (R=252 km), Saturn's moon Enceladus is one of the most geologically active body of the Solar System. This activity, concentrated at the south pole [1], implies a warm interior, consistent with a liquid water layer underneath the ice shell and a differentiated interior [2, 3]. The global shape data show a depression at the south pole [4]. It has been proposed that the dichotomy between the north and south hemispheres may be the result of asymmetry in core shape [5]. [5] proposed three hypotheses to explain the possible irregularity of Enceladus' rocky core: accretional melting of the outer region of the icy moon associated with the degree-one instability; accretion of icy protomoons around irregular rock chunks; and collisional merger of two previously differentiated protomoons. Here we test the latter hypothesis by investigating the consequences of the collision of a large differentiated impactor on the shape of Enceladus' core.

2. Impact modeling

To constrain the consequences of large-scale impacts on Enceladus, we simulated head-on collisions of differentiated impactors with size ranging between 50 and 200 km using the iSALE2D shock physics code [6]. From these simulations, we tracked the evolution of rock fragments coming from the impactor and the impact-induced modification of Enceladus's core shape. In particular, we quantified the sensitivity in these outcomes to key model parameters, such as impactor velocity and radius, as well as structure and mechanical properties of Enceladus' interior (porosity, strength, temperature profile, core size, presence of an internal ocean).

3. Results

Fig. 1 shows characteristic simulations with (vimp=10 vesc, Rimp=25 km), (vimp=10 vesc, Rimp=75 km) and (vimp= vesc, Rimp=75 km). After such events, a large volume of Enceladus' mantle is displaced or escapes the orbit of the icy moon. To get a quantitative measure of deformation induced by the impact event, we monitor the plastic strain experienced by the impacted material. As represented in Fig. 1, the icy material is highly disturbed by the impact and most of the plastic deformation occurs in this layer. For the largest impact velocities (Fig. 1, left and middle), deformation also occurs at the top of the rocky core and leads to the formation of a depression. The material removed from the depression is displaced in a very small

uplift of the core, surrounding the depression.

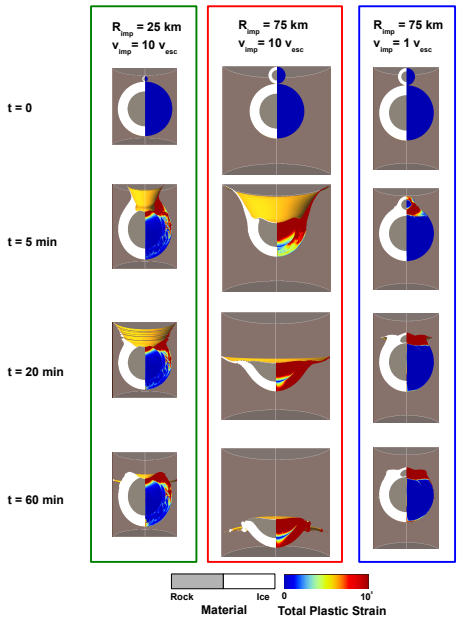

Figure 1: Material repartition (left column) and total plastic deformation (right column) as a function of time (from top to bottom) on Enceladus for 3 impact cases: (vimp=10 vesc, Rimp=25 km), (left), (vimp=10 vesc, Rimp=75 km) (centre) and (vimp= vesc, Rimp=75 km) (right)

We have used numerical impact simulations to examine the behaviour of an Enceladus' rocky core after an impact with a differentiated proto-moon with size ratios ranging between 0.1 and 0.4 and impact velocities ranging between 0.24 to 2.4 km/s. Our results show that depending on these two impact parameters, the post-impact shape of the target body's rocky core can exhibit negative or positive topographical features. If enough energy is available, part of the Enceladus' core is excavated which leads to a negative topography anomaly surrounded by a small positive anomaly. Otherwise the impactor's core spreads above the target body's core and leads to a positive topographic anomaly. Ultimately, for impactors larger than 150 km and/or impact velocities $\geq$ 10 vesc, the target body's core is disrupted and a substantial part of the icy mantle is irreversibly removed from the icy moon.

Among the icy mantle and the rocky core porosities, only the second one influences the post-impact rocky core shape. However, its influence is less significant compared to the impact velocity or the impactor radius. This conclusion also stands for the minimum strength of the impacted material. On the contrary, the presence of a thick sub-surface water ocean tends to reduce deformation of the rocky core during the impact.

4. Conclusions

Constraining precisely the rocky core morphology is more likely to inform on the late accretionary conditions (i.e. impact velocity and impactor size) than on the internal structure and mechanical behaviour of Enceladus. For a better comprehension of the post-impact rocky core shape, more sophisticated (i.e. 3D) simulations are required to include the impact angle effect.

Acknowledgements

We gratefully acknowledge the developers of iSALE, including Kai Wünnemann, Boris Ivanov, Jay Melosh, and Dirk Elbeshausen. We also thank Katarina Miljkovich and Tom Davison for useful discussions.

References

[1] Tobie, G., O. Cadek, and C. Sotin: Solid tidal friction above a liquid water reservoir as the origin of the south pole hotspot on Enceladus, Icarus, 196, 642-652, 2008.

[2] Nimmo, F., J. R. Spencer, R. T. Pappalardo, and M. E. Mullen : Shear heating as the origin of the plumes and heat flux on Enceladus, Nature, 447, 289-291, 2007.

[3] Schubert, G., J. D. Anderson, B. J. Travis, and J. Palguta: Enceladus: Present internal structure and differentiation by early and long-term radiogenic heating, Icarus, 188, 345-355, 2007.

[4] Thomas, P. C., J. A. Burns, P. Helfenstein, S. Squyres, J. Veverka, C. Porco, E. P. Turtle, A. McEwen, T. Denk, B. Giese, T. Roatsch, T. V. Johnson, and R. A. Jacobson: Shapes of the saturnian icy satellites and their significance, Icarus, 190, 573-584, 2007.

[5] McKinnon, W. B.: The shape of Enceladus as explained by an irregular core: Implications for gravity, libration, and survival of its subsurface ocean, Journal of Geophysical Research (Planets), 118, 1775−1788, 2013.

[6] Collins, G. S., H. J. Melosh, and B. A. Ivanov: Modeling damage and deformation in impact simulations, Meteoritics and Planetary Science, 39, 217-231, 2004.

EPSC Abstracts
Vol. 10, EPSC2015-109, 2015
European Planetary Science Congress 2015

Temporal evolution of Saturn lightning activity during Saturn's change of season in spring equinox 2009

Joseph Ambrose Pagaran and Georg Fischer
Institute of Physics, University of Graz, Graz, Austria (joseph.pagaran@uni-graz.at)

Abstract

Saturn Electrostatic Discharges or SEDs are measured by the Cassini/RPWS (Radio and Plasma Wave Science) instrument from 1 to 16 MHz. In August 2009, Saturn's northern (southern) hemisphere enters spring (autumn) 7-year-long season. The RPWS instrument, has so far recorded more than a dozen storms since the spacecraft's orbital insertion in 2004. Lasting for several months, each storm consisted of episodes with a periodicity lasting close to one Saturn rotation (about 10 hours and 40 minutes), which start/stop when the SED cloud enters/leaves the radio horizon.

Many of these SED storms raged at 35° South, dubbed the storm alley. The true temporal evolution of Saturn lightning rates is influenced by observational parameters like spacecraft distance and attitude, antenna choice and RPWS receiver modes with different integration times. In this contribution, we describe two methods to obtain the temporal evolution of Saturn lightning flashes in all SEDs episodes from the end of the year 2007 (Storm F) to the middle of the year 2010 (Storm I). The first method (denoted by *I*) determines the 'true' number of SEDs above a selected threshold of 0.8 dB using a normalization procedure [3] that is based on the spacecraft distance and on the RPWS receiver survey mode regardless of different integration times, attitude, antenna choice, etc. The second method (denoted by *II*) estimates the total number of SEDs and validates the 'true' number of SEDs obtained from the first method. The latter method, *II*, uses generalized extreme-value distribution (EVD) functions to find the best-fit EVD to intensity distribution [3] of each SED episodes observed during the Cassini equinox mission (2007-2010). The extracted SEDs using the computer algorithm of [1] can be seen as extreme events above a threshold.

We discuss the following issues. (1) The temporal evolution in smaller scale of weeks to months to larger scale of years. (2) How the normalized intensity (flash rates) determined from the first method, method *I*, are varying in the course of the storm. (3) Whether the total number of SEDs determined from the second method, method *II*, shows a hidden periodicity in it, and if there are dynamical processes in a thunderstorm deep in Saturn's atmosphere that could be somewhat regular or not; (4) We propose the total number of SEDs from second method, method *II*, as an independent measure (from observational parameters) for the activity of Saturn lightning. (5) Using planetary comparative meteorology, we briefly explain the temporal evolution of the derived lightning flash number on Saturn in terms of lightning on Earth.

Acknowledgements

Support from the Austrian Science Fund, FWF project P24325-N16 grant, is gratefully acknowledged.

References

[1] Fischer, G., M. D. Desch, P. Zarka, M. L. Kaiser, D. A. Gurnett, W. S. Kurth, W. Macher, H. O. Rucker, A. Lecacheux, W. M. Farrell, and B. Cecconi, Saturn lightning recorded by Cassini/RPWS in 2004, *Icarus*, *183*, 135–152, 2006.

[2] Pagaran, J.A. and G. Fischer, Saturn lightning recorded by Cassini/RPWS from high-inclination orbits in 2009, EGU General Assembly Conference (EGU) Abstracts, Vol. 15, EGU2013-3232, Vienna, Austria, 2013.

[3] Pagaran, J.A. and G. Fischer, Tail fitting the intensity distribution of selected Saturnian lightning storm episodes, European Planetary Science Congress (EPSC) Abstracts, Vol. 9, EPSC2014-796, Cascais, Portugal, 2014.

EPSC Abstracts
Vol. 10, EPSC2015-124, 2015
European Planetary Science Congress 2015

Hot N_2 in Titan's upper atmosphere

P. Lavvas (1), R.V. Yelle (2), A. Heays (3), L. Campbell (4), M.J. Brunger (4,5), M. Galand (6), and V. Vuitton (7)
(1) Groupe de Spectroscopie Moléculaire et Atmosphérique, Université de Reims, Champagne-Ardenne, CNRS UMR 7331, France, (2) Lunar and Planetary Laboratory, University of Arizona, 1629 E University Blvd, 85723,AZ, USA (3) Leiden Observatory, Leiden University, P.O. Box 9513, 2300 RA Leiden, The Netherlands (4) School of Chemical and Physical Sciences, Flinders University, GPO Box 2100, Adelaide, SA 5001, Australia (5) Institute of Mathematical Sciences, University of Malaya, 50603 Kuala Lumpur, Malaysia (6) Space and Atmospheric Physics Group, Department of Physics, Imperial College London (7) Univ. Grenoble Alpes, CNRS, IPAG, F-38000 Grenoble, France
(panayotis.lavvas@univ-reims.fr / Fax: +33-3-26-91-31-47)

Abstract

We present a detailed model for the vibrational population of all non pre-dissociating excited electronic states of N_2, as well as for the ground and ionic states, in Titan's atmosphere. Our model includes the detailed energy deposition calculations presented in the past [1] as well as the more recent developments in the high resolution N_2 photo-absorption cross sections that allow us to calculate photo-excitation rates for different vibrational levels of singlet nitrogen states, and provide information for their pre-dissociation yields. In addition, we consider the effect of collisions and chemical reactions in the population of the different states. Our results demonstrate that a significant population of vibrationally excited ground state N_2 survives in Titan's upper atmosphere. This hot N_2 population can improve the agreement between models and observations for the emission of the c'_4 state that is significantly affected by resonant scattering. Moreover we discuss the potential implications of the vibrationally excited population on the ionospheric densities.

1. Introduction

Airglow (induced by solar photons) and aurora (by magnetospheric particles) are fundamental molecular processes that allow us to characterize the high altitude regions of planetary atmospheres. For the N_2-rich atmosphere of Titan (as well as those of the Earth, Triton, and Pluto) the emission spectrum of excited nitrogen demonstrates multiple bands from the plethora of excited electronic states available and covers a large part of the electromagnetic spectrum. Airglow is just one of the processes that take place at the high altitude regions of planetary atmospheres, though, the other being the collisional de-excitation of the different N_2 states that eventually defines the atmospheric local heating rate. Therefore, a detailed description of the N_2-state population is necessary for understanding these two processes. In this study we present a new N_2-state model focusing on Titan's atmosphere.

We specifically focus here on the resulting vibrational distribution of the ground state that has not been addressed in the previous studies. The presence of vibrationally excited N_2 can have important consequences for the atmospheric chemistry; excited molecules can partake in processes that are energetically forbidden for the more abundant ground state molecules, in this way allowing for chemical reactions that normally are not considered possible under Titan's atmospheric conditions. Such mechanisms have been identified in the Earth's atmosphere where the N_2 vibrational population has an important influence on the ionospheric electron density [2].

2. Model Description

In this study we developed a new model for the N_2 states' population, specifically for Titan. The advantage of our model is that it calculates the population of all non pre-dissociating states of N_2 and utilizes the detailed energy deposition calculations for Titan's atmosphere we have performed in the past [1]. The latter include the high-resolution, state-specific cross sections of N_2 derived from theoretical calculations, which only became available in recent years [3], and have important ramifications for the energy deposition in the atmosphere and the excitation of different electronic states. In addition, our model includes a detailed description of the collisional processes that could affect the different states, including chemical reactions, suitable for Titan's atmosphere.

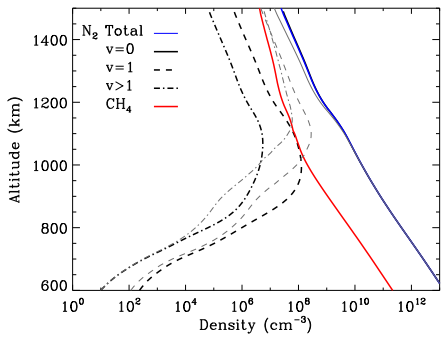

Figure 1: Density profiles for the ν=0, 1, and ν >1 vibrational levels for the nominal case compared with the total N_2 (blue) and CH_4 (red) density profiles. The thin gray lines represent the same results, but in the case that diffusion is not included in the calculations.

3. Results and Conclusions

Our results demonstrate that a significant population of vibrationally excited ground state molecules survives in Titan's upper atmosphere (Fig. 1). For the first excited vibrational level the density is comparable to that of methane, although the exact densities depend on the vibrational energy exchange rate with CH_4, which is not well constrained. We find that this vibrationally excited population of N_2 affects the resonant scattering for its excited singlet states and accounting for it leads to better agreement with the observed emissions from Cassini/UVIS. Particularly we find that the excited ground state levels result in a decrease of the CY(0,1) by a factor of 2, that is close to the required decrease (factor of 3) derived by [4] under the assumption of a thermal vibrational distribution (Fig. 2). In addition, we find that the non-thermal population brings the altitudes of peak emission for the CY(0,1) and CY(0,2) bands closer, in agreement with the observed peaks. Implications of the hot N_2 population on the other aspects of the ionosphere will be discussed.

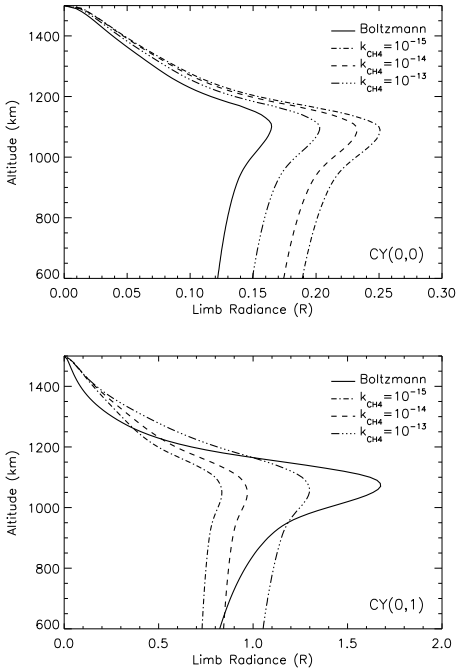

Figure 2: Limb radiances for the CY(0,0) and CY(0,1) transitions. Each panel presents the calculated emissions in spherical geometry, assuming different N_2 state vibrational distributions: solid lines correspond to a Boltzmann distribution at 150 K, while the broken lines correspond to the ground state vibrational distributions calculated with our model for the three different values of the vibrational energy transfer rate assumed between N_2 and CH_4. Their differences demonstrate the importance of the ground state population on the observable emissions.

References

[1] Lavvas, P., et al. (2011). Energy deposition and primary chemical products in Titan's upper atmosphere. Icarus, 213, 233-251.

[2] Campbell, L., et al. (2006). Role of electronic excited N_2 in vibrational excitation of the N_2 ground state at high latitudes. Journal of Geophysical Research, 111, A09317.

[3] Heays, A. N., et al. (2014). The high-resolution extreme ultraviolet spectrum of N_2 by electron impact. The Astrophysical Journal Supplement Series, 211, 28.

[4] Stevens, M. H., et al. (2011). The production of Titan's ultraviolet nitrogen airglow. Journal of Geophysical Research, 116(A),05304.

EPSC Abstracts
Vol. 10, EPSC2015-136, 2015
European Planetary Science Congress 2015

Water accumulation below Europa's strike-slip faults

K. Kalousová (1), G. Tobie (2), O. Souček (3), G. Choblet (2), and O. Čadek (1)
(1) Department of Geophysics, Charles University in Prague, Czech Republic (kalous@karel.troja.mff.cuni.cz)
(2) Laboratoire de Planétologie et Géodynamique, Université de Nantes, CNRS, France
(3) Mathematical Institute, Charles University in Prague, Czech Republic

Abstract

The onset of melting below Europa's recently active strike-slip faults and the gravitational/thermal stability of partially molten ice are investigated by solving the equations for a two-phase compressible mixture of water ice and liquid water in 2D geometry. As a first step, the relative motion between ice and water is neglected, i.e. the meltwater is transported by the flowing ice. Our preliminary results suggest that for sufficiently large shear heating rate of $\sim 2\times10^{-4}$ W m^{-3} melting can occur at depths as shallow as $\sim$3 km below Europa's surface. Moreover, the reservoirs of partially molten ice with $\sim$5–10% of liquid water can remain within the cold lid for a few hundreds of kiloyears if the underlying ice is sufficiently cold (viscous) and free of fractures.

1. Introduction

Tidal forces due to its eccentric orbit around Jupiter play a significant role in the thermal-orbital evolution of Europa. The associated deflection results in strong heating due to viscous friction which is mostly located in the warm convective part of the ice shell [1] and also along tidally-activated strike-slip faults in the upper part of the ice shell [2]. This heating might locally be strong enough to produce liquid water. The presence of large water lenses at shallow depths may possibly explain the formation of chaos terrains [3], observed in different locations on Europa's surface, as well as the ubiquitous double ridges [4].

The localization of water production and the efficiency of its extraction depend strongly on the thermal structure of the ice shell. In our previous study, we have examined ice melting and subsequent meltwater transport by two-phase flow in a simplified 1D geometry [5]. We found that partially molten reservoirs are not stable at the top of hot plumes. On the other hand, our 1D results suggested that liquid water might accumulate in cold conductive regions subjected to strong shear heating. Here, we concentrate on the latter case (melting at strike-slip faults) and investigate the stability of partially-molten regions in 2D Cartesian geometry.

2. Numerical model

The equations for two-phase flow of a compressible mixture of water ice and liquid water [6] are employed. These allow us to consistently address melting of ice and the subsequent meltwater transport by a combination of porous flow of water through the partially-molten ice matrix and convective Rayleigh-Taylor instabilities. In this work, as a first step, we neglect the relative motion between the ice matrix and the meltwater and consider the impermeable limit of the governing equations (by setting ice permeability equal to zero), thus concentrating on the transport of meltwater that is locked within the ice matrix - for this reason (i.e. assuming no porous flow), the residence times for liquid water should be considered as upper limits. A similar model has already been used in [1], but our approach allows the ice matrix to compact viscously when melting starts.

While water density and viscosity are kept constant and ice density is assumed to depend on temperature only (Boussinesq approximation), the ice viscosity is prescribed as a function of temperature, stress, (constant) grain size, and fraction of water [1,7]. Heating at the strike-slip fault is prescribed as a smooth function of coordinates with a maximum of 2×10^{-4} W m^{-3} [2] located in the middle of a domain 3 km below the surface, and is decreased with increasing amount of water. In some simulations, viscosity-dependent volumetric tidal heating [1] is considered.

3. Results and summary

In our reference simulation with grain size d=0.7 mm and considering only shear heating on the fault (i.e. assuming no volumetric tidal heating), melting starts at a depth of about 3 km below Europa's surface. The porosity (water volume fraction in the ice-water mixture) at the end of the simulation ($\sim$1900 kyr after the onset of melting) is depicted in the top panel of Figure 1. Even though the partially molten reservoir of few ($<$10) percents slowly propagates downwards due to the negative buoyancy of liquid water, the majority of produced meltwater is located in the top 10 km.

For a very small grain size, d=0.1 mm, which can be considered as a lower limit for Europa [8], melting starts at about the same place as in the reference case, however, due to small viscosity below the fault (of the order of 10^{13} Pa s), the partially molten region is not gravitationally stable and collapses downwards after less than 500 kyr from the onset of melting (middle panel of Fig. 1).

Finally, the viscosity-dependent tidal heating with the maximum amplitude of 5×10^{-6} W m^{-3}, which is the mean value for Europa [1], is introduced into the simulation with grain size d=0.7 mm. Melting starts again a few kilometers below the surface and, only a few tens of kiloyears later, the melt appears also at the bottom boundary (and accumulates there since water can only be advected by ice and the bottom boundary is prescribed to be impermeable for ice flow). Due to the faster temperature increase and the associated viscosity decrease below the fault, the partially molten material is less stable than in the simulation without volumetric heating and starts to collapse downwards - approximately 1700 kyr after the onset of melting, the majority of meltwater generated at the fault has already collapsed and is located at depths larger than 10 km (bottom panel of Fig. 1).

Overall, our results suggest that liquid water may be produced only a few kilometers below Europa's surface due to viscous friction at active strike-slip faults. The partially molten reservoirs with ∼5–10% of liquid water might remain within shallow depths for several hundreds of kiloyears, provided that the underlying ice is sufficiently viscous (with grain sizes of at least ∼0.7 mm) and cold (with small, i.e. $<5\times10^{-6}$ W m^{-3}, tidal heating amplitudes). The presence of melting-temperature lowering salts [9], especially in the cold upper part of the ice shell, might lead to earlier onset of melting and longer term stability of these reservoirs. The inclusion of plasticity and a more realistic parametrization of shear heating at the fault may also influence the lifetimes of water lenses. Progress in modeling these different effects and the consequences for melt stability will be presented at the meeting.

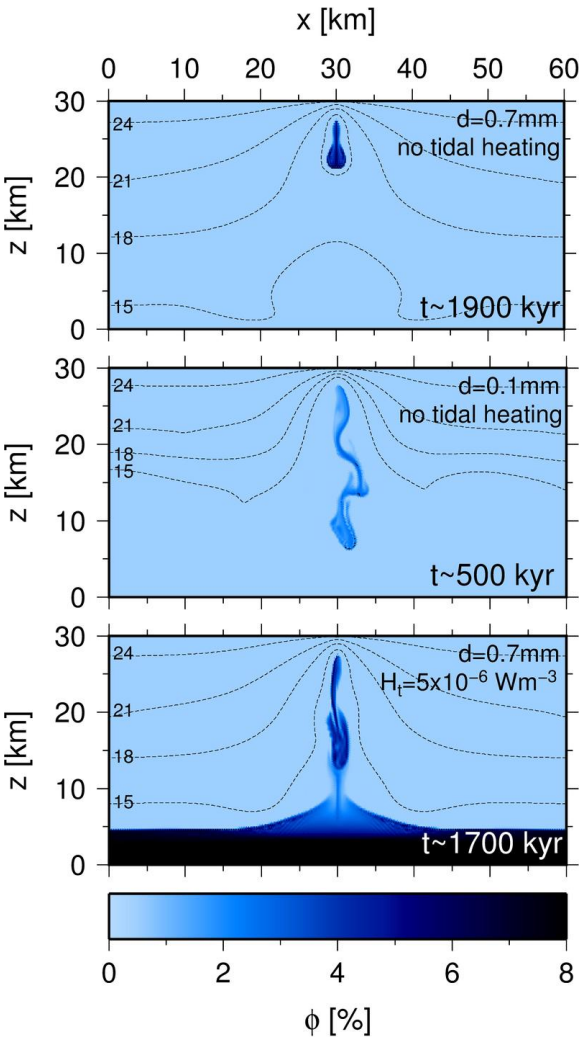

Figure 1: *Top*: Porosity at the end of the simulation with d=0.7 mm and no tidal heating. Time is counted from the onset of melting. Contours depict the logarithm of ice viscosity in Pa s. *Middle*: The same as above but for d=0.1 mm. *Bottom*: The same as above but for d=0.7 mm and H_t=5×10^{-6} W m^{-3}.

Acknowledgements

This research received funding from the European Research Council under the European Community's Seventh Framework Programme FP7/2007-2013 grant agreement 259285 and Grant Agency of Czech Republic through project 15-14263Y. This work was also supported by the IT4Innovations Centre of Excellence project (CZ.1.05/1.1.00/02.0070), funded by the European Regional Development Fund and the national budget of the Czech Republic via the Research and Development for Innovations Operational Programme, as well as Czech Ministry of Education, Youth and Sports via the project Large Research, Development and Innovations Infrastructures (LM2011033).

References

[1] Tobie et al. (2003), *JGR*, **108**, 5124–5138. [2] Nimmo & Gaidos (2002), *JGR*, **107**, 5021–5028. [3] Schmidt et al. (2011), *Nature*, **479**, 502–505. [4] Dombard et al. (2013), *Icarus*, **223**, 74–81. [5] Kalousová et al. (2014), *JGR*, **119**, 532–549. [6] Souček et al. (2014), *GAFD*, **108**, 639-666. [7] Goldsby & Kohlstedt (2001), *JGR*, **106**, 11017–11030. [8] Barr & Showman (2009), *Europa*, pp. 405–430. [9] Zolotov & Kargel (2009), *Europa*, pp. 431–457.

EPSC Abstracts
Vol. 10, EPSC2015-139, 2015
European Planetary Science Congress 2015

Estimates of Temperatures in Saturn's Upper Atmosphere from Cassini Radio Occultation Observations

L. Moore

Boston University, Center for Space Physics, Massachusetts, USA (moore@bu.edu)

Abstract

The effective or slab thickness (τ) of an ionosphere is defined as the ratio between local total electron content (TEC) and peak electron density (N_{MAX}). In a photochemical ionosphere this parameter is approximately four times the scale height (H=kT/mg) of the ionized neutral gas.

We use the 59 radio occultations of Saturn's ionosphere obtained by Cassini's RSS instrument in order to estimate thermospheric temperatures, and we compare these estimates with temperatures derived from solar and stellar occultations.

The globally averaged slab thickness in Saturn's ionosphere is roughly 1500 km. Given certain assumptions, such slab thicknesses translate into average temperatures of 400-600 K, with a slight increase at higher latitudes. In addition, slab thickness values below 1000 km are found only at low latitudes, within 20^o of Saturn's equator, perhaps indicative of relatively cooler equatorial temperatures.

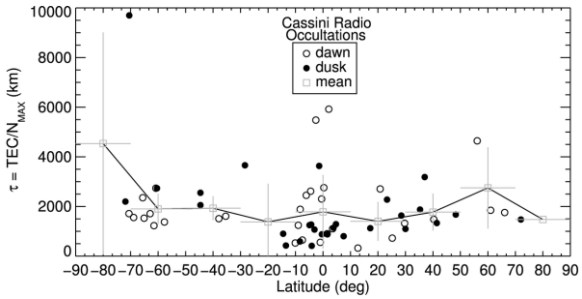

Figure 1: Slab thickness values from Cassini radio occultations.

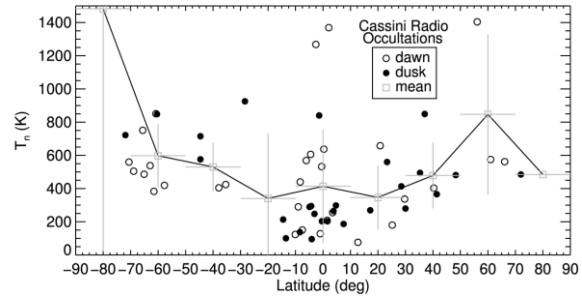

Figure 2: Thermospheric temperatures estimated from the slab thicknesses of Figure 1.

EPSC Abstracts
Vol. 10, EPSC2015-144, 2015
European Planetary Science Congress 2015

Global maps of Jupiter's ionosphere/thermosphere via H_3^+: ground-based observations from 2012 and 2015

J. O'Donoghue (1), L. Moore (1), H. Melin (2), T. Stallard (2)
(1) Center for Space Physics, Boston University, USA, (2) Radio & Space Plasma Physics, University of Leicester, UK
Correspondence to: jameso@bu.edu

Abstract

We present observations from two observing campaigns using the 3-metre NASA infrared telescope facility (IRTF) telescope and SpeX instrument; three full nights of observations were performed in Dec. 2012, and 4 nights in Feb. 2015. Both observations obtained near complete 360 degrees system III longitude and ±90 degrees planetocentric latitude maps of ionospheric H_3^+ molecular ion emissions. This ion is considered in local thermodynamic equilibrium with its surroundings and as such the properties derived from it - e.g. temperature - are inferred to represent that of the ionosphere and co-located thermosphere. Therefore, these maps display global energy distribution over the ionosphere in the different years. This work is highly complementary to data set to be taken by the Juno spacecraft, which arrives in the Jovian system in 2016.

Preliminary results within the 2012 data indicate (amongst many other things) a global pattern in mid-low latitude ionospheric emissions whereby one half of planetary longitudes are more emissive than the other (see Figure 1). The cause for this may be tied to asymmetries in planetary magnetic field, as a larger magnetic field strength could inhibit particle precipitation and therefore emissions.

The observations from 2015 were taken at a time of exceptional output from the volcanic moon Io and we examine the impact this may have had on the aurora and Io footprint at the time. Further results include cross-comparisons of data taken in 1997, 2012 and 2015 to explore long term behaviours.

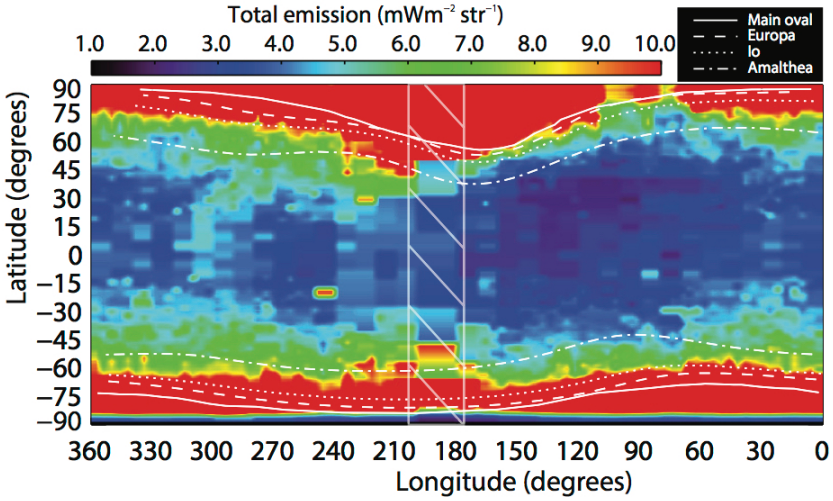

Figure 1: Global map of Jovian H_3^+ total emissions in Jupiter system III planetocentric coordinates.
The map has been limited to 10 $mWm^{-2}sr^{-1}$. All values are below 10% uncertainty. The grey diagonal lines in the centre indicate the interpolation of data. The over-plotted white lines show the magnetic footprints of satellites and the main oval, as indicated.

EPSC Abstracts
Vol. 10, EPSC2015-150, 2015
European Planetary Science Congress 2015

Mass loss as a driving mechanism of global tectonics of Enceladus

Leszek Czechowski
University of Warsaw, Faculty of Physics, Institute of Geophysics, ul. Pasteura 7,02-093 Poland (lczech@op.pl/Fax: +48-22-5546882)

Abstract

Enceladus, a satellite of Saturn, is the smallest celestial body in the Solar System where volcanic activity is observed. It is concentrated in the South Polar Terrain (SPT) where the mass is ejected into space with the rate ~200 kg/s. We suggest here the following tectonic consequences of this mass loss: subsidence of SPT, flow of matter in the mantle and motion of adjacent plates towards SPT. Some of these processes are modeled using numerical and laboratory simulations.

1. Introduction

Enceladus, a satellite of Saturn, is loosing mass as a result of its volcanic activity. Every second, the mass of ~200 kg is ejected into space from the South Polar Terrain (SPT) – Fig. 1. - [1, 2, 3, 4, 5, 6]. The mass forms E ring.

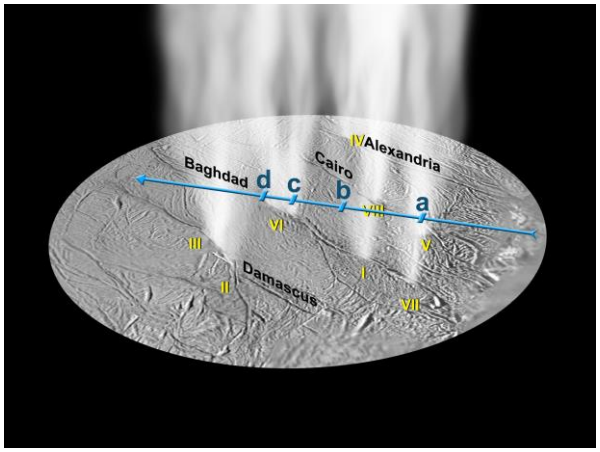

Figure 1: The jets from 'tiger stripes' in the South Polar Terrain on Enceladus (after NASA PIA10355).

The loss of matter from the body's interior should lead to global compression of the crust. Typical effects of compression are: thrust faults, folding and subduction. However, such forms are not dominant on Enceladus. We propose here special tectonic model that could explain this paradox.

2. Subsidence of SPT and tectonics

The volatiles escape from the hot region through the fractures forming plumes in the space – Fig.1. The loss of the volatiles results in a void, an instability, and motion of solid matter into the hot region to fill the void. The motion includes – Fig. 2:

(i) Subsidence of the 'lithosphere' of SPT.
(ii) Flow of the matter in the mantle.
(iii) Motion of plates adjacent to SPT towards the active region.

If emerging void is being filled by the subsidence of SPT only, then the velocity of subsidence is ~0.05 $mm \cdot yr^{-1}$. However, all three types of motion are probably important, so the subsidence is slower but mantle flow and plates' motion also play a role in filling the void.

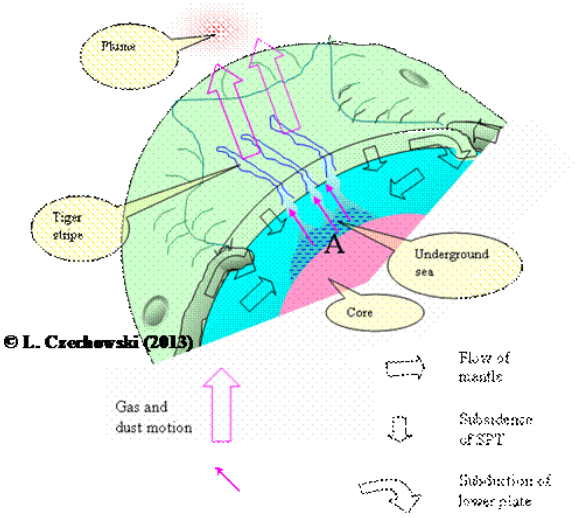

Figure 2: A scheme of suggested processes in the activity center (after [7]).

Note that in our model the reduction of the crust area is not a result of compression but it is a result of the plate sinking. Therefore the compressional surface features do not have to be dominant.

3. Models of subsidence

The numerical model of suggested process of subsidence is developed. It is based on the typical set of equation: Navier-Stokes equation for incompressible viscous liquid, equation of continuity

and equation of heat conduction. The Newtonian and non-Newtonian rheologies are used. The preliminary results of the model indicate that the subsidence rate of ~0.06 mm·yr^{-1} is possible if we assume Newtonian rheology of the ice. For non-Newtonian rheology more probable value is ~0.02 mm·yr^{-1}. In this case the velocity of motion of the 'mantle' material is higher.

4. Experimental model

Fig. 3 presents the map of the STP (left hand part of the figure). One can see the low polygonal region surrounded by the characteristic 'arcs'. In the laboratory model we observe the regular pentagonal plate (model of STP) sinking in viscoelastic material. Its rheology corresponds to assumption that icy plates are warm enough to creep like glaciers. The right hand side of the Fig. 3 presents the situation 150 hours after beginning of sinking. The most of the plate is already covered by the material – the size of the plate is given by the yellow double arrow. Note 'kinks', that are formed above vertices of the plate. Contrary to expectations (the viscoelastic material behaves like the fluid for the considered time scale) these 'kinks' appear to be stable features. This fact suggests that 'plates' adjacent to the SPT could behave like a glaciers.

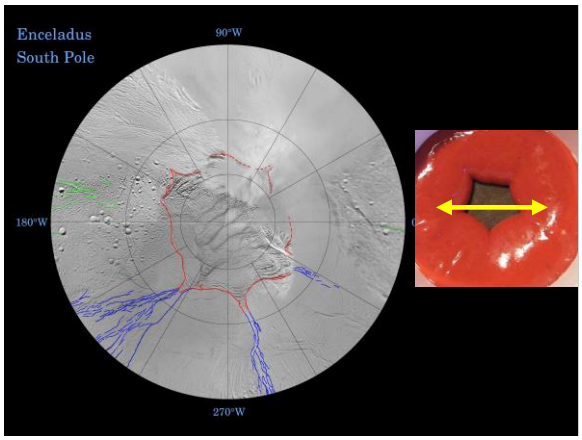

]Figure 3. The image of STP (left hand side, after NASA). Model of subsidence is on the right part of the figure. (after [7]).

5. Summary and Conclusions

Our hypothesis is a natural consequence of observed mass loss. In our opinion this mass loss is a main factor driving tectonic motions. Of course, it does not exclude some form of solid state convection in the icy mantle, but in fact this convection is not needed. The time of operation of this form of tectonics is not known. There are some observations suggesting that the activity in the STP is now decreasing. The periodic changes of activity are possible. Other observations suggest that in the past there were other centers of activity similar to the present STP [1, 6]. The indication of the future activity centers is less certain. However, the ovoid-shaped depression up to 2 km deep, of size 200×140 km with the center at 200E, 15S is a good candidate [6, 7].

Acknowledgements

The research is partly supported by National Science Centre (grant 2011/ 01/ B/ ST10/06653).

References

[1] Spencer, J. R., *et al*. Enceladus: An Active Cryovolcanic Satellite, in: M.K. Dougherty et al. (eds.), *Saturn from Cassini-Huygens*, Springer Science, (2009), p. 683.

[2] Kargel, J.S. Enceladus: Cosmic gymnast, volatile miniworld. *Science* 311, 1389–1391 (2006).

[3] Langenberg, H., Planetary science: Jets of mystery *Nature Geoscience* 1, 816 (2008) doi:10.1038/ngeo373.

[4] Giese, B., and the Cassini Imaging Team. The topography of Enceladus. *EPSC Abstracts* Vol. 5, EPSC2010-675 (2010).

[5] Kargel, J.S. Enceladus: Cosmic gymnast, volatile miniworld. *Science* 311, 1389–1391 (2006).

[6] Czechowski, L. Some remarks on the early evolution of Enceladus. Planet. Space Sci.11 (2014); 104. DOI: 10.1016/j.pss.2014.09.010

[7] Czechowski, L., Enceladus - the vanishing satellite - submitted

presenting in EGU 2014, Vienna.

EPSC Abstracts
Vol. 10, EPSC2015-156, 2015
European Planetary Science Congress 2015

Science Objectives for the Europa Clipper Mission Concept: Investigating the Potential Habitability of Europa

R. Pappalardo (1), D. Senske (1), L. Prockter (2), B. Paczkowski (1), S. Vance (1), A. Rhoden (2), B. Goldstein (1), T. Magner (2), and B. Cooke (1)
(1) Jet Propulsion Laboratory, California Institute of Technology, Pasadena, CA 91109, (2) Johns Hopkins University Applied Physics Laboratory, Laurel, MD 20723.

Abstract

Advancing our understanding of the icy worlds of the outer solar system will provide a basis to better evaluate potential habitability across the solar system. The exploration of Europa is at the forefront of gaining insight into the key components, water, chemistry, and energy, which make a world potentially habitable. The Europa Clipper mission concept would provide a systematic study of Europa, extending from its exosphere to the deep interior, providing significant knowledge as to how this icy water world formed and evolved.

1. Introduction

Understanding the processes that lead to potential habitability across the solar system is a key recommendation of the Planetary Science Decadal Survey, "*Visions and Voyages*" [1]. Fundamental to implementing this recommendation is evaluating the astrobiological significance of the icy satellites of the giant outer planets. It is in this context that Europa is at the forefront for recommended outer planet satellite exploration [1].

2. Europa's Potential Habitability

Advancing the state of knowledge of Europa's potential habitability has its basis in understanding the three "ingredients" for life: water, chemistry, and energy. It is hypothesized the Europa may have all three of these ingredients in the form of: (1) an extensive saltwater ocean beneath an ice shell that is geodynamically active and relatively thin (several kilometers to several tens of kilometers thick); (2) key chemical elements derived from the primordial chondritic composition of the Jovian protoplanetary disk, plus delivery by asteroids and comets over time; and (3) a source of chemical energy for life, from the combination of irradiation of its surface to produce oxidants, plus hydrothermal activity and/or serpentinization at its ocean floor to produce reductants. Key to this, the processes that shape Europa's ice shell, and the exchange processes between the surface and ocean, are not well understood. Even the existence of a subsurface ocean—while the evidence for its presence is compelling—is not proven.

3. Science Objectives for Europa Exploration

A NASA chartered Europa Science Definition Team (SDT) formulated the goal for future Europa exploration as: "Explore Europa to investigate its habitability." That group formulated objectives for a mission in Jupiter orbit that would make multiple-flybys of Europa:
(1) *Ocean and Ice Shell*: Characterize the ice shell and any subsurface water, including their heterogeneity, ocean properties, and the nature of surface-ice-ocean exchange;
(2) *Composition*: Understand the habitability of Europa's ocean through composition and chemistry;
(3) *Geology*: Understand the formation of surface features, including sites of recent or current activity, and characterize high science interest localities.

The Europa SDT also considered implications of the Hubble Space Telescope detection of a possible plume at Europa [2]. They concluded that the mission concept as conceived, if well instrumented, could do an excellent job of searching for and characterizing plumes, if they exist.

Science achieved by the Europa Clipper mission concept would provide global and regional characterization of this satellite. It is anticipated that a future step in addressing key scientific questions regarding the habitability and composition of Europa would be to land a spacecraft capable of *in situ* sampling and analysis. Based on a recent study of a Europa lander concept [3], additional information is needed regarding Europa's surface characteristics and properties to robustly architect a low-risk lander concept. To maximize technical and scientific success of a potential future landed mission, high fidelity surface reconnaissance is essential.

The SDT formulated a separate goal for reconnaissance of Europa as: *Characterize scientifically compelling sites, and hazards, for a potential future landed mission to Europa*. From this goal flow the two objectives of reconnaissance for the Europa Clipper mission concept:
(1) *Site Characterization*: Assess the distribution of surface hazards, the load-bearing capacity of the surface, the structure of the subsurface, and the regolith thickness, for at least 15 sites of interest;
(2) *Science Value*: Assess the composition of surface materials, the geologic context of the surface, the potential for geologic activity, the proximity of near-surface water, and the potential for active upwelling of ocean material, for at least 15 sites of interest.

4. The Europa Clipper Mission Concept

Based on the science and reconnaissance objectives, a joint technical team from the California Institute of Technology's Jet Propulsion Laboratory and the Johns Hopkins University Applied Physics Laboratory has devised a flight system and mission design that can accommodate a capable science payload responsive to the defined science objectives. A mission design has been developed that incorporates 45 close flybys of Europa, to achieve globally distributed regional surface coverage. The overall mission architecture is optimized to achieve science while minimizing radiation exposure inherent in the Jupiter system. The baseline concept is for a solar-powered spacecraft, launched on NASA's Space launch System (SLS).

5. Conclusions

A Jupiter-orbiting spacecraft that makes many flybys of Europa would provide an excellent platform from which to conduct measurements to investigate Europa's ocean and ice shell, composition, and geology, and thus the potential ingredients for life. Development of the Europa Clipper mission concept is ongoing, focusing on requirements development and spacecraft design trades.

It is anticipated that NASA will complete its initial phase of instrument selection in the spring of 2015. We will provide an update on status of the science and reconnaissance development of this mission concept.

References

[1] Space Studies Board: Vision and Voyages, The National Academies Press, Washington, DC, 2011.

[2] Roth, L. *et al.*: Transient Water Vapor at Europa's South Pole, *Science*, 343, 171-174, 2014.

[3] Europa Study Team: Europa Study Final Report—Lander: JPL Internal Document D-71990, 2012.

EPSC Abstracts
Vol. 10, EPSC2015-171, 2015
European Planetary Science Congress 2015

Search for evidence of Allene on Titan with new spectroscopic data

A. Jolly (1), Y. Benilan (1), L. Manceron (2), F. Kwabia-Tchana (1), C. Nixon (3)

(1) Laboratoire Interuniversitaire des Systèmes Atmosphériques (LISA), UMR 7583 du CNRS, Universités Paris Diderot et Paris-Est Créteil, Institut Pierre Simon Laplace (IPSL), Créteil, France.
(2) Synchrotron SOLEIL, L'orme des Merisiers, Saint-Aubin-BP 48, 91192 Gif-sur-Yvette Cedex and MONARIS, UMR 8233. CNRS-UPMC, 4, place Jussieu 75252, France.
(3) Planetary Systems Laboratory, NASA Goddard Space Flight Center, Greenbelt MD 21113, USA.

1. Introduction

The Composite Infrared Spectrometer (CIRS) on-board Cassini has recorded spectra in the far and mid-infrared since 2004 with a spectral resolution of up to 0.5 cm^{-1}. Mismatch between observed and model spectra obtained from the available line lists has led us to study the spectroscopic parameters of HC_3N, C_4H_2 and C_2N_2, the longest gas phase carbon chains observed so far on Titan. Fundamental and hot band intensities, as well as line lists were systematically verified by comparison with new laboratory spectra. Erroneous band intensities, as well as an absence or shortage of hot band transitions in the available line lists leading to model-data mismatches and inaccurate quantifications have been found.
Improvement in the spectroscopic parameters has led to the detection of ^{13}C isotopologues of HC_3N [1] and C_4H_2 [2]. The study on C_2N_2 opens the way to the detection of ^{15}N isotopologues whose abundances could give clues to understand the origin and the evolution of Titan's atmosphere [3]. The higher accuracy of spectroscopic data used to model CIRS spectra enables the search for longer carbon chains on Titan such as HC_5N, C_6H_2 and C_4N_2. Intensity measurements and a careful analysis of high resolution data has led to the first line lists for C_4N_2. No detection of this molecule has yet been possible, but a precise abundance upper limit of C_4N_2 in the gas phase in Titan's atmosphere could be determined [4].
One of the molecules that were often searched for in Titan's atmosphere is allene **(CH_2CCH_2)**.

2. Allene

Allene has not been observed so far in Titan's atmosphere although it has three active bending modes, ν_9 (999 cm^{-1}), ν_{10} (845 cm^{-1}) and ν_{11} (352cm^{-1}) in the CIRS observation range. Allene is also an isomer of propyne **(CH_3CCH)** which has been observed on Titan, thanks to two bending modes ν_9 (633 cm^{-1}) and ν_{10} (327 cm^{-1}) by the Voyager mission. These data have shown that the abundance of propyne in Titan's atmosphere has reached values as high as 10^{-6} at the north pole [5]. The clearly lower abundance of allene is not straightforward to understand since both isomers are very similar from a chemical point of view. The most obvious explanation is the existence of an isomerization process where allene transforms into propyne, but the efficiency of such a process is not easy to quantify. Another factor which could influence the abundances of allene and propyne would be differences in photolysis rates.

Anyway, the presence of allene on Titan cannot be ruled out yet. A tentative detection has in fact already been made from the ground with the TEXES instrument at high resolution. The identification concerns ν_{10} subbands close to 845 cm^{-1} among strong emission lines of ethane (C_2H_6). This tentative detection was presented at the EPSC-DPS joint meeting 2011 and, according to the authors, a definitive detection could not be made due to the lack of good line lists. No allene line list is present either in HITRAN or in GEISA, but Coustenis et al. [6] already investigated the detectability of allene in Titan's atmosphere using spectroscopic parameter by Chazelas et al. [7], for the ν_{10} band centered at 845 cm^{-1} and from Pliva and Kauppinen, for the ν_{11} band near 352 cm^{-1} [8]. Line intensities could be obtained from band intensity measurements by Koga et al.[9].

They concluded that the non-detection of allene implied an abundance below 5.10^{-9}.

In this work, we have used the same spectroscopic data but also added parameters obtained in high resolution studies by Nissen et al. [10] and Hegelund et al. [11], which also include spectroscopic parameters for the hot bands. The hot band contribution is particularly important at room temperature and needs to be included in order to compare the calculated line lists with room temperature spectra. Calculations have been tested against room and high temperature spectra taken at 0.08 cm-1 resolution in the ν_{10}/ν_9 wavenumber range. Concerning the far infrared region where the ν_{11} band of allene can be observed, we have recorded room temperature spectra with a resolution of 0.1 cm^{-1} at the SOLEIL-AILES synchrotron beamline with the same apparatus used for our previous studies [3, 4]. Figure 1 compares the laboratory spectra obtained in the far infrared with calculations using the new line list.

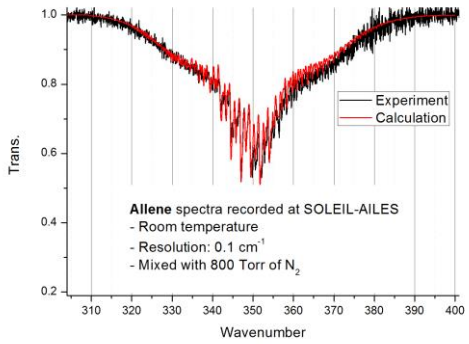

Figure 1: Allene ν_{11} laboratory spectra compared to calculated spectra.

As can be seen, our calculation reproduces the measured spectra quite satisfyingly. Very precise comparison between laboratory and calculated spectra in the ν_{10} /ν_9 region also give very good results.

This means that allene can be searched in CIRS spectra of Titan in both spectral regions with good confidence. The first attempts to detect allene in Titan's atmosphere with CIRS observations and the new line lists will be presented.

References

1. Jennings, D., et al., *Isotopic Ratios in Titan's Atmosphere from Cassini CIRS Limb Sounding: HC_3N in the North.* Astrophysical Journal, 2008. **681**: p. L109-L111.
2. Jolly, A., et al., *The n8 bending mode of diacetylene: from laboratory spectroscopy to the detection of C-13 isotopologues in Titan's atmosphere.* Astrophysical Journal, 2010. **714**(1): p. 852-859.
3. Fayt, A., et al., *Frequency and intensity analyses of the far infrared nu(5) band system of cyanogen (C2N2) and applications to Titan.* Journal of Quantitative Spectroscopy & Radiative Transfer, 2012. **113**(11): p. 1195-1219.
4. Jolly, A., et al., *Gas phase dicyanoacetylene (C4N2) on Titan: New experimental and theoretical spectroscopy results applied to Cassini CIRS data.* Icarus, 2015. **248**: p. 340-346.
5. Vinatier, S., et al., *Seasonal variations in Titan's middle atmosphere during the northern spring derived from Cassini/CIRS observations.* Icarus, 2015. **250**: p. 95-115.
6. Coustenis, A., et al., *Modelling Titan's thermal infrared spectrum for high-resolution space observations.* Icarus, 1993. **102**: p. 240.
7. Chazelas, J., et al., *Analysis of the V_9/V_{10} band system of allene.* Journal of Molecular Spectroscopy, 1985. **110**(2): p. 326-338.
8. Pliva, J. and J. Kauppinen, *High-resolution Fourier-transform study of the perpendicular band n_{11} of allene at 353 cm^{-1}.* Journal of Molecular Spectroscopy, 1985. **111**(1): p. 93-101.
9. Koga, Y., et al., *Infrared absorption intensities of allene.* J. Chem. Phys., 1979. **71**(6): p. 2404-2411.
10. Nissen, S., et al., *High-resolution infrared study of the nu(11) band of allene.* Journal of Molecular Spectroscopy, 2002. **216**(2): p. 197-202.
11. Hegelund, F., N. Andresen, and M. Koivusaari, *A high-resolution infrared study of the $N_9+N_{11}-N_{11}$, $N_{10}+N_{11}-N_{11}$ hot band sytem in allene.* Journal of Molecular Spectroscopy, 1993. **159**(1): p. 230-248.

EPSC Abstracts
Vol. 10, EPSC2015-175, 2015
European Planetary Science Congress 2015

Enceladus-Mimas paradox: a result of different early evolutions of satellites?

Leszek Czechowski , Piotr Witek
Institute of Geophysics University of Warsaw, ul. Pasteura 7, 02-093 Warszawa, Poland E-mail: lczecho@op.pl

Abstract

Thermal history of Mimas and Enceladus is investigated from the beginning of accretion to 400 Myr. The following heat sources are included: short lived and long lived radioactive isotopes, accretion, serpentinization, and phase changes. We find that temperature of Mimas' interior was significantly lower than of Enceladus. Comparison of thermal models of Mimas and Enceladus indicates that conditions favorable for starting tidal heating lasted for short time (~10^7 yr) in Mimas and for ~10^8 yr in Enceladus. This could explain Mimas-Enceladus paradox.

1. Numerical model

In our calculations we use numerical model developed by Czechowski (2012) (see e.g. description in [1]). The model is based on parameterized theory of convection combined with 1-dimensional equation of the heat transfer in spherical coordinates:

$$\rho c_p \frac{\partial T(r,t)}{\partial t} = \mathrm{div}(k(r,T)\,\mathrm{grad}T(r,t)) + \rho Q(r,t)$$

where r is the radial distance (spherical coordinate), ρ is the density [kg m^{-3}], c_p [J kg^{1} K^{-1}] is the specific heat, Q [W kg^{-1}] is the heating rate, and k [W m^{-1} K^{-1}] is the thermal conductivity. $Q(r, t)$ includes sources and sinks of the heat. The equation is solved in time dependent region [0, R(t)]. During accretion the radius $R(t)$ increases in time according to formula: $R(t) = a\,t$ for $t_{ini} < t < t_{ac}$, and $R(t) = R_{sat}$ for $t > t_{ac}$, i.e. after the accretion (see e.g. [2]), where t_{ini} denotes beginning of accretion and t_{ac} denotes duration of this process.

If the Rayleigh number in the considered layer exceeds its critical value Ra_{cr} then convection starts. It leads to effective heat transfer. The full description of convection is given by a velocity field and temperature distribution. However, we are interested in convection as a process of heat transport only. For solid state convection (SSC) heat transport can be described by dimensionless Nusselt number Nu. We use the following definition of the Nu:

Nu= (True total surface heat flow)/(Total heat flow without convection).

The heat transport by SSC is modelled simply by multiplying the coefficient of the heat conduction in the considered layer, i.e.:

$$k_{conv} = Nu\ k.$$

This approach is used successfully in parameterized theory of convection for SSC in the Earth and other planets (e.g. [3], [4]).

Parameterization of liquid state convection (LSC) is even simpler. Ra in molten region is very high (usually higher than 10^{16}). The LSC could be very intensive resulting in almost adiabatic temperature gradient given by:

$$\frac{dT}{dr} = \frac{g\alpha_m T}{c_{pm}},$$

where α_m and c_{pm} are thermal expansion coefficient and specific heat in molten region, g is the local gravity. In Enceladus and Mimas the

adiabatic gradient is low and therefore LSC region is almost isothermal.

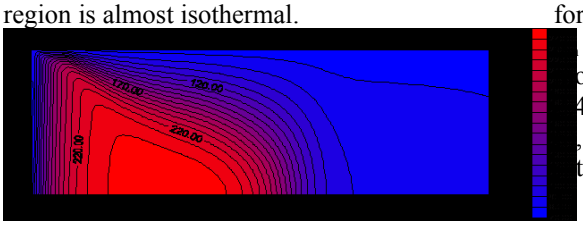

Fig.1 Thermal evolution of Mimas for the following values of parameters: ηm of 10^{14} Pa s, c_{hyd}= 240000 J kg^{-1}, E= 5×10^4 J mole^{-1}, $t$ac =0.1 Myr, k_{sil}=4.2 W m^{-1} K^{-1}, t_{ini} =1.8 Myr. Vertical axis gives distance from the center of the satellite (r/R_{Sat}). Horizontal axis gives log10(time in Myr) Note that initially the isotherms are going up following increasing radius of the accreting body. For the first Myr's the temperature increases fast because of high concentration of the radioactive elements. The maximum is reached in a few millions of years and subsequently isotherms corresponding to high temperature (say 220 K) move down.

2. Results

Comparison of thermal models of Mimas and Enceladus indicates that conditions favorable for starting tidal heating (interior hot enough) lasted for short time (~10^7 yr) in Mimas and for ~10^8 yr in Enceladus. This could explain Mimas-Enceladus paradox – see Fig. 1 and Fig. 2.

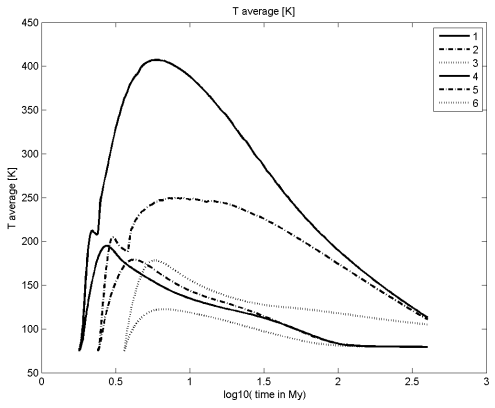

Fig.2 Comparison of average temperature T_{ave} for Enceladus and Mimas. Parameters: viscosity of 10^{14} Pa s, c_{hyd}= 240000 J kg^{-1}, E= 5×10^4 J ole^{-1}, t_{ac} =0.1 Myr, k_{sil}=4.2 W m^{-1} K^{-1}, t_{ini} =1.8, 4, 3.6 Myr for lines 1 (and 4), 2 (and 5), 3 (and , respectively. Initial temperatures of both tellites are the same; note common point at t = (leftmost). All lines for Mimas are below the corresponding lines for Enceladus indicating lower temperature in smaller Mimas. Note also that all lines for Mimas for large time converge for substantially

Conclusions

The Mimas-Enceladus paradox is probably the result of short time when Mimas was hot enough to allow for substantial tidal heating. The Mimas-Tethys resonance formed later when Mimas was already cool. (see also [1, 4]) The full text of the paper will be published in Acta Geophysica [5].

Acknowledgements: The research is partly supported by National Science Centre (grant 2011/ 01/ B/ ST10/06653).

References :

[1] Czechowski, L. (2014) Some remarks on the early evolution of Enceladus. Planet. Sp. Sc. 104, 185-199.

[2] Merk, R., Breuer, D., Spohn, T. (2002). Numerical modeling of ^{26}Al induced radioactive melting of asteroids concerning accretion. Icarus 199, 183-191.

[3] Sharpe, H.N., Peltier, W.R., (1978) Parameterized mantle convection and the Earth's thermal history. Geophys. Res. Lett. 5, 737-740.

[4] Czechowski, L. (2006) Parameterized model of convection driven by tidal and radiogenic heating. Adv. Space Res. 38, 788-793.

[5] Czechowski, L., Witek, P. (2015) Comparisons of early evolutions of Mimas and Enceladus. In press in Acta Geophysica.

EPSC Abstracts
Vol. 10, EPSC2015-181, 2015
European Planetary Science Congress 2015

Eclipse-induced changes of Titan's meteorology at equinox

T. Tokano
Institut für Geophysik und Meteorologie, Universität zu Köln, Germany (tokano@geo.uni-koeln.de)

Abstract

The impact of equinoctial eclipses on Titan's meteorology is investigated by a global climate model. Eclipses are simulated by globally turning off the solar heating at the right time. The surface temperature on the subsaturnian side suddenly drops during an eclipse by a small amount. This in turn affects the temperature and wind in the planetary boundary layer due to slightly reduced convective heating transfer from the surface. The impact of eclipses is not entirely negligible for Titan's meteorology.

1. Introduction

An eclipse of Titan by Saturn occurs when the Sun passes through Titan's orbital plane, so that Saturn can periodically put Titan into its own shadow. This repeatedly (~20 times) occurs within a period of ~1 year around the vernal and autumnal equinox for up to ~6 hours. Due to synchronous rotation of Titan only the subsaturnian side is directly affected by an eclipse. Titan's eclipses are excellent opportunities to observe Titan's airglow in darkness [1]. On the other hand, an eclipse is also known to cause small meteorological changes on Earth [2]. This study explicitly investigates whether similar meteorological effects may also be expected on Titan.

2. Methods

The impact of the eclipse on Titan's meteorology is investigated by comparing the results of simulations with a Titan global climate model (GCM) carried out with and without implementing eclipses. The most recent version of the Cologne Titan GCM [3] is used. The thermal inertia of the surface has been tuned such as to approximately fit the observed diurnal cycle of the surface temperature at low latitudes [4]. An eclipse is simulated by globally turning off the solar heating for the duration of an eclipse. The eclipse duration and timing are calculated as a function of the season, i.e. the Saturn-centric longitude of the Sun (L_S), and local time at Titan's subsaturnian meridian.

3. Results

During an eclipse the surface temperature on the subsaturnian side decreases for up to 6 hours by 0.1 K or so. The diurnal maximum temperature is thus systematically lower on the subsaturnian side than on the antisaturnian side on 20 consecutive Titan days. The impact of eclipses on the atmosphere is less clear-cut but not negligible. The mean atmospheric temperature near the surface is slightly lower if eclipses are taken into account. This is not caused by in situ radiative cooling of the air during the eclipse but due to slightly reduced convective heat transfer from the surface. The perturbation of the surface air temperature has an influence on the surface winds. This study investigates the significance of the response of the atmosphere (temperature, wind and pressure) to eclipses dependent on longitude, latitude and altitude.

Acknowledgements

The author is supported by DFG grant TO 269/4-1.

References

[1] Lavvas, P., et al.: Titan's emission processes during eclipse. Icarus, Vol. 241, pp. 397-408, 2014.

[2] Aplin, K. L., Harrison, R. G.: Meteorological effects of the eclipse on 11 August 1999 in cloudy and clear conditions. Proc. R. Soc. London A, Vol. 459, pp. 353-371, 2003.

[3] Tokano, T.: Wind-induced equatorial bulge in Venus and Titan general circulation models: Implication for the simulation of superrotation. Geophys. Res. Lett., Vol. 40, pp. 4538-4543, 2013.

[4] Cottini, V., et al.: Spatial and temporal variations in Titan's surface temperatures from Cassini CIRS observations. Planet. Space Sci., Vol. 60, pp. 62-71, 2012.

EPSC Abstracts
Vol. 10, EPSC2015-193, 2015
European Planetary Science Congress 2015

Planetcam UPV/EHU – A lucky imaging camera for multi-spectral observations of the Giant Planets in 0.38-1.7 μm

R. Hueso (1,2), I. Mendikoa (1), A. Sánchez-Lavega (1,2), S. Pérez-Hoyos (1,2), J. F. Rojas (1,2), E. García-Melendo (1,3)
(1) Dpto. Física Aplicada I, E.T.S. Ingeniería, Universidad del País Vasco, Bilbao, Spain, (2) Unidad Asociada Grupo Ciencias Planetarias UPV/EHU- IAA (CSIC) Bilbao, Spain, (3) Fundació Observatori Esteve Duran, Montseny 46, 08553 Seva, Barcelona. Spain. (ricardo.hueso@ehu.es / Fax: +34 94601 4178)

Abstract

PlanetCam UPV/EHU [1] is an astronomical instrument designed for high-resolution observations of Solar System planets. The main scientific themes are atmospheric dynamics and the vertical cloud structure of Jupiter and Saturn. The instrument uses a dichroic mirror to separate the light in two beams with spectral ranges from 380 nm to 1 micron (visible channel) and from 1 to 1.7 microns (Short Wave InfraRed, SWIR channel) and two detectors working simultaneously with fast acquisition modes. High-resolution images are built using lucky imaging techniques [2]. Several hundred short exposed images are obtained and stored in fits files. Images are automatically reduced by a pipeline called PLAYLIST (written in IDL and requiring no interaction by the user) which selects the best frames and co-registers them using image correlation over several tie-points. The result is a high signal to noise ratio image that can be processed to show the faint structures in the data. PlanetCam is a visiting instrument mainly built for the 1.23 and 2.2m telescopes at Calar Alto Observatory in Spain but it has also been tested in the 1.5 m Telescope Carlos Sanchez in Tenerife and the 1.05 m Telescope at the Pic du Midi observatory.

1. Spatial resolution and filters

Each detector allows three optical configurations with spatial resolutions that can suit different atmospheric seeing conditions or observational constraints. Spatial resolution ranges from 0.03'' to 0.23'' per pixel in the 2.2m telescope at Calar Alto Observatory in Spain. Low luminous sources can be observed in the visible by using binning factors that sacrifice spatial resolution. Atmospheric seeing strongly affects the results and details over an extended object like Jupiter smaller than 0.4'' are difficult to resolve in most observing runs. Smaller and bright objects like Ganymede allow attaining spatial resolutions of 0.2'' indicating difficulties in lucky imaging with large aperture telescopes. The strength of PlanetCam, however, is the capability of obtaining high-resolution observations also in narrow band filters.

Observations are obtained in broad band visible filters and in narrow band filters in and out methane absorbing bands in the visible and near infrared. These observations allow to study and characterize the vertical cloud structure of Giant and Icy Planets. Additional filters from the blue to UV part of the spectrum complement this information and are also useful for the study of Venus and Mars clouds.

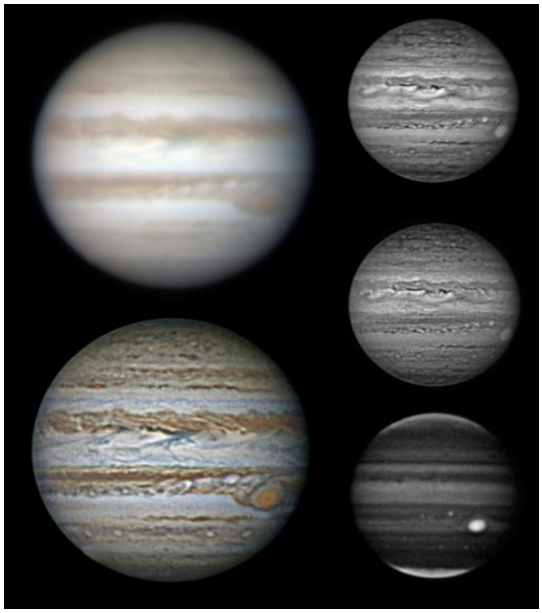

Figure 1. Jupiter. Left panel: Visible RVB color image with photometric quality (top) and after applying high-pass filters to show the high resolution data (bottom). Right panel: SWIR images in bands J, H and in a methane absorption band at 1160 nm. Observations from 11 December 2014.

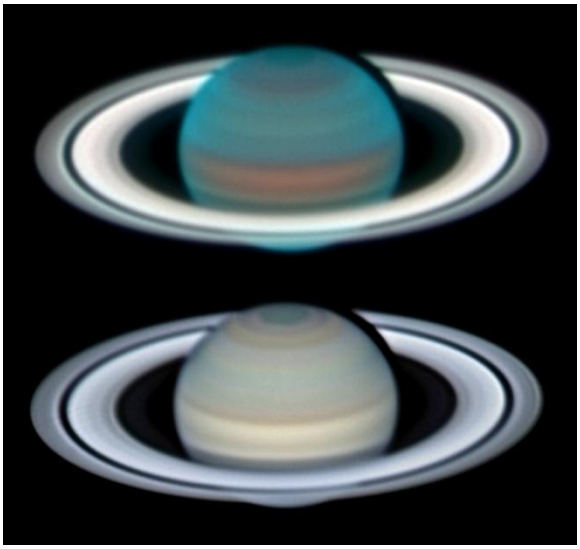

Figure 2: Saturn. Top: Upper hazes observed with a combination of a weak methane band filter, a violet and an ultraviolet filter. Bottom: Lower clouds observed in broadband RVB Johnson filters. Observations from 6 April 2014.

2. Science themes

Jupiter and Saturn observations have been obtained on the last planetary oppositions. We plan to keep observing both planets in the next few years with the next main objectives:

1- Support to Juno on Jupiter. While Jupiter will be the subject of an international broad collaboration with amateurs, PlanetCam can obtain both Visible and SWIR images of the planet.

2- Multi-spectral Ground-based observations of Saturn. Low phase angles observations complement Cassini observations of Saturn which are scarcer in the last years of the mission due to the characteristics of the orbital tour around the Saturn system. Additionally, latitudinal coverage is different from Cassini and ground-based observations.

3- Time critical phenomena. Jupiter and Saturn present dynamic atmospheres where unexpected events of large interest occasionally happen [3, 4]. Also in the event of an impact in any of these planets such as the 2009 large impact [5] or other smaller impacts [6] we can provide a quick response from Calar Alto.

In each observing night we use the rest of the hours for other scientific cases in Solar System (Venus clouds for dynamics studies, Mars, Uranus, Neptune and Titan). We also have observation runs of star occultations by asteroids and transneptunian objects as well as exoplanetary transits. In all these areas PlanetCam can provide valuable data.

Acknowledgements

This work was supported by the Spanish project AYA2012-36666 with FEDER support, Grupos Gobierno Vasco IT765-13 and UPV/EHU UFI11/55.

References

[1] A. Sánchez-Lavega et al. *Proc. of SPIE*, **8446**, 84467X-1 (2012).

[2] N. Law et al. Lucky Imaging: High Angular Resolution Imaging in the Visible from the Ground. *Astronomy & Astrophysics*, **446**, 739 – 745 (2005).

[3] Sánchez-Lavega et al. Depth of a strong Jovian jet from a planetary-scale disturbance driven by storms. *Nature*, **451**, 437-440 (2008).

[4] Sánchez-Lavega et al. Deep winds beneath Saturn's upper clouds from a seasonal long-lived planetary-scale storm. *Nature*, **475**, 71-74 (2011).

[5] Sánchez-Lavega et al. The impact of a large object with Jupiter in July 2009. *ApJ.* **715**, L150 (2010).

[6] Hueso et al. Impact flux on Jupiter: From superbolides to large-scale collisions. *A&A*, **560**, A55, (2013).

EPSC Abstracts
Vol. 10, EPSC2015-225, 2015
European Planetary Science Congress 2015

How did Enceladus form?

O. Mousis (1), S. Charnoz (2), A. Crida (3), P. Estrada (4) and J. H. Waite (5)
(1) Aix Marseille Université, CNRS, LAM (Laboratoire d'Astrophysique de Marseille) UMR 7326, 13388, Marseille, France (olivier.mousis@lam.fr), (2) Institut Universitaire de France, Institut de Physique du Globe, Paris, France, (3) Institut Universitaire de France, Laboratoire Lagrange, UMR 7293; Université Nice Sophia-antipolis / CNRS / Observatoire de la Côte d'Azur, France, (4) Carl Sagan Center, SETI Institute, 189 N. Bernardo Ave. # 100, Mountain View, CA 94043, USA, (5) Department of Space Science, Southwest Research Institute, 6220 Culebra Rd., San Antonio, TX 78228, USA.

Abstract

The Cassini Ion Neutral Mass Spectrometer detected a mass peak at mass 28 in Enceladus' plumes, which was originally interpreted as CO coming from the dissociation of CO_2 on the walls of the INMS closed ion source ante chamber. [1]. However, a more recent analysis suggests that this determination would more likely correspond to the presence of plume-originated CO and/or N_2 emanating from the plumes [2]. Assuming that CO and N_2 have been trapped in Enceladus' building blocks during their formation poses a consistency problem with the scenarios of Titan's formation, arguing that this satellite formed from planetesimals condensed in the protosolar nebula before having been partly devolatilized within Saturn's subnebula during migration and accretion [3]. In this scenario, CO and N_2 would have been strongly depleted in Titan's building blocks, in agreement with i) the extremely low atmospheric abundance of CO observed in the Titan atmosphere and ii) the fact that N_2, the main atmospheric constituent, could derive from the photolysis of primordial NH_3 [4] or from shock chemistry [5]. Following this scheme, the building blocks of Enceladus, whose orbit is interior to that of Titan, should have been too depleted in primordial CO and N_2.

In our presentation, we will investigate the different formation scenarios of Enceladus that could explain the present composition of its plumes. One strong constraint derived from the INMS data is that Enceladus' planetesimals must have either i) migrated on colder tracks in Saturn's subnebula than those of Titan did or ii) were larger when they formed so they did not have the time to significantly outgass during migration through the Saturn subnebula. All these possibilities will be discussed in our presentation.

References

[1] Waite, J. H., Jr., Lewis, W. S., Magee, B. A., et al. 2009, Nature, 460, 487

[2] Waite, J.~H., Brockwell, T., Magee, B., et al., 2013,AGU Fall Meeting Abstracts, 8

[3] Mousis, O., Lunine, J. I., Thomas, C., et al. 2009. ApJ, 691, 1780

[4] Atreya, S. K., Donahue, T. M., and Kuhn, W. R. 1978, Science, 201, 611.

[5] Sekine, Y., Genda, H., Sugita, S., Kadono, T., and Matsui, T. 2011, Nature Geoscience, 4, 359

EPSC Abstracts
Vol. 10, EPSC2015-231, 2015
European Planetary Science Congress 2015

An analysis of the stability of Saturn's Hexagon jet and its counterpart in the South

A. Antuñano (1), T. del Río-Gaztelurrutia (1,2), A. Sánchez-Lavega (1,2)
(1) Departamento de Física Aplicada I, E.T.S. Ingeniería, Universidad del País Vasco, Bilbao, Spain.
(2) Unidad Asociada Grupo Ciencias Planetarias UPV/EHU-IAA (CSIC), Bilbao, Spain.

Abstract

In this study we use the wind and vorticity gradient profiles from A. Antuñano et al. [1] to study the stability of Saturn's Hexagon jet and its counterpart in the south by analyzing the barotropic instability of quasi-geostrophic jets. We also present the growth rates of the barotropic instabilities for both jets.

1. Introduction

Images obtained by the Voyager I and II flybys in 1980-1981 showed a hexagonal feature at 75ºN planetocentric latitude with an embedded fast eastward jet reaching a peak velocity of 120 ms^{-1} [4]. This same feature was again re-observed by ground based telescopes and by the Hubble Space Telescope (HST) in 1990-1995 [5-6]. After the arrival of the Cassini Mission to Saturn in 2004, the hexagon was again observed, first in the infrared with VIMS [2] and then, with the ISS after the equinox in 2009. The hexagon has remained stationary in System III for the last 30 years [5-7]. During 1997 and 2002 the South of Saturn's was captured by the HST showing a strong eastward jet at similar latitudes [6]. However, these images did not show any hexagonal feature in the south.

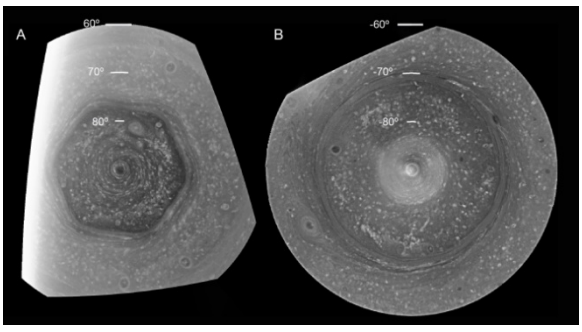

Figure 1 Cassini ISS CB2 images of Saturn's poles: A) North polar region on 14 June 2013. B) South polar region on December 2008. [1]

Antuñano et al. [1] compared the dynamics of both polar regions, showing that the wind and vorticity profiles of both jets (hexagon and its counterpart) are similar, except for the 5º difference in latitude of the jets, and that the Rayleigh-Kuo instability is satisfied in both jets.

As the violation of Rayleigh-Kuo stability criterion does not guarantee the growth of an instability, we analyze the linear barotropic stability of the Hexagon jet and its equivalent using the data from Antuñano et al. [1]. We also compute the growth rates of the barotropic instability for different Rossby deformation radius L_D and wave numbers m.

2. Analysis

The vorticity equation for a barotropic and inviscid flow is

$$\frac{D(q'+f)}{Dt}=0 \qquad (1)$$

Where $q'=\nabla^2\psi'-\frac{\pi^2}{L_D^2}\psi'$ is the shallow water quasi-geostrophic potential vorticity, ψ' is the eddy stream function, L_D is the Rossby deformation radius and f is the Coriolis parameter. We seek for a solution of the type

$$\psi'=\Psi'(y)e^{ik(x-ct)} \qquad (2)$$

where $k=m/r\cos(\varphi)$ is the wave number, r is Saturn's radius at that latitude, φ is the mean latitude [3] and c is the phase velocity and may be complex. Substituting this solution in (1) and after derivation we obtain the vorticity equation.

$$u(y)\left[\partial_{yy}-k^2-\frac{\pi^2}{L_D^2}\right]\Psi+\left[\beta-u_{yy}\right]\Psi=c\left[\partial_{yy}-k^2-\frac{\pi^2}{L_D^2}\right]\Psi \qquad (3)$$

We have solved this eigenvalue equation for different values of L_D and k, with the zonal velocity and vorticity gradient profiles from Antuñano et al. [1], using the finite difference method and $\partial\Psi'/\partial y=0$ at 5000km north and south from the peak as boundary

conditions. The aim of this study is to obtain the growth rates (kc_i) of a barotropic disturbance, thus, we seek for the eigenvalue (phase speed) with the largest imaginary part for each L_D and k, which corresponds to the most rapidly growing mode.

3. Results

Our barotropic instability analysis shows that the faster growing mode for a Rossby deformation radius of L_D=3000km, is m=5-6 for both the northern and southern hemisphere. One could be tempted to assume that the hexagon in the north, mode 6, is related to this instability maximum. However, no hexagonal feature is observed in the south and thus, this analysis does not shed light on the hexagon absence in the South.

The growth rates of the instability for different values of L_D are shown in Figure 1 and Figure 2 for the North and South respectively. As mentioned before, in both cases we find that the maximum growth rate (kc_i) peaks at values of m that decrease with decreasing Rossby deformation radius.

Future work includes 3D numerical models of the jets instabilities in both North and South hemispheres.

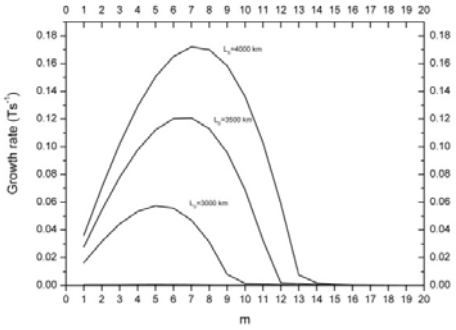

Figure 2 Growth rates of the barotropic instability for different L_D and m for the north.

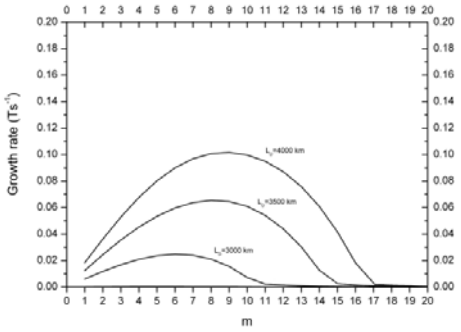

Figure 3 Growth rates of the barotropic instability for different L_D and m for the south.

Acknowledgements

A.A. is supported by a MINECO FPI PhD Studentship. This work was supported by the Spanish project AYA2012-36666 with FEDER support, Grupos Gobierno Vasco IT-765-13 and by Universidad del País Vasco UPV/EHU through grant UFI11/55.

References

[1] Antuñano A., del Río-Gaztelurrutia, T., Sánchez-Lavega, A. and Hueso, R.: Dynamics of Saturn's polar regions, J. Geophys. Res. Planets, 120, 155-176, 2015.

[2] Baines, K. H. et al.: Saturn's north polar cyclone and hexagon at depth revealed by Cassini/VIMS, Planet. Space Sci., 57, 1671-1681, 2009.

[3] Barbosa Aguiar, A. C., Read, P. L., Wordsworth, R. D., Salter, T. and Yamazaki, Y. H.: A laboratory model of Saturn's north polar hexagon, Icarus, 206, 755-763 , 2010.

[4] Godfrey, D. A.: A hexagonal feature around Saturn's north pole, Icarus, 76, 335-356, 1988.

[5] Sánchez-Lavega, A., Lecacheux, J., Colas , F. and Laques, P.: Ground-based observations of Saturn's north polar spot and hexagon, Science, 260, 329-332, 1993.

[6] Sánchez-Lavega, A., Pérez-Hoyos, S., Acarreta, J. R. and French, R. G.: No hexagonal wave around Saturn's southern pole, Icarus, 160, 216-219, 2002.

[7] Sánchez-Lavega, A. et al.: The long term steady motion of Saturn's hexagon and Geophys. Res. Lett., 41, 1425-1431 (2014).

EPSC Abstracts
Vol. 10, EPSC2015-233, 2015
European Planetary Science Congress 2015

A Y-like structure in Jupiter's equator

N. Barrado-Izagirre, J. Legarreta, E. García-Melendo, A. Sánchez-Lavega and J.M. Gómez-Forrellad
Dpto. de Física Aplicada I, ETSI de Bilbao, UPV/EHU, Alda. Urquijo s/n, 48013, Bilbao, Spain
(naiara.barrado@ehu.es / Fax: +00-34-94-6014178)

Abstract

In this work we are presenting a study of peculiar Y-shaped structures that appeared in the equatorial zone of Jupiter between September and December 2012. These low albedo structures (named Y1 and Y2) were oriented along the equator and centered on it (at latitude 0.5ºto 1ºN). By using images acquired by a worldwide network of observers contributing to the PVOL-IOPW database [3] and operating small telescopes, we have analyzed the morphology of the structures and the surrounding area as well as the dynamical evolution during their lifetime 90 and 60 days respectively. In this period of time convective activity was registered near the vertex of these structures. We have complemented the study with a set of images in ultraviolet and near infrared wavelengths obtained by the Hubble Space Telescope (HST) for this epoch. The features were not visible at 255 nm wavelengths which indicate that they were vertically thin and placed in altitude between the upper Equatorial hazes and the main cloud deck. In addition, they move faster than their surroundings. Finally, we interpret the phenomenon as the manifestation of a transient equatorially trapped Kelvin wave.

1. Introduction

The equatorial region of Jupiter is dominated by an intense and broad eastward jet about 30º wide in latitude (from 15ºN to 15ºS), with two permanent velocity maximums at the north and south boundaries of the Equatorial zone (at 6º) and a central minimum with a velocity of around 60 to 80 ms^{-1} at 0º latitude and a parabolic shape between the north and south jets [1,3 ,5]. Globally, Jupiter's equatorial jet can be seen as a symmetric double jet with maximum velocities peaks of ~ 150 ms^{-1} and a central minimum with a velocity of -70 ms^{-1} (wetsward) relative to the two jets peaks. This structure of the jet was proposed to be the result of a mixture of meridional motions related to Hadley cells and a Kelvin wave [6].

In this paper go over the detection and study of two features appeared in Jupiter's equatorial zone in the last months of 2012 ground-based and HST images. The features had a Y-like shape approximately symmetric with respect to the equator with their vertices aligned and centered on it.

2. Observations

The PVOL-IOPW database is a repository of giant planets observations contributed by an international network of amateur astronomers in the framework of the International Outer Planets Watch Atmospheres node. It stores a large number of images and it allows web-base queries with several criteria [3]. These observations allow a wide temporal coverage of Jupiter and Saturn. The quality of the observations is very variable but some observers obtain images with spatial resolutions down to 0.5'' (1500 km over the Jovian disk at opposition). They provide almost a dayly coverage around the opposition. We complement these observations with a set of images taken by the HST the 19-20 September when the Y1 was present in the atmosphere. This set contains two wavelengths', UV and NIR, images.

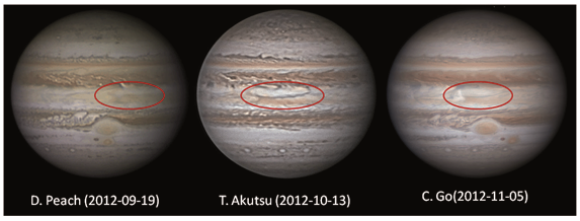

Figure 1: Visual aspect of the "Y" in three IOPW-PVOL data base images. The orientation of the planet is North up East at right.

3. Morphology, evolution and motions

Two Y-shaped structures formed and survived for months in the last quarter of 2012 at Jupiter's EZ. But contrarily to would be expected, turned over, i.e. with the open side of the 'Y' facing the minimum of

the equatorial eastward jet. The first Y feature, Y1, formed in September at 300º of longitude survived for 90 days and traveled with a longitudinal velocity of 99.4 ± 0.1 ms^{-1}. Similarly the second one appeared in October at 100º traveling with a 101.4 ± 0.6 ms^{-1} velocity for 60 days (see Figure 2).

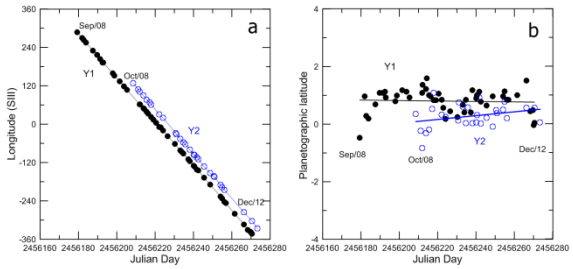

Figure 2: On the right panel we represent the drift of both features during 2012. Left panel shows the small variations suffered by Y1 and Y2 in latitude.

The Y-like structures appeared as a low albedo feature in the RGB compositions and in the HST 763 nm red wavelength images, where we observed that apparently they are moving above the ammonia cloud tops. However, in the HST UV images (255 nm wavelength) there was no evidence of the structures and only a dark patch was observed in the methane absorption band images from PVOL. These two wavelengths are sensitive to the upper atmospheric haze and high features are bright in the methane; therefore these features must be at a lower altitude. Consequently the dark clouds forming the Y-structure must be thin and located somewhere between the lower ammonia cloud and the upper ultraviolet absorbing hazes.

In November some bright spots were detected near to the vertices of Y1 and Y2. It is difficult to establish the lifetime of these spots but it must be of the order of 2-4 days. We were able to measure the area of one of those and noticed that it grew rapidly.

4. Kelvin wave hypothesis

With the aim of clarify the origin of the phenomenon we have explored the hypothesis of explaining this phenomenon as a Kelvin wave. We have used a two layer "shallow water" model [2]. The simulations that we obtain reproduce the main morphology observed in the cloud top and the properties of the Y structures, like its phase velocity when the excited layer is thin. These results suggest the manifestation of an equatorially confined Kelvin wave and its interaction with a Rossby wave.

Acknowledgements

This work was supported by the Spanish MICIIN project AYA2012-36666 with FEDER funds, by Grupos Gobierno Vasco IT-65-013 and by Universidad País Vasco UPV/EHU through program UFI11/55. The IOPW contributors are from the International Outer Planet Watch Team IOPW-PVOL:
http://www.pvol.ehu.es/pvol/index.jsp?action=iopw.

References

[1] García-Melendo, E. and Sánchez-Lavega, A.: A study of the stability of the jovian zonal winds from HST images: 1995-2000, Icarus, 152, pp. 316-330, 2001

[2]García-Melendo, E. and Sánchez-Lavega, A.: Shallow Water simulations of Saturn's Giant Storms at different latitudes, Icarus, (submitted 2015).

[3] Hueso, R. et al.: The international outer planets watch atmospheres node database of giant planet images, PSS, 59, pp. 1152-1159, 2010.

[4] Ingersoll, A.P., et al.: Dynamics of Jupiter's atmosphere. In: Bagenal, F., Dowling, T.E., Mckinnon, W.B. (Eds.), Jupiter: The Planet, Satellite and Magnetosphere. Cambridge University Press, Cambridge, UK, pp.105-128, 2004.

[5] Rogers, J.H. 1995. The Giant Planet Jupiter. Cambridge Univ. Press, New York.

[6] Yamazaki Y.H. et al.: Hadley circulations and Kelvin wave-driven equatorial jets in the atmospheres of Jupiter and Saturn. Planetary Space Science, 53, pp. 508-525, 2005.

EPSC Abstracts
Vol. 10, EPSC2015-238, 2015
European Planetary Science Congress 2015

Influence of the tides on the obliquity of Enceladus

R.-M. Baland (1,2), M. Yseboodt (2), and T. Van Hoolst (2)
(1) Université catholique de Louvain, Earth and Life Institute, Louvain-la-Neuve, Belgium,
(2) Royal Observatory of Belgium, Brussels, Belgium, (balandrm@oma.be)

Abstract

We propose a Cassini State model for Enceladus in which we assume the presence of a global ocean beneath an ice shell and include the existence of deformations induced by obliquity tides. We aim to assess whether the obliquity of Enceladus can reach values large enough to trigger a strong heat flux caused by the dissipation associated with obliquity tides.

1. Introduction

Enceladus presents plumes of water vapor and ice particles at its warm south pole, which have been interpreted as evidence of a liquid water reservoir beneath the surface [6]. Gravity, topography, and heat flux measurements are in favour of a local reservoir. However, the gravity measurements cannot rule out a global ocean [5]. Spin precession measurements and modeling may help to discriminate between the two hypotheses, since a global ocean may decouple the surface from the interior and lead to different spin precessions of the solid layers.

For a synchronous triaxial satellite, it is often assumed that the obliquity is that of the classical Cassini state, valid for uniform precession. Here, we propose to develop a new theoretical model for the Cassini State, taking into account that Enceladus experiences a nonuniform orbital precession (e.g.[3] for the Galilean satellites), may harbor an internal global ocean (e.g. [1] for Titan), and experiences periodic elastic deformations. The need for a new model comes from the hypothesis that the jets of Enceladus could be associated with a strong heat flux resulting from tidal heating, if the obliquity is larger than $0.05 - 0.1°$[7, 8]. In our modeling, we search for a resonant amplification of the solution (due to the non uniformity of the orbital precession and/or the presence of the internal global ocean and/or the elastic deformations of the solid layers). Such a resonance may lead to a high values for obliquity, as in the case for Titan [1] or Ganymede and Callisto [2].

2. Solid spin precession

When the orbital precession is uniform and the satellite is solid and rigid, the obliquity ε of the Cassini state derived from the solution of the angular momentum equation governing the spin precession is constant

$$\varepsilon = -\frac{i\dot{\Omega}}{\frac{\kappa}{C} + \dot{\Omega}}, \quad \text{with} \quad \kappa = \frac{3}{2} n (C - A) \qquad (1)$$

where $\dot{\Omega}$ is the constant orbital precession rate, i is the orbital inclination (constant if the precession is uniform), n is the mean motion, and $A < B < C$ are the principal moments of inertia. Using the measured gravity field of [5], and the orbital precession of [9], we find that $\varepsilon = 6.4\,10^{-4}$ degrees, or 2.80 m at the surface (see also [4]).

The effect of elastic deformations is to reduce the effective torque exterted by Saturn on Enceladus, in such a way that the "solid elastic obliquity" ε_{el} is given by Eq. (1) where κ is replaced by

$$\kappa = \frac{3}{2} n \left\{ (C - A) - k_2 M_e R^2 q_r \right\} \qquad (2)$$

with k_2 the Tidal Love number of the solid Enceladus, M_e and R the mass and the mean radius, and q_r the ratio of the centrifugal acceleration to the gravitational acceleration. For $k_2 = 0.015$, ε_{el} is about 1% larger than ε, and no resonant amplification occurs. Considering the nonuniform orbital precession of the satellite (see e.g. ephemerides of [9]) does not allow to find a resonant amplification neither (see Fig. 1).

3. Partially decoupled spin precession

We assume that Enceladus is made of three uniform and homogenous layers: an elastic ice shell (s), a liquid water ocean, and an elastic rock interior (i). Under the assumption that the ocean is in hydrostatic equilibrium, the system of angular momemtum equations governing the spin precessions of the different layers

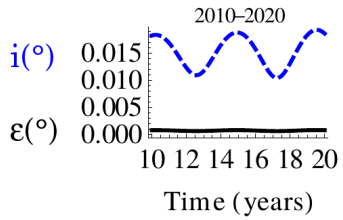

Figure 1: Orbital inclination (blue) and solid obliquity (black), of Enceladus for the period 2010-2020 and for the nonuniform orbital precession. Rigid and elastic cases for the spin obliquity are indistinguishable.

reduces to the angular momemtum equations of the solid layers [1]. They are written, correct up to the first order in spin obliquities and orbital inclination, as

$$C_s \frac{dS_s}{dt} = I\tilde{\kappa}_s(N - S_s) - I\tilde{K}_s(S_i - S_s) \quad (3)$$

$$C_i \frac{dS_i}{dt} = I\tilde{\kappa}_i(N - S_i) + I\tilde{K}_i(S_i - S_s) \quad (4)$$

where S_s and S_i are the projections on the Laplace plane of the unit vectors along the rotation axes of the shell and of the interior, respectively. C_s and C_i are the polar moment of inertia of the two solid layers. $\tilde{\kappa}'_l$ and $\tilde{K}_l$ represent the strengths of the external torque of Saturn and of the internal gravitational torque on the solid layer l, corrected for the ocean pressure and taking into account the elasticity effects. The solution of the system is characterized by an obliquity amplitude for the shell and the interior, for each term of frequency $\dot{\Omega}_j$ and amplitude i_j of the series for the orbital precession:

$$\varepsilon_{j,s} = \frac{i_j\dot{\Omega}_j(C_i\tilde{K}_i + C_s\tilde{K}_s - C_s\tilde{\kappa}_i - C_i\,C_s\,\dot{\Omega}_j)}{C_iC_s(\omega_+ + \dot{\Omega}_j)(\omega_- + \dot{\Omega}_j)}, \quad (5)$$

$$\varepsilon_{j,i} = \frac{i_j\dot{\Omega}_j(C_i\tilde{K}_i + C_s\tilde{K}_s - C_i\tilde{\kappa}_s - C_i\,C_s\,\dot{\Omega}_j)}{C_iC_s(\omega_+ + \dot{\Omega}_j)(\omega_- + \dot{\Omega}_j)}. \quad (6)$$

with $\omega_\pm$, the eigenfrequencies of the system. We compute the solution for a large range of density profiles of Enceladus. We find that the obliquity of Enceladus' shell is of the same order ($\sim 6\,10^{-4}$ deg) as the obliquity of the solid case and that elasticity has an effect of at best a few percents on the solution.

4. Summary and Conclusions

We conclude that both the hypotheses of a local reservoir or of a global ocean fail to reach large obliquity values satisfying the requirements of [7, 8], even when nonuniform orbital precession and/or elastic tidal deformations are considered. We reach similar conclusions as previous study [4], that is to say that the origin of the strong heat flux of Enceladus is unlikely to be the dissipation associated with the obliquity tides.

Acknowledgements

R.M.B. is funded by a FSR (Fonds Spécial de Recherches) grant from UCL

References

[1] Baland, R.-M., Van Hoolst, T., Yseboodt, M., and Karatekin, Ö.: Titan's obliquity as evidence of a subsurface ocean?, Astronomy & Astrophysics, Vol. 530, ID. A141, 2011.

[2] Baland, R.-M., Yseboodt, M., and Van Hoolst, T.: Obliquity of the Galilean satellites: The influence of a global internal liquid layer, Icarus, Vol. 220, pp. 435-448, 2012.

[3] Bills, B.G.: Free and forced obliquities of the Galilean satellites of Jupiter, Icarus, Vol. 175, pp. 233-247, 2005.

[4] Chen, E.M.A, and Nimmo, F.: Obliquity tides do not significantly heat Enceladus, ICarus, Vol. 214, pp. 779-781, 2011.

[5] Iess, L., and 10 colleagues: The Gravity Field and Interior Structure of Enceladus, Science, Vol. 344, pp. 78-80, 2014.

[6] Porco, C.C., and 24 colleagues: Cassini Observes the Active South Pole of Enceladus, Science, Vol. 311, pp. 1393-1401, 2006.

[7] Tyler, R.H.: Ocean tides heat Enceladus, Geophysical Research Letters, Vol. 36, p. L15205, 2009.

[8] Tyler, R.H.: Tidal dynamical considerations constrain the state of an ocean on Enceladus, Icarus, Vol. 211, pp. 770-779, 2011.

[9] Vienne, A., and Duriez, A.: TASS1.6: Ephemerides of the major Saturnian satellites, Astronomy & Astrophysics, Vol. 297, p. 588, 1995.

EPSC Abstracts
Vol. 10, EPSC2015-253, 2015
European Planetary Science Congress 2015

Investigation of Titan's surface and atmosphere photometry using the VIMS instrument onboard Cassini

Thomas Cornet (1), Nicolas Altobelli (1), Sébastien Rodriguez (2), Luca Maltagliati (2), Stéphane Le Mouélic (3), Christophe Sotin (3,4), Robert H. Brown (5), Jason W. Barnes (6), Bonnie J. Buratti (4), Kevin H. Baines (4), Roger N. Clark (7) and Phillip D. Nicholson (8).
(1) European Space Agency (ESA), European Space Astronomy Centre (ESAC), PO BOX 78, Villanueva de la Cañada (Madrid), Spain (tcornet@sciops.esa.int). (2) Laboratoire AIM, CEA/Saclay, Gif/Yvette, France. (3) LPG Nantes, UMR 6112 CNRS, Université de Nantes, Nantes, France. (4) Jet Propulsion Laboratory (JPL), Pasadena, CA, USA. (5) University of Arizona, Tucson, AZ, USA. (6) University of Idaho, Moscow, ID, USA. (7) Planetary Science Institute (PSI), Tucson, AZ, USA. (8) Cornell University, Ithaca, NY, USA.

Abstract

After 110 targeted flybys of Titan in a decade, the Cassini Visual and Infrared Mapping Spectrometer (VIMS) instrument acquired more than 34,000 hyperspectral cubes pointing at the surface of Titan on the dayside. Due to the strong influence of the absorbing and scattering atmosphere and of the heterogeneous viewing geometry of the flybys, retrieving Titan's surface and atmosphere normal albedo values extracted from the VIMS data remains challenging. In the present work, we aim to determine appropriate photometric functions to describe the light scattering in Titan's atmosphere, which could be used as a basis for empirical corrections or Radiative Transfer (RT) calculations to retrieve normal albedo values for the surface and the atmosphere.

1. Introduction

Titan's surface is only visible with VIMS in the infrared in 7 spectral atmospheric windows centred at 0.93, 1.08, 1.27, 1.59, 2.01, 2.7-2.8 and 5 μm [1]. Atmospheric scattering and absorption dominate Titan's spectrum at wavelengths shorter than 3 microns, while the 5 μm window has a reduced atmospheric scattering contribution to the signal recorded by VIMS [2].
We focus our study on the images acquired at the edges of each atmospheric window to determine the light scattering properties of the atmosphere. In order to explore the angular dependencies of the I/F over Titan, the entire VIMS Ta-T110 data set is decomposed into a MySQL relational database from which we extract angular and time tends on precise location or wavelength subsets. Our first fitting tests are performed on a reduced particular data set acquired at T88 to avoid time variations.

2. The T88 "EPF" observation

An "Emergence-Phase Function'' (or EPF) observation has been acquired during the T88 flyby. It consists of 25 cubes targeting the same area at a constant incidence angle of ~51^{o} and with varying emergence and phase angles (from 0 to 60^{o}).
Figure 1 shows the angular trends of the I/F with wavelength. The data clearly exhibit an increase of I/F at 5 μm at low phase angles, which is usually indicative of an opposition effect of planetary surfaces [3], already observed by Huygens/DISR [4]. In the short-wavelength windows, a "kink" and a sharp increase in the I/F are seen respectively at low and high emergence and phase angles. These effects strengthen with decreasing wavelength. They are also present in the images taken at wavelengths where the atmosphere is completely opaque, which clearly indicates that the shape of the curves is controlled by atmospheric effects. To decouple the surface-atmosphere problem, we first focus on the modelling of the atmospheric scattering and absorbing properties at the edges of the atmospheric windows.

3. Atmospheric model

Assuming that the atmosphere is a particulate medium that prevent any opposition effect, we use the simple Hapke ISMA model (Eq. 1 [3]) to take into account the effects of a multiply scattered

radiation (in a plane parallel approximation). The scattering anisotropy is given by the single-scattering term of Eq. 1 (particle phase function $P_{atm}(g)$), the multiple scattering $M(\omega_0,\mu_0,\mu)$ being isotropic.

$$\frac{I}{F} = \frac{\omega_{0,atm}}{4}\frac{1}{\mu_0+\mu}\left[P_{atm}(g) + M(\mu_0,\mu)\right]\left[1 - e^{-\tau_{atm}\left(\frac{1}{\mu_0}+\frac{1}{\mu}\right)}\right] \quad (1)$$

We take into account the coupling between the haze and gas in $\omega_{0,atm}$, $P_{atm}(g)$ and τ_{atm} [5]. Because the single-scattering albedo of the gas is very low, the phase function for the total atmosphere is mainly controlled by that of the haze, for which we use a Henyey-Greenstein function with 2 lobes (*b*: size of the lobe, *c*: direction of scattering). Figure 2 shows a fit example taken at 1.14 µm as well as the $P_{atm}(g)$ parameters determined at each of the atmospheric wavelength investigated (average value of *b*~0.27+/-0.05 and *c*~-0.52+/-0.2). Our parameters fall into the "irregular particles" domain of the "*b* VS *c*" diagram [3], which seems quite consistent with the expected fractal aggregate shape of Titan's large aerosols particles.

4. Summary

We are using the VIMS Ta-T110 data in order to determine the photometric functions of the surface and of the atmosphere. We started our study on the T88 EPF observation by fitting phase curves of atmospheric images using simple analytical laws. We found a set of parameters that are consistent with the fact that the aerosols are irregular particles, forward scattering with a rather large lobe. Future work will include the study of the other atmospheric windows to infer surface properties, and particularly the 5 µm window where the phase curve shape differs from the other.

Acknowledgements

Part of this work has been funded by the ESAC Faculty. TC is funded by the ESA Research Fellowship Programme in Space Science.

References

[1] Sotin, C. et al., Nature, 2005.

[2] Rodriguez, S. et al., PSS, 2006.

[3] Hapke, B., Cambridge Univ. Press, 2012.

[4] Schröder, S., and Keller, H.U., PSS, 2009.

[5] Hayne, P. et al., Icarus, 2014.

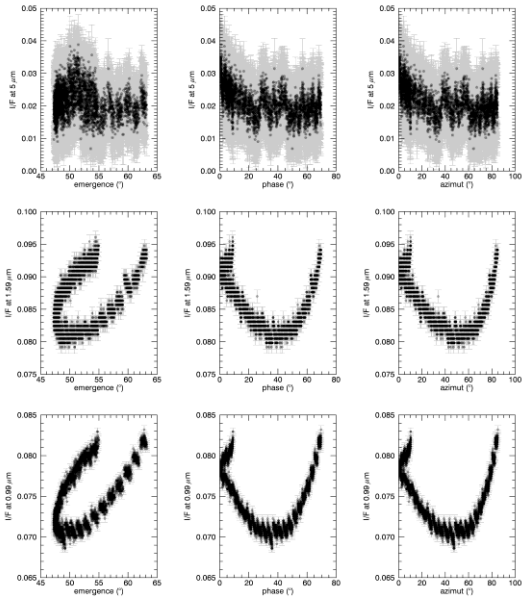

Figure 1: Angular trends of the VIMS I/F at 5 µm, 1.59 µm and 0.99 µm.

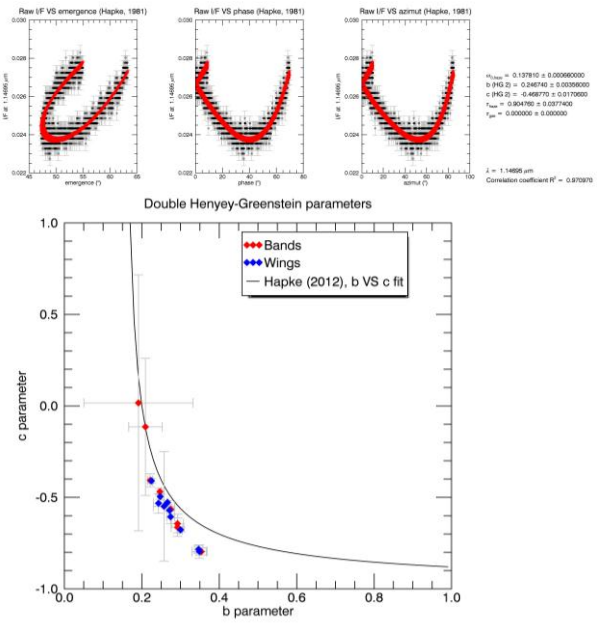

Figure 2: top: fit of the 1.14 µm data with Eq. (1). **Bottom:** Henyey-Greenstein parameters determined at each atmospheric wavelength investigated represented in the "b versus c" diagram.

EPSC Abstracts
Vol. 10, EPSC2015-285, 2015
European Planetary Science Congress 2015

Spectral detectability of CH_4-N_2 clathrates for in-situ and remote observation of Titan and other icy moons

D. Nna-Mvondo, G. Tobie, E. Le Menn, O. Grasset

Laboratoire de Planétologie et Géodynamique, LPG Nantes, CNRS UMR 6112, Université de Nantes, France (delphine.nnamvondo@univ-nantes.fr)

Abstract

Multicomponent clathrates may be present at the surface of several icy moons, although they have not been detected yet, possibly due to the absence of reliable spectral data. In this work, we present infrared (IR) and Raman spectral studies of CH_4-N_2 clathrates at low temperature and pressure, in order to identify discriminating criteria for their possible detection. These clathrates are particularly interesting for Titan and Pluto. Our experimental results indicate that identification of mixed clathrate from remote sensing is very challenging, and that only in-situ Raman spectroscopy may provide a clear identification of clathrate and constraints on their composition.

1. Introduction

Clathrate hydrates are expected to be present at the surface and in the subsurface of many icy moons [1]. Several gas compounds such as CO_2, CH_4 or N_2 are known to easily combine with water molecules to form clathrate hydrates at the temperature and pressure conditions of many icy moons and can be trapped simultaneously, leading to the formation of multicomponent clathrates. For example, on Titan, many atmospheric compounds, such as N_2, CH_4, C_2H_6 and other light hydrocarbons, are likely to be incorporated in subsurface reservoirs of multicomponent clathrates as they are stable relative to water ice at surface conditions [1]. The presence of clathrate hydrates in icy moons may be especially relevant in Planetary Sciences and Astrobiology. They probably play a key role in the storage and transport of gas compounds in water-rich environments [2]. Consequently, they could possibly act as a transporting agent of potential nutrients and products of biological activity, from the deep interior to the icy shell [3]. The detection of clathrates on Titan's surface, and more extensively on icy planetary surfaces, could be of crucial importance in understanding their role and constraining their relevance in the chemical processes occurring in the outer Solar System. Studies on methane clathrates, applied to Earth and planetary icy bodies, have been carried out to a large extent. However, experimental measurements for multicomponent clathrates are still scarce or non-existent, and therefore have to be addressed. In the present study, we focus on CH_4-N_2 mixed clathrates, which are the dominant species at Titanôs surface. Similar analysis will be extended to other gas compounds in the future.

2. Laboratory experiments

CH_4-N_2 Clathrate samples were synthesized in an autoclave combined with a cooling system and a multi-gas mixer. Few ml of deionized water was introduced in the autoclave and pressurized with the N_2 and CH_4 gases for a couple of days, at controlled low temperature and low pressure, within the field of formation and stability of the clathrate. The clathration rate and molar composition of clathrates were previously monitored and quantified by gas chromatography (GC). The spectral characterization, at low temperature (94K) and under vacuum (10^{-5} bar), was performed by FTIR reflectance spectroscopy in the mid-near IR (2000 - 10000 cm^{-1}) and Raman spectroscopy from 50 to 4000 cm^{-1}, using an Liq N_2-cooled cryostat (Fig. 1).

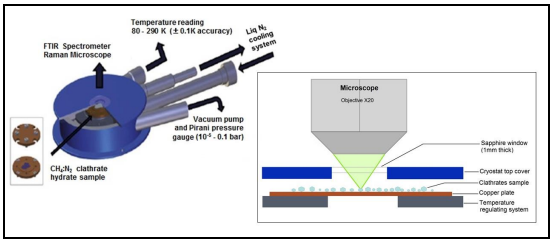

Figure 1: Cooled cryostat used for the spectroscopy.

3. Results

IR and Raman spectra were obtained for different CH_4 molar fractions in the CH_4-N_2 clathrates, varying from 0.30 to 1. For each clathrate composition, a dozen of single crystals were analyzed (Fig. 2).

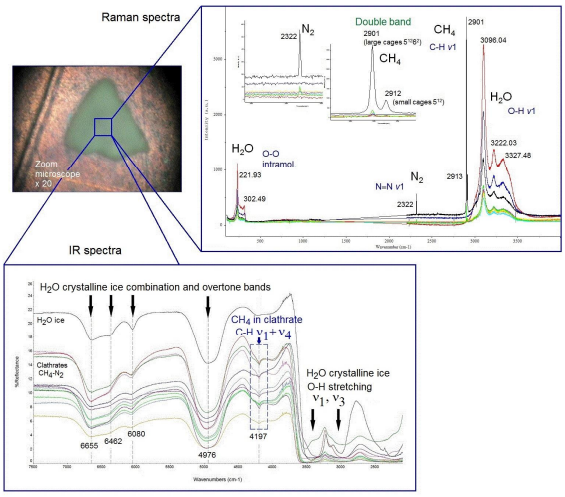

Figure 2: Example of Raman and IR spectra obtained for 0.62/0.38 CH_4-N_2 clathrates.

The CH_4 double peak in Raman at 2901 cm^{-1} (higher intensity) and 2913 cm^{-1} (smaller intensity) is a characteristic signature of the large and small cages of the sI clathrate structure. It is also observed the N_2 vibration band at 2322 cm^{-1} of sI small/large cage type and the vibration of H_2O within the hydrate structure at 221 cm^{-1}, 302 cm^{-1} and 3096 cm^{-1}. For IR spectra, the position and shape of the main absorption bands of the clathrates are very similar to those of pure crystalline water ice. The ice matrix dominates the IR signature. However, the vibration of C-H in the first combination mode ν1 + ν4 appears at 4197 cm^{-1} showing the presence of CH_4 trapped in the clathrate cages. We conducted various quantitative studies consisting in examining if the ratios of the areas and heights of the CH_4, N_2 and H_2O bands detected in IR and Raman spectroscopy (ratios of CH_4/N_2, CH_4/H_2O, N_2/H_2O and $CH_{4\text{large cages}}/CH_{4\text{small cages}}$) could be related to the composition of the gas guests sequestered in the clathrates. We have found that only the CH_4/N_2 band ratio in Raman spectroscopy can be a reliable measure to determine the molar composition of such binary clathrates, as both variables are clearly related together by an exponential proportionality (Fig. 3).

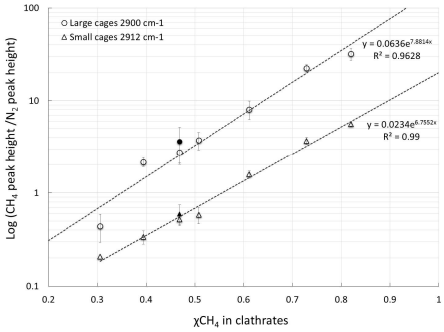

Figure 3: Variation of the ratio of peak heights of CH_4 over the peak heights of N_2 for large (○) and small cages (△) as a function of the molar composition of clathrates. Plain symbols (●▲) are spectra taken under room atmosphere for comparison.

4. Conclusions

Due to the weak appearance of the absorption band of trapped CH_4 with respect to the strong H_2O-ice matrix absorption, it may be problematic to detect CH_4-N_2 clathrates on icy surface from IR remote sensing, using instruments such as Cassini-VIMS. In any case, IR signatures would not allow the characterization of the clathrate composition. In contrast, our Raman analyses indicate that in-situ Raman investigation is a very promising technique for detecting easily and efficiently multicomponent clathrates and for quantifying the sequestered gases in planetary ices.

Acknowledgements

The research leading to this work has received funding from the European Research Council under the European Communityôs Seventh Framework Programme (FP7/2007-2013 Grant Agreement No. 259285).

References

[1] Choukroun, M., Kieffer, S., Lu, X., Tobie G.: Clathrate Hydrates: Implications for Exchange Processes in the Outer Solar System, The Science of Solar System Ices, Springer New York, pp 409-454, 2013.

[2] Tobie, G., Lunine, J.I., Sotin, C.: Episodic outgassing as the origin of atmospheric methane on Titan, Nature, Vol. 440 (7080), pp. 61-64, 2006.

[3] Tobie, G., Choblet, G., Sotin, C.: Tidally heated convection: Constraints on Europa's ice shell thickness, J. Geophys. Res.: Planets, Vol. 108 (E11), 5124, 2003.

EPSC Abstracts
Vol. 10, EPSC2015-302, 2015
European Planetary Science Congress 2015

Stratospheric benzene and hydrocarbon aerosols in Saturn's auroral regions

S. Guerlet (1), T. Fouchet (2), S. Vinatier (2), A.A. Simon (3), E. Dartois (4) and A. Spiga (1)
(1) Laboratoire de Météorologie Dynamique/IPSL/CNRS, Paris, France (2) LESIA/Observatoire de Paris, Meudon, France (3) NASA/GSFC, Greenbelt, MD, USA (4) IAS, Orsay, France (sandrine.guerlet@lmd.jussieu.fr)

Abstract

Saturn's polar upper atmosphere exhibits significant auroral activity, however, its impact on stratospheric chemistry (*i.e.* the production of benzene and heavier hydrocarbons) and thermal structure is poorly documented. Here we report on the first measurement of benzene column abundance in Saturn's polar stratosphere, together with the first detection of spectral signatures of the polar haze in the thermal infrared, based on limb measurements from the Composite Infrared Spectrometer (CIRS) on board Cassini. We then evaluate the radiative impact of the polar haze.

1. Introduction

Saturn's polar regions are characterized by permanent dark polar caps in the UV, generally attributed to the presence of polar stratospheric hazes ([2, 3]) possibly produced by the precipitation of energetic auroral electrons ([4]). The aerosol sizes and optical properties have been derived in the UV and visible from HST observations ([5, 6]) but little is known about their infrared properties or radiative impact. In parallel, the disk-average benzene (C_6H_6) column density has been measured in the stratospheres of Jupiter and Saturn from ISO ([7]). Modeling studies suggest that ion chemistry plays a key role in producing benzene and polar aerosols in Jupiter's polar atmosphere (eg., [8]), but the role of ion chemistry has not been studied in the case of Saturn's atmosphere. In this context, our goal is to search for tracers of ion chemistry (benzene and aerosols) in Saturn's neutral stratosphere.

2. Cassini/CIRS data analysis

2.1 Temperature retrievals

We analyse four datasets acquired in limb viewing geometry between 2007 and 2012 by the Composite Infrared Spectrometer onboard Cassini at latitudes 40°N, the equator, 35°S and 80°S (within the polar cap). The thermal emission of Saturn's atmosphere was recorded in the range 580–1480 cm^{-1} with a spectral resolution between 0.5 cm^{-1} and 1.5 cm^{-1}. We first employ the forward radiative transfer model coupled to the bayesian inversion method described in [9] to retrieve vertical temperature profiles from the analysis of the ν_4 methane band (1200–1370 cm^{-1}) and of the H_2-H_2 and H_2-He collision-induced emission (590–660 cm^{-1}). These profiles are constrained between 20 mbar and a few μbar. Secondly, vertical profiles of the volume mixing ratio of various hydrocarbons can be retrieved from the analysis of their emission bands.

2.2 Benzene retrievals

A benzene emission band at 673 cm^{-1} is clearly detected at 80°S (Fig. 1) and more marginally at 40°N. We find that the retrieved benzene profiles are very sensitive to the choice of the prior profile, but that the C_6H_6 column density integrated between 3-mbar and 0.2-mbar is a robust quantity. Upper limits are derived at the equator and 35°S. Benzene is found slightly enhanced at 80°S compared to other latitudes. In contrast, the photochemical model of [1] (which only includes neutral chemistry) predicts a maximum benzene abundance at the equator, and about 50 times less at 80°S. This suggests that ion chemistry plays a key role in producing benzene in Saturn's polar stratosphere, similarly to Jupiter's stratosphere.

2.3 Aerosol retrievals

At 80°S, after the retrieval of the temperature and hydrocarbon profiles, our best-fit spectra still do not match the observations in several spectral regions (see Fig. 2) and we additionally retrieve aerosol opacity profiles in small, independent, spectral regions (10 to 20 cm^{-1} wide) to derive the spectral dependency of the haze opacity. These profiles are constrained between ∼3 mbar and 0.1 mbar. The haze integrated

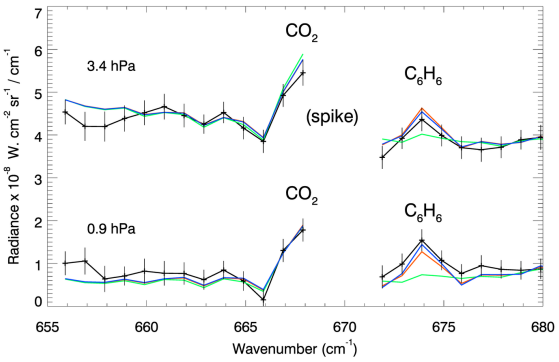

Figure 1: Cassini/CIRS limb spectra acquired at two different tangent pressure levels at 80°S (in black). Best-fit synthetic spectra are overplotted, corresponding to the retrieval of the CO_2 mixing ratio alone (in green, no benzene opacity) or to the simultaneous retrieval of CO_2 and C_6H_6 mixing ratios (in blue and red, assuming different C_6H_6 vertical distributions).

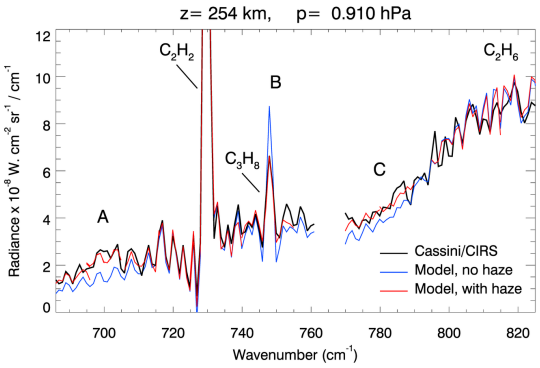

Figure 2: Cassini/CIRS limb spectra acquired at 80°S compared with best-fit synthetic spectra, with or without including the retrieval of haze opacity. A, B and C highlight the location of the main aerosol signatures.

opacity exhibits distinct spectral bands centered at 700, 750, 780, 1390 and 1450 cm^{-1}, similarly to Titan's aerosol signatures in the thermal infrared, which have been assigned to vibration modes of aliphatic and aromatic hydrocarbons [10].

We then evaluate the radiative impact of this polar haze on the thermal structure using a seasonal radiative-convective model of Saturn's atmosphere [11]. We assume that aerosols are spherical particle aggregates with a radius of 0.1 μm and use Mie scattering theory to compute their extinction coefficient. We find that the polar haze induces a net stratospheric heating during summer reaching +6 K at the 10-mbar pressure level, and a net stratospheric cooling during winter reaching -5 K at and above the 0.1-mbar pressure level.

3. Summary and Conclusions

On Saturn's auroral region (80°S), benzene is found slightly enhanced compared to its equatorial and mid-latitude values. This contrasts with the photochemical model of [1] and advocates for the inclusion of ion-related reactions in Saturn's chemical models. The polar stratosphere is also enriched in aerosols, with spectral signatures consistent with aromatic and aliphatic hydrocarbons. We estimate this polar haze to warm the middle stratosphere by 6K in summer, hence it could partly account for the warm polar hood observed in Saturn's summer stratosphere.

Acknowledgements

Part of this work was funded by the French ANR under grant agreement ANR-12-PDOC-0013.

References

[1] Moses, J. and Greathouse, T., J. Geophys. Res. Vol. 110, p. 9007, 2005.

[2] West, R. A. et al., Advances in Space Research Vol. 3, p.45-48, 1983.

[3] Karkoschka, E. & Tomasko, M. G., Icarus Vol. 106, p. 428, 1993

[4] Pryor, W. R. & Hord, C. W., Icarus Vol. 91, p. 161-172, 1991.

[5] Karkoschka, E. & Tomasko, M., Icarus, vol. 179, p. 195-221, 2005.

[6] Pérez-Hoyos, S. et al., Icarus Vol. 176, p. 155-174, 2005.

[7] Bézard, B. et al., Icarus Vol. 154, p. 492-500, 2001.

[8] Wong, A.-S., Yung, Y. L., & Friedson, A. J., Geophys. Res. Let. Vol. 30, p. 1447, 2003.

[9] Guerlet, S. et al. , Icarus Vol. 203, p. 214-232, 2009.

[10] Vinatier, S. et al., Icarus Vol. 219, p. 5-12, 2012.

[11] Guerlet, S. et al., Icarus Vol. 238, p. 110-124, 2014

EPSC Abstracts
Vol. 10, EPSC2015-314, 2015
European Planetary Science Congress 2015

Comparative Planetary Atmospheres of Pluto and Triton

D. F. Strobel (1), X. Zhu (2)
(1) Johns Hopkins University, Baltimore, Maryland, USA, (strobel@jhu.edu/+1 410-51607933) (2) Johns Hopkins University Applied Physics Laboratory, Laurel, Maryland,USA

Abstract

Both atmospheres of Pluto and Neptune's largest satellite Triton have cold surfaces with similar surface gravities and atmospheric surface pressures. We have updated the Zhu et al. *Icarus* **228**, 301, 2014) model for Pluto's atmosphere by adopting Voigt line profiles in the radiation code with the latest spectral database and extended the model to Triton's atmosphere by including additional parameterized heating due to the magnetospheric electron energy deposition. Numerical experiments show that the escape rate of an atmosphere for an icy planetary body similar to Pluto or Triton is quite sensitive to the methane abundance and planetary surface gravity. Together this leads to a cumulative effect on the density variation with the altitude that significantly changes the atmospheric scale height at the exobase together with the exobase altitude. The atmospheric thermal structure near the exobase is sensitive to the atmospheric escape rate only when it is significantly greater than 10^{26} molecules s^{-1} above which an enhanced escape rate corresponds to a stronger radial velocity that adiabatically cools the atmosphere to a lower temperature.

1. Introduction

In the outer solar system, Pluto and Triton are widely regarded as the largest end-members of Kuiper-Belt objects and as "twins" with thin buffered N2 atmospheres controlled by interactions with surface ice, primarily N2 frost. There are substantial differences between the atmospheres of Pluto and Triton at the microbar level where stellar occultation measurements probe. Pluto's scale height and temperature are about twice Triton's values. In the altitude range 25–150 km the atmospheric structure of Triton has a steep thermal gradient above 50 km altitude, with a nearly isothermal profile below [2]. The upper part of the profile can be explained by downward conduction of heat deposited by magnetospheric electrons and solar UV. However below 50 km, the atmospheric temperature is too cold for any known constituent to radiate away the inferred heat flux from the upper atmosphere. Why Triton has what would appear to be a thick troposphere, while Pluto has at most a thin planetary boundary layer will be discussed [3]. We confirm that magnetospheric electron energy deposition is necessary to explain the Voyager derived 100 K thermosphere on Triton.

References

[1] Zhu, X., Strobel, D. F., Erwin, J. T., The Density and Thermal Structure of Pluto's Atmosphere and Associated Escape Processes and Rates, *Icarus* **228**, 301-314, 2014.

[2] Elliot, J. L., D. F. Strobel, X. Zhu, J. A. Stansberry, L. H. Wasserman, and O. G. Franz, The Thermal Structure of Triton's Middle Atmosphere, Icarus, 143, 425-428, 2000.

[3] Zalucha, A. M., X. Zhu, A. A. S. Gulbis, D. F. Strobel, and J. L. Elliot, An analysis of Pluto's troposphere using stellar occultation light curves and an atmospheric radiative-conductive-convective model, Icarus, 214, 685-700, doi:10.1016/j.icarus.2011.05.015, 2011.

EPSC Abstracts
Vol. 10, EPSC2015-320, 2015
European Planetary Science Congress 2015

ALMA observations of Titan : Vertical and spatial distribution of nitriles

R. Moreno, E. Lellouch, S. Vinatier (1), M. Gurwell (2) A. Moullet (3) L.M. Lara (4) T. Hidayat (5)
(1) LESIA, Obs. Paris-Meudon, France, raphael.moreno@obspm.fr, (2) Harvard-Smithsonian CfA, MA, USA, (3) NRAO, Charlottesville, VA, USA (4) IAA-CSIC, Granada, Spain, (5) Department of Astronomy and Bosscha Observatory, ITB, Bandung, 40132, Indonesia.

Abstract

We report submm observations of Titan performed with the ALMA interferometer centered at the rotational frequencies of HCN(4-3) and HNC(4-3), i.e. 354 and 362 GHz. These measurements yielded disk-resolved emission spectra of Titan with an angular resolution of ~0.47''. Titan's angular surface diameter was 0.77''.
Data were acquired in summer 2012 near the greatest eastern and western elongations of Titan at a spectral resolution of 122 kHz ($\lambda/d\,\lambda = 310^6$).

We have obtained maps of several nitriles present in Titan' stratosphere: HCN, HC_3N, CH_3CN, HNC, C_2H_5CN and other weak lines (isotopes, vibrationnally excited lines).

We will present radiative transfer analysis of the spectra acquired. With the combination of all these detected rotational lines, we will constrain the atmospheric temperature, the spatial and vertical distribution of these species, as well as isotopic ratios.

Moreover, Doppler lineshift measurements will enable us to constrain the zonal wind flow in the upper atmosphere.

1. Figures

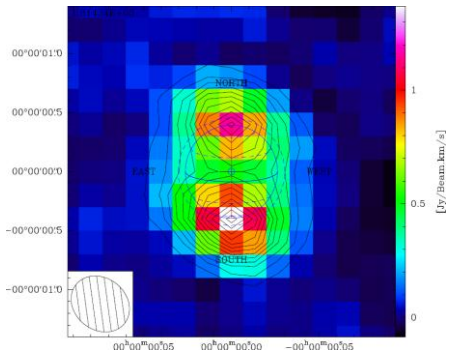

Figure 1: HC_3N map of Titan performed with ALMA. The blue circle corresponds to the surface radius. The beam size in shown in the lower left corner.

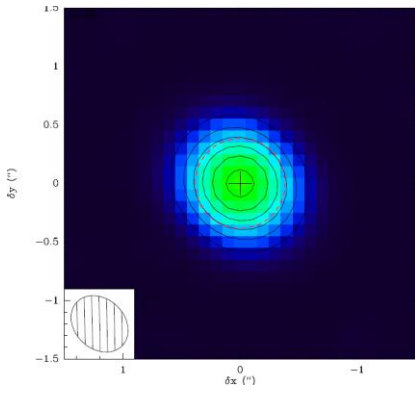

Figure 2: Continuum map of Titan at 356 GHz.

Acknowledgements

ALMA is a partnership of ESO (representing its member states), NSF (USA) and NINS (Japan), together with NRC (Canada) and NSC and ASIAA (Taiwan), in cooperation with the Republic of Chile. The Joint ALMA Observatory is operated by ESO, AUI/NRAO and NAOJ

EPSC Abstracts
Vol. 10, EPSC2015-326, 2015
European Planetary Science Congress 2015

A New Map of Io's Volcanic Heat Flow

A. G. Davies (1), G. J. Veeder (2), T. V. Johnson (1) and D. L. Matson (2).
(1) Jet Propulsion Laboratory – California Institute of Technology, Pasadena, CA, USA, (2) Bear Fight Institute, Winthrop, WA, USA. (Ashley.Davies@jpl.nasa.gov / Tel: +001-818-393-1775)

Abstract

A global heat flow map has been created from the quantification of thermal emission from 242 volcanic centers [1]. This map shows concentrations of thermal emission that are different from the concentration of active volcanic centres, and that the pattern of volcanic heat flow observed on the surface of Io is not matched by current models of deep and shallow tidal heating.

1. Introduction

It has long been assumed that the distribution of Io's surface heat flow should reflect the depth and magnitude of interior tidal heating (see review in [1]). Heating deep in the mantle should lead to a preponderance of surface heat flow at Io's poles. Mostly shallow aesthenospheric heating should manifest as enhanced heat flow at sub- and anti-jovian longitudes, although it has long been accepted that a mixture of deep and shallow heating is probable. However, recent work examining the longitudinal and latitudinal distribution of heat flow [2] and the distribution of paterae and a subset of hot spots [3] shows an offset in the peaks of thermal emission and hot spot locations that cannot be explained by current interior heating models. In order to examine this phenomenon more closely we have created a map that shows the distribution of volcanic thermal energy on Io, having quantified the thermal emission from 250 volcanic centres [2].

2. Volcanic heat flow data

Our data are primarily from spacecraft and ground based telescope observations at infrared wavelengths. Previous work [4-6] shows that a preponderance of Io's volcanic thermal emission comes from paterae. The thermal emission from Io's volcanic centres spans six orders of magnitude. In a series of papers [2,4-6] we have quantified and tabulated the thermal emission from 242 volcanic centres of ongoing or recent volcanic activity and an additional 8 outburst eruptions to establish Io's background volcanic activity during the *Voyager-Galileo* epoch. As outburst eruptions are transitory and only account for a small percentage (< 2%) of Io's yearly volcanic heat flow [1], we currently omit them from the Io volcanic heat flow map. We account for approximately 54% of Io's global average heat flow of 1.05×10^{14} W from our ground-based observations [5-7]. The area covered by all of the thermal sources, mostly dark-floored (low-albedo) paterae and dark lava flow fields, is only 2% of Io's surface. The average heat flow from Io's volcanically active areas is 68 W m^{-2} [2]. The remaining "unaccounted" heat flow, if averaged over Io's non-volcanically-active surface, is equivalent to a conducted heat flow of 0.98 ± 0.2 W m^{-2} [2], still much greater than the mean heat flow of the Earth (0.07 W m^{-2} [8]) and the Moon (0.03 W m^{-2} [9]).

3. Heat Flow Map

The heat flow map and comparison with locations of volcanic centres and different heat flow models are shown in Fig. 1. As previously noted, we find a non-uniform distribution of heat flow. The end-member heating models are not well matched. The sub-jovian point, (0° W) where aesthenospheric heating alone would generate a peak in surface heat flow, is notable for a lack of large or powerful volcanic centres, and a relatively low regional heat flow. Anti-jovian hemispheric heat flow (90°-180°-270°W) is more variegated.

4. Summary

The volcanic heat flow map strongly suggests that existing models of Io's interior heating do not fully explain the observed surface heat flow. Uncertainty remains over "unaccounted" heat flow, which may be tied to anomalously high temperature polar regions.

A dedicated Io mission [10,11] would establish global temperature distribution and provide further constraints on evolving interior heat flow models. Heat flow map comparison with geology [12 and topography [13] may be illuminating.

Acknowledgements

This work was performed at the Jet Propulsion Laboratory-California Institute of Technology and the Bear Fight Institute under contract to NASA. AGD and GJV were supported by grants from the NASA OPR Program. © Caltech, 2015.

References

[1] Davies, A. G. (2007) *Volcanism on Io – A Comparison with Earth*, Cambridge University Press.
[2] Veeder, G. J., et al. (2015) *Icarus*, 245, 379-410.
[3] Hamilton, C., et al. (2013) *EPSL*, 361, 272-286.
[4] Veeder, G. J., et al. (2009) *Icarus*, 204, 239-253.
[5] Veeder, G. J., et al. (2011) *Icarus*, 212, 236-261.
[6] Veeder, G. J., et al. (2012) *Icarus*, 219, 701-722.
[7] Veeder, G. J., et al. (1994) *JGR*, 99, 17095-17162.
[8] Turcotte, D. and Schubert, G. (1986) *Geodynamics*, Wiley.
[9] Langseth, M. G. et al. (1972) *Earth, Moon & Planets*, 4, 390-410.
[10] McEwen, A. S. et al. (2012) *Acta Astron.*, 93, 539-544.
[11] McEwen, A. S, et al. (2015) *LPSC 46*, The Woodlands, TX, abstract 1627.
[12] Williams, D. A. et al. (2011) *Icarus* 214, 91–112.
[13] White, O. et al. (2014) *JGR-Planets*, 119, 6, 1276-1301.

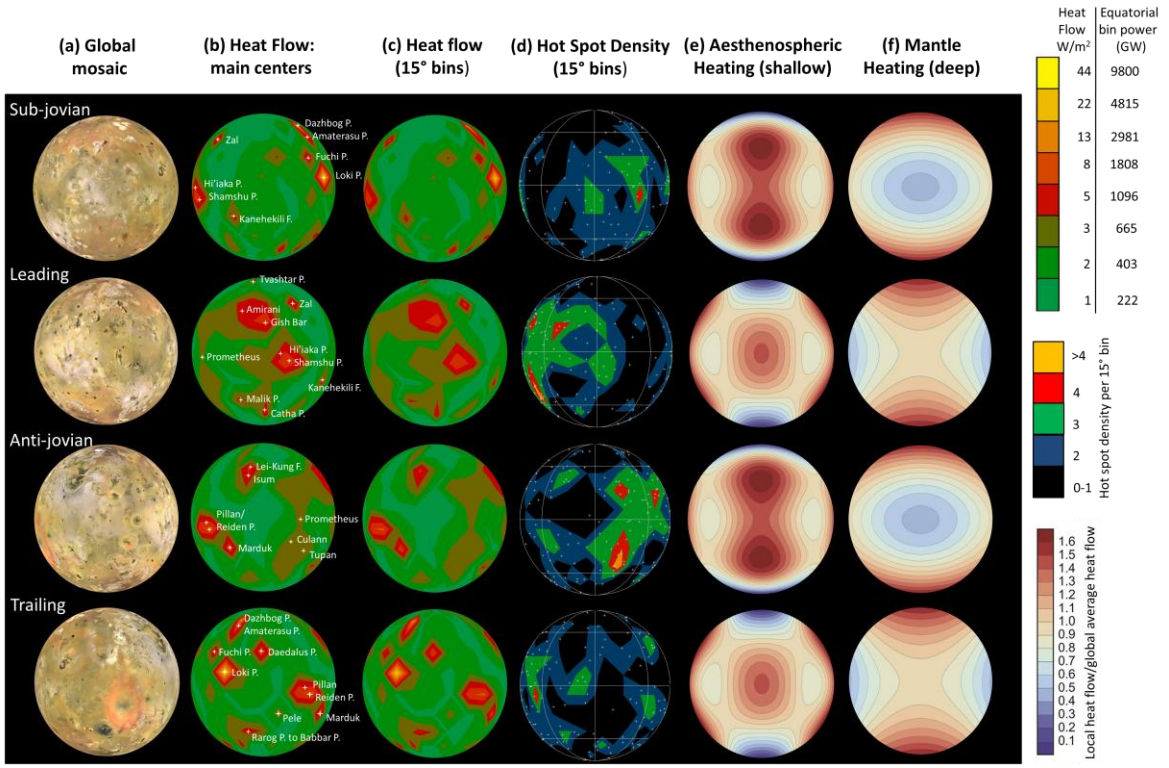

Figure 1. Io's surface heat flow (cols. b and c) compared with active volcano density (col. d), the Io USGS global mosaic (col. a), and end-member models of expected heat flow from shallow aesthenospheric heating (col. e) and deep mantle heating (col. f). Data have been re-projected to show the sub-jovian, leading, anti-jovian and trailing hemispheres of Io. The deep and shallow model heat flow plots were adapted from images in [3]. Outburst eruptions are excluded. There are three scales on the right. Top scale: for columns b and c; i.e., heat flow in W/m^2 per 15° bin (first column) and heat flow per bin on the equator (second column). Middle scale: for column d (hot spot density). Bottom scale: for columns e and f (end-member heating models).

EPSC Abstracts
Vol. 10, EPSC2015-330, 2015
European Planetary Science Congress 2015

Possible evidence for a methane source in Enceladus' ocean

Alexis Bouquet (1,2), Olivier Mousis (3), J. Hunter Waite (2), and Sylvain Picaud (4)
(1) University of Texas at San Antonio, Department of physics & Astronomy, San Antonio, Texas, USA (2) Southwest Research Institute (6220 Culebra Road, San Antonio, TX 78228, USA), (3) Aix Marseille Université, CNRS, LAM (Laboratoire d'Astrophysique de Marseille) UMR 7326, 13388, Marseille, France (4) Université de Franche-Comté, Institut UTINAM, CNRS/INSU, UMR 6213, Observatoire des Sciences de l'Univers de Besançon, France
(alexis.bouquet@gmail.com)

Abstract

We have investigated the evolution of the composition of the putative internal ocean of Enceladus. We used a thermodynamical statistical model to assess the formation of clathrate hydrates in an ocean with the composition of the plumes observed by the Cassini probe. We find that in our initial scenario as well as in alternative ones, clathrates form and efficiently deplete methane in the ocean, below plume levels. An additional source of methane in the ocean or ulterior dissociation of the clathrates are required to explain the abundances of methane detected in the plumes..

1. Introduction

Enceladus is geologically active, with plumes of water vapor and dust emanating from its south polar terrain [1]. An internal liquid ocean is the most prominent explanation as the source of Enceladus' plumes [2]. Here we used a subglacial lake model [3] in order to investigate the time evolution of species dissolved in Enceladus' hypothesized ocean. This allowed us to compare the results of the different processes at work in our model with the composition of the plumes as measured by the Cassini INMS mass spectrometer [4,5].

2. Model and hypothesis

The model used in this work has been first elaborated to mimic the evolution of Lake Vostok's composition in Antarctica [3], namely the largest subglacial lake known on Earth. In our system, water and the different gases are delivered to the internal ocean when melting occurs due to the slow downward motion of the overlying gas-rich ice layers, and gas-free water leaves the lake as ice accretes to the bottom of the ice sheet in regions where ice moves outward [3,6]. Once the solubility limit has been reached for the species dominant in the ocean, bubbles could form but fugacity and temperature conditions in the liquid layer allow instead clathrate formation. We then computed the composition of clathrates forming at these conditions and investigated how it would affect the proportions of species dissolved in the water of the ocean. To determine the equilibrium conditions of clathrates potentially forming in the deep ocean, we computed the gas fugacities via the resolution of the Redlich-Kwong equation of state [7]. We used a statistical thermodynamic model based on the description of the guest-clathrate interaction by a spherically averaged Kihara potential with a nominal set of potential parameters [3,8,9]. In our computations, we used an ocean composition derived from the values measured in the plumes by Cassini INMS, i.e., the starting hypothesis is that those plumes are representative of the composition of the ocean. We investigated the behavior of five detected species prone to clathration: CO_2, CO, CH_4, N_2 and H_2S. Noble gas (Ar, Kr, Xe) were also considered in order to make predictions to be compared with future measurements. Our calculations take place at a depth of 30km (~3MPa on Enceladus) and at a temperature of 0°C. Those conditions are representative of the range of values generally admitted [4,5,10].

3. Results

We found that the "steady state" composition ultimately reached by the ocean (Fig. 1) cannot match the one of the plumes, as CH_4 is very efficiently trapped into the clathrate phase and its proportion among dissolved species always falls

below plume levels. Tests of other mixtures with more CH_4 in the starting liquid composition did not solve this question as the efficiency of the trapping always brings CH_4 levels below the expected value. Kr and Xe were also found to be noticeably depleted (by one order of magnitude). A calculation of the density of clathrates hosting the volatiles seen in the plumes show those clathrates should have lower density than the environning salt water, they therefore should ascend to the top of the ocean.

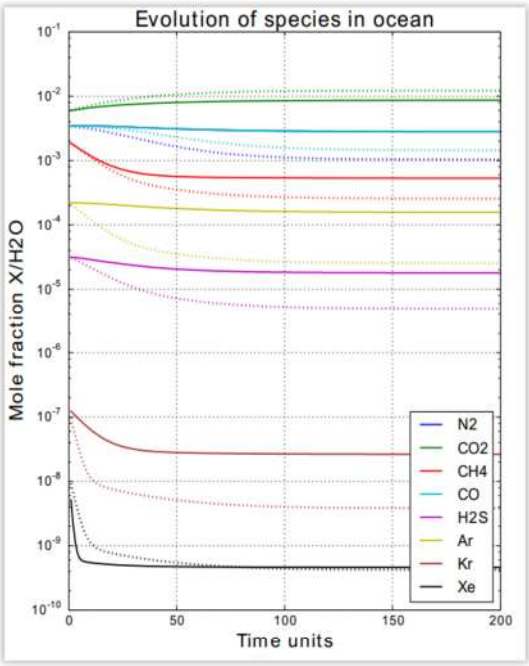

Figure 1: Evolution of the mole fraction of considered species by time units of the model.The full lines represent a scenario of structure I clathrate formation, the dotted lines represent a scenario of structure II formation. The initial values are the mole fractions deduced from the plumes (or from planetesimal formation models in the case of noble gases)

6. Summary and Conclusions

We find that due to clathrate formation, methane in Enceladus' ocean should be depleted below plume levels. This suggests a constant addition of methane in the ocean or ulterior dissociation of clathrates. The source explanation is supported by evidence of hydrothermal activity in the plumes [11], pointing to serpentinization as a possible provider of methane. Future investigations will focus on the transport of clathrates in the ocean after their formation in order to determine to what extent they are involved in the process of plumes formation. It should also be noted that the conditions for capture of volatiles in clathrates are likely to be met in most of the subglacial oceans of the solar system (Jovian moons, Ceres).

In: Bouquet et al., Possible evidence for a methane source in Enceladus' ocean , Geophysical Research Letters, Volume 42, Issue 5, pp. 1334-1339

Acknowledgements

O. Mousis is supported by CNES.
Support by the Cassini Project through JPL subcontract no. 1405853 is acknowledged.
Support by the Rosina Project through JPL subcontract no. 1296001 is acknowledged.

References

[1]Spencer J. R. et al. (2006) *Science*, *311*, 1401-1405.
[2]Potsberg F. et al. (2009 *Nature*, *459*, 1098-1101.
[3]Mousis O. et al. (2013) *Astrobiology, 13(4),* 380-390.
[4]Waite J. H. et al. (2009) *Nature, 460,* 487-490.
[5] Kempf S. et al. (2014) *Space Science Reviews*, submitted.
[6]McKay C. P. et al. (2003) *Geophysical Research Letters*, *30*, 10.1029/2003GL017490.
[7]Redlich O., and Kwong J.N.S. (1949) *Chemical Reviews*, *44*, 233-244.
[8]Mousis O. et al. (2010) *Faraday Discussions*, *147*, 509-525.
[9]Mousis O. et al. (2012) *The Astrophysical Journal*, *757:146*, 7 pp.
[10]Matson D. et al. (2012), Enceladus: a hypothesis to bring both heat and chemicals to the surface, *Icarus 221,* 53-62.
[11]Hsu,H.-W. *et al.,* Ongoing hydrothermal activities within Enceladus. *Nature* **519**, 207–210 (2015)

EPSC Abstracts
Vol. 10, EPSC2015-351, 2015
European Planetary Science Congress 2015

High resolution LBT imaging of Io and Jupiter

A. Conrad (1), K. de Kleer (2), J. Leisenring (3), A. La Camera (4), C. Arcidiacono (5), M. Bertero (4), P. Boccacci (4), D. Defrère (3), I. de Pater (2), P. Hinz (3), K.-H. Hofmann (6), M. Kürster (7), J. Rathbun (8), D. Schertl (6), A. Skemer (3), M. Skrutskie (9), J. Spencer (10), C. Veillet (1), G. Weigelt (6), and C. E. Woodward (11)
(1) LBTO, University of Arizona, Tucson Arizona, USA (aconrad@lbto.org / Fax: 1-520-626-9333), (2) University of Califronia at Berkeley, California, USA, (3) University of Arizona, Arizona, USA, (4) University of Genoa, Genoa, Italy, (5) Observatory of Bologna, Bologna, Italy, (6) Max Planck Institute for Radio Astronomy, Bonn, Germnay, (7) Max Planck Institute for Astronomy, Heidelberg, Germany, (8) Planetary Science Institute, Arizona, USA, (9) University of Virginia, Virginia,USA, (10) Southwest Research Institute, Colorado, USA, (11) Minnesota Institute for Astrophysics, Minnesota,USA

Abstract

We report here results from observing Io at high angular resolution, ~32 mas at 4.8 μm, with LBT at two favorable oppositions as described in our report given at the 2011 EPSC [1]. Analysis of datasets acquired during the last two oppositions has yielded spatially resolved M-band emission at Loki Patera [2], L-band fringes at an eruption site, an occultation of Loki and Pele by Europa, and sufficient sub-earth longitude (SEL) and parallactic angle coverage to produce a full disk map. We summarize completed results for the first of these, and give brief progress reports for the latter three. Finally, we provide plans for imaging the full disk of Jupiter using the MCAO system which is in its commissioning phase at LBT.

1. Loki Patera

Using the Large Binocular Telescope Interferometer (LBTI) [3] mid-infrared camera, LMIRcam, we imaged Io on the night of 24 Dec 2013 UT and detected strong M-band (4.8 μm) thermal emission arising from Loki Patera [1]. In this Fizeau imaging mode, the 22.8 m baseline of the Large Binocular Telescope (LBT) provides angular resolution of ~32 mas (~100 km at Io). In Fig. 1 we show the two distinct emission features detected in this observation, overlaid on a Voyager image of the lava lake on which they are located. These observations also revealed 15 other emission sites, including two previously unidentified hot spots [1].

2. L-band fringes on eruption site

The majority of the LBTI data have been taken at M-band; however, an extremely bright eruption occurred during our 5 Feb 2015 UT observing run which was visible on the limb. The brightness enabled us to obtain L-band fringes (Fig. 2) in Fizeau imaging mode using the 22.8 m baseline.

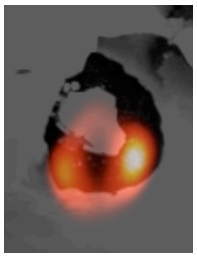

Figure 1: Location of the two hotspots detected within Loki patera. The grey portion of the figure is a Voyager image. We resolve approximately 3 resolutions elements across the lake. The overlaid image of our 4.8 μm LBTI data (in orange) has been smoothed to better indicate the location of the two distinct emission features.

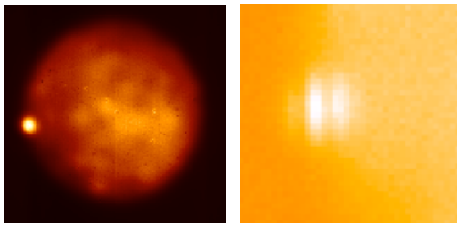

Figure 2: L-band images of an eruption taken with LBTI on 5 Feb 2015.

3. Io/Europa Occultation

On 8 Mar 2015 UT, we observed an occultation of the two Io volcanoes Loki and Pele (see Fig. 3) by Europa. The knife-edge effect of the occultation could provide additional data for measuring features

at high angular resolution. Note for example in Fig. 3 that as occulting Europa approaches Loki, that volcano is still resolved (whereas Pele is unresolved). However as Loki becomes clipped by Europa, we briefly see only a portion of Loki and its image is therefore unresolved.

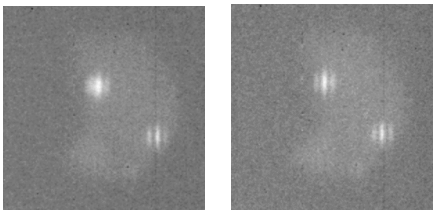

Figure 3: Two raw frames at 4.8 μm of Io's 8 Mar 2015 UT occultation by Europa. Pele (unresolved in both frames) is in the lower right and Loki (resolved in the left hand frame) is in the upper left. Europa appears dark because the water ice on its surface absorbs the incident sunlight at this wavelength.

4. Complete Surface

Production of a complete map of Io at the LBT 22.8 meter resolution requires coverage in both parallactic angle and sub-earth longitude (SEL). Data obtained during the last two Io oppositions provides sufficient coverage for producing a full disk map (Fig. 4).

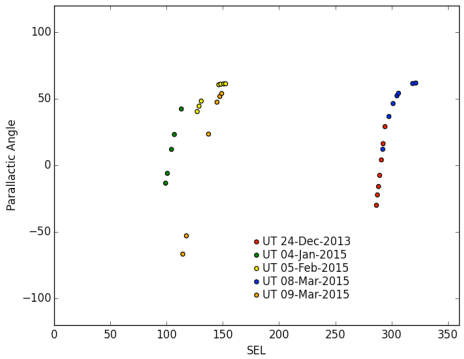

Figure 4. SEL versus parallactic angle coverage of data collected during last two oppositions.

5. Jupiter Full Disk

Solar system objects, since the late 1990's, have been well-studied from ground-based telescopes with adaptive optics (AO). However, a few objects have eluded this technology due to their wide angular extent. Most notably, Venus, Mars at most viewing opportunities, and Jupiter, because their size exceeds the 2-4 arc-second limit for self-reference imposed by most AO systems, are rarely viewed at high angular resolution from the ground. At 40 arc-seconds, Jupiter cannot be used for self-reference and the anisoplanatic effect of single conjugate AO (SCAO) systems limits field of view [4]. Jupiter is therefore a perfect target for exploiting the capabilities of emerging multi-conjugate AO (MCAO) systems. With 12 pyramid wave front sensors (PMWFS) patrolling an annulus with 6-arcminute diameter in its ground-layer AO (GLAO) subsystem, and 8 PMWFS patrolling a circular 2 arc-minute field in its high layer AO subsystem, LINC-NIRVANA (L-N) [5] will be capable of providing homogenous AO correction at 1.1-2.2 μm across the full disk of Jupiter for the first time since observations taken with the MCAO demonstrator (MAD) system in 2008 [6]. At the meeting, we will provide simulations that quantify the correction expected with L-N, in both single-mirror (8.4 meter) MCAO mode, planned for 2017, and in Fizeau (22.8 meter) mode, under consideration as a possible upgrade.

References

[1] Conrad, A., de Pater, I., Kürster, M., Herbst, T., Kaltenegger, L., Skrutskie, M., Hinz, P.: Observing Io at high resolution from the ground with LBT, EPSC-DPS Joint Meeting, 2011

[2] Conrad, A., de Kleer, K., Leisenring, J., et al: Spatially Resolved M-band Emission from Io's Loki Patera – Fizeau Imaging at the 22.8 meter LBT, AJ, DOI:10.1088/0004-6256/149/5/175, 2015.

[3] - Hinz, Phil; Arbo, P.; Bailey, V.; et al: First AO-corrected interferometry with LBTI: steps towards routine coherent imaging observations, SPIE 8445**,** 2012

[4] de Pater, I., Wong, M.H., de Kleer, K. et al: Keck adaptive optics images of Jupiter's north polar cap and Northern Red Oval, Icarus, 213, 2011

[5] Herbst, T. M., Ragazzoni, R., Eckart, A., and Weigelt, G.: Imaging beyond the fringe: an update on the LINC-NIRVANA Fizeau interferometer for the LBT, SPIE 7734, 2010

[6] Wong, M. H., Marchis, F., Marchetti, E., et al: A shift in Jupiter's equatorial haze distribution imaged with the Multi-Conjugate Adaptive Optics Demonstrator at the VLT, AAS/DPS, 2008

EPSC Abstracts
Vol. 10, EPSC2015-374, 2015
European Planetary Science Congress 2015

Stratospheric temperature and composition of Jupiter's polar aurora from IRTF-TEXES

J. A. Sinclair (1), G. S. Orton (1), T. K. Greathouse (2), L. N. Fletcher (3) and P. G. J. Irwin (3)
(1) Jet Propulsion Laboratory, California, United States (james.sinclair@jpl.nasa.gov), (2) Southwest Research Institute, Texas, United States, (3) University of Oxford, United Kingdom

Abstract

We perform an analysis of TEXES (Texas Echelon Cross Echelle Spectrograph, 5- to 25-μm,[1]) spectra of Jupiter's high latitudes observed in December 2014 in order to study the jovian polar aurora. The high resolving power (R $\sim$ 85000) of TEXES allows a large altitude range (10 mbar to 0.01 mbar) in Jupiter's stratosphere to be sounded. Retrievals of temperature and stratospheric composition of these measurements therefore: 1) allow the vertical deposition of auroral energy to be determined and 2) quantify how the auroral processes modify the thermal structure and composition of the jovian stratosphere

1. Introduction

The neutral atmosphere of Jupiter's poles is highly coupled with the external magnetospheric environment. Energetic particles of the solar wind are deflected along Jupiter's magnetic field lines and penetrate the jovian atmosphere at high latitudes. The atmosphere serves as a form of resistance to the charged particles generating the Joule heating responsible for producing the auroral-related *hot spots* observed in the thermal infrared. Figure 1 shows brightness temperature maps of H_2 S1, C_2H_2 (acetylene), C_2H_6 (ethane), C_2H_4 (ethylene) and CH_4 (methane) emission of Jupiter's high-latitudes from IRTF-TEXES scans obtained in December 2014. The enhanced CH_4 emission at high-northern latitudes (north of 50°N and longitudes 120°W - 220°W) and at high-southern latitudes (south of 70°S and longitudes 20°W to 90°W) marks the positions of the auroral-related hot spots that have been observed previously (e.g. [2,3,4,5,6]) and indicates the enhancement of stratospheric temperatures in this region. The enhanced emission of C_2H_2, C_2H_4 and C_2H_6 may also be a result of the warmer stratospheric temperatures in the pressure region in which their lines form and/or may indicate an enrichment in concentration of these molecules: a retrieval analysis is required to disentangle these two contributions.

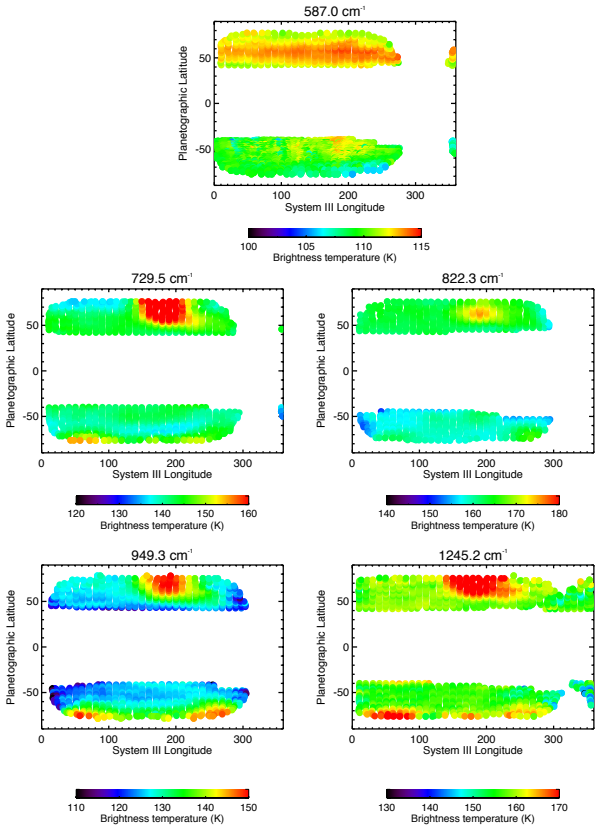

Figure 1: Brightness temperature maps of Jupiter from IRTF-TEXES at 587.0 cm^{-1} (H_2 S1 emission), 729.5 cm^{-1} (C_2H_2 emission), 822.3 cm^{-1} (C_2H_6 emission), 949.3 cm^{-1} (C_2H_4 emission) and 1245.2 cm^{-1} (CH_4 emission).

Similar behaviour as well as enhanced emission of C_3H_4, C_4H_2 and C_6H_6 has been observed in previous studies using Voyager-IRIS (Infrared Interferometer Spectrometer) and Cassini-CIRS (Composite Infrared Spectrometer) spectra (e.g. [3,4,6,7]). However, in these earlier studies, often only qualitative conclusions about temperature and/or concentration contrasts have been made from the spectra alone. In addition, these spacecraft measurements are of limited spectral

resolving power (R < 2500) and thus only sound a single stratospheric level at approximately 5 mbar and thus only capture the effects of the aurora at one altitude. In contrast, ground-based high-resolution (R > 10^4) heterodyne spectra of C_2H_4 features were used to probe the 10-μbar region of Jupiter's aurora [5]. However, without independent temperature information, discrimination between thermal and chemical enhancements inside the aurora was a challenge.

Thus, we aim to quantify the temperature and composition contrasts inside Jupiter's auroral regions by an analysis of IRTF-TEXES spectra acquired in December 2014. The high resolving power of these observations (R = 85000) have sounded a large pressure range in Jupiter's atmosphere (10 mbar to 0.01 mbar), which will allow the effects of the auroral processes on Jupiter's neutral atmosphere to be studied as a function of latitude, longitude and importantly, height. Our method of data acquisition allowed us to obtain independent temperature and composition information at each latitude and longitude, which will allow the degeneracy between temperature and composition in fitting the spectra to be removed.

This work will provide a much needed context for the short-wavelength data that will be returned by the Juno mission upon its arrival at Jupiter in 2016. Juno does not include a thermal infrared instrument that would allow temperature and composition to be determined.

2. Observations & Analysis

TEXES observations at NASA's Infrared Telescope Facility (IRTF) were acquired on December 11th, 2014. At this time, Jupiter's doppler shift exceeded a magnitude of 20 km/s such that telluric and jovian CH_4 lines could easily be distinguished. Initially, in the 587 cm^{-1} spectral setting, the slit (6-12" in length) of the spectrograph was aligned east-west on Jupiter and scanned south, from dark sky off the northern limb of Jupiter, to approximately 50°N (planetographic). Spectra of the dark sky served as a flatfield and as a telluric divisor and a room-temperature blackbody was used as a radiometric standard. These scans were then repeated for the 730 cm^{-1}, 823 cm^{-1}, 950 cm^{-1} and 1248 cm^{-1} settings and subsequently, a similar set of scans were taken for Jupiter's southern hemisphere.

This process was repeated such that Jupiter's rotation allowed longitudinal coverage to be extended and such that observations of a common latitude, longitude and emission angle range could be averaged together to increase the signal-to-noise ratio. Figure 2 shows example spectra at 64°N in all 5 spectral settings, which include the molecular features indicated in the Figure. The enhanced emission inside the auroral hot spot is prominent, in particular for CH_4, C_2H_2 and C_2H_4.

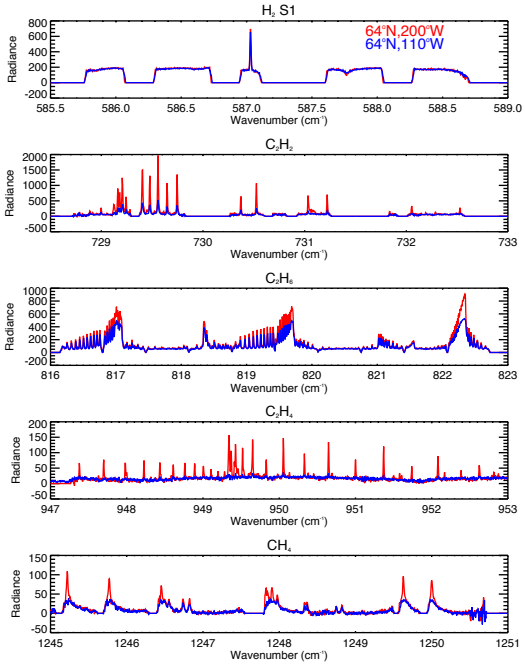

Figure 2: Reduced and calibrated IRTF-TEXES spectra of H_2 S1, C_2H_2, C_2H_6, C_2H_4 and CH_4 emission at 64°N (planetographic), 200°W (red: on the aurora) and 110°W (blue: quiescent). Radiances are in units of nW cm^{-2} sr^{-1} (cm^{-1})$^{-1}$. Regions of zero radiance correspond to breaks in the spectrum between the orders of the diffraction grating.

Retrievals of temperature and composition from these spectra will be conducted using Nemesis [8], a forward model and retrieval radiative-transfer tool. The vertical temperature profile is retrieved using the H_2 S(1) and CH_4 spectra while the C_2H_2, C_2H_6 and C_2H_4 spectra will be used to retrieve their respective concentrations.

References

[1] Lacy et al., 2002, *PASP* 114(792), 153-168
[2] Caldwell et al., 1980, *Icarus* 44, 667-675
[3] Kim et al., 1985, *Icarus* 64, 233-248
[4] Drossart et al., 1993, *JGR* 98, E10, 18803-18811
[5] Kostiuk et al., 1993, *JGR* 98, E10, 18823-18830
[6] Flasar et al., 2002, *Nature* 427, 132-135
[7] Kunde et al., 2004, *Science* 305, 1582-1586
[8] Irwin et al., 2008, *JQSRT* 109, 1136-1150

EPSC Abstracts
Vol. 10, EPSC2015-377, 2015
European Planetary Science Congress 2015

Trapping of noble gases in Titan's atmosphere: A computational study

O. Ozgurel(1), F. Pauzat(1), Y. Ellinger(1) and M.C. Bacchus-Montabonel(2)
(1)Laboratoire de Chimie Théorique, Sorbonne Universités, UPMC Univ. Paris 06, CNRS-UMR 7616, 4, Place Jussieu, 75252 Paris CEDEX 05, France (e-mail: ozgurel@lct.jussieu.fr/Fax +33-1-44274117)
(2)Institut Lumière Matière CNRS UMR 5306, Université Lyon 1, 69622 Villeurbanne CEDEX, France

Abstract

An unexpected noble gases deficiency has been observed in Titan's atmosphere and is still not completely explained. We consider the chemical trapping of these noble gases by ions and neutral molecules present in the upper atmosphere of Titan by means of quantum chemical computational methods.

1. Introduction

The unexpected characteristic of the atmosphere of Titan is that no noble gases other than argon were detected by the Gas Chromatograph Mass Spectrometer (GCMS) aboard the Huygens probe during its descent to the surface of Titan in January 2005. Moreover, most of the detected argon consists of ^{40}Ar which is a decay product of ^{40}K [1]. The significant observed deficiency of noble gases is surprising because this satellite was expected to be made from the same building blocks in the feeding zone of Saturn [2] and share a similar composition with the noble gas-rich planetesimals from which Jupiter was formed [3].

There have been various studies to investigate the possible reasons for this noble gas deficiency, which may be divided into two main themes: the external type related to the formation conditions of Titan in the primitive nebula [4,5], and the internal type related to the atmospheric structure of Titan.

Here, we approach this problem with an internal type explanation, i.e. the possible trapping of noble gases by the molecules present in the atmosphere of Titan. In a first step, we study the interaction of noble gases with the most abundant positive ions present in the upper atmosphere. A second step deals with the possible insertion of noble gases into the neutral molecules of the atmosphere.

2. Trapping by Positive Ions

From the recent interpretation of the data available from the Cassini Ion Neutral Mass Spectrometer (INMS), it is deduced that the most abundant positive ions in the Titan's atmosphere are $HCNH^+$, N_2^+ and $C_2H_4^+$ [6]. Preliminary investigations have been performed for the structures and stabilities of the noble gas complexes of these ions with increasing levels of theory BH&HLYP and CCSD. The results of these calculations showed that only N_2^+ can be an efficient sequestrating agent for noble gases.

Because N_2^+ is an open shell molecule, more complete investigations with multi configurational method (CASPT2) have been necessary in order to get reliable energy potential curves for the corresponding radiative associations between N_2^+ and each of the three noble gases Ar, Kr, Xe.

The quantum chemical determination of the rate coefficients [7] of these radiative associations are obtained with respect to the temperature.

3. Trapping by Neutral Molecules

This second type of trapping mechanism consists in the insertion of the noble gases into the C-H bond of neutral molecules present in the medium. The direct insertion is not thermodynamically favourable. It has to be a multi step process involving the formation of the radical by the radiative environment, followed by the addition of the noble gases to the radical and finally by the capture of the hydrogen.

The most abundant neutral molecules in the atmosphere are C_2H_6, C_3H_8, HCN, C_2H_2 [8]. Successful preliminary tests for HCN and C_2H_2 have

been obtained with Krypton and Xenon, though not for Argon.

4. Conclusion

From the results obtained in this computational study, it can be said that both ions and neutral free radicals are capable of trapping noble gases in Titan's atmosphere. Although the mechanisms are different, namely, radiative association for ions and multi step additions for neutral species, the absence of activation barriers in most reactions is encouraging in view of forthcoming studies on the trapping of Ar, Kr, and Xe by larger systems on the route to tholins [9].

References

[1] Niemann, H. B., Atreya, S. K., Bauer, S. J., et al., Nature, Vol. 438, 779, 2005.

[2] Mousis, O., Gautier, D., Bockelée-Morvan, D., Icarus, Vol. 156, 162, 2002.

[3] Alibert, Y., Mousis, O., Benz, W., ApJ, Vol. 622, L145, 2005.

[4] Mousis, O., Pauzat, F., Ellinger, Y., Ceccarelli, C., ApJ, Vol. 673, 637, 2008.

[5] Pauzat, F., Ellinger, Y., Mousis, O., Dib, Ali, M., Ozgurel, O., ApJ, Vol. 777, 29, 2013.

[6] Mandt, K.E.,Gell D.A. et al., JGR, Vol. 117, E10006, 2012.

[7] Bacchus-Montabonel, M.C., Talbi, D. and Persico, M., J. Phys. B, Vol. 33, 955, 2000

[8] Coustenis, A.,Jennings, D.E., Icarus, Vol. 207, 461, 2010.

[9] Waite Jr., J.H. et al., Science, Vol. 316, 870, 2007.

EPSC Abstracts
Vol. 10, EPSC2015-399, 2015
European Planetary Science Congress 2015

Photochemistry in Saturn's Ring-Shadowed Atmosphere: Hydrocarbon Modulation & Observations of Dust Content

S.G. Edgington (1), S.K. Atreya (2), E.H. Wilson (3), K.H. Baines (1,4), R.A. West (1), G.L. Bjoraker (5), L.N. Fletcher (6), T. Momary (1)

(1) Jet Propulsion Laboratory/California Institute of Technology, USA (scott.g.edgington@jpl.nasa.gov), (2) University of Michigan, USA, (3) Space Environment Technologies, USA, (4) University of Wisconsin, USA , (5) NASA Goddard Space Flight Center, USA, (6) University of Oxford, UK

Abstract

Cassini has been orbiting Saturn for eleven years. During this epoch, the ring shadow has moved from covering a relatively large portion of the northern hemisphere (Figure 1) to covering a large swath south of the equator and continues to move southward. At Saturn Orbit Insertion on July 1, 2004, the ring plane was inclined by ~24 degrees relative to the Sun-Saturn vector. At this time, the projection of the B-ring onto Saturn reached as far as 40ºN along the central meridian (~52ºN at the terminator). At its maximum extent, the ring shadow can reach as far as 48ºN (~58ºN at the terminator). The net effect is that the intensity of both ultraviolet and visible sunlight penetrating into any particular latitude will vary depending on both Saturn's axis relative to the Sun and the optical thickness of each ring system. In essence, the rings act like venetian blinds.(Figure 2).

Our previous work [1,2] examined the variation of the solar flux as a function of solar inclination, i.e. ~8 year season (Figure 3) at Saturn. Here, we report on the impact of the oscillating ring shadow on the photolysis and production rates of hydrocarbons in Saturn's stratosphere and upper troposphere, including acetylene, ethane, propane, and benzene. Beginning with methane, we investigate the impact on production and loss rates of the long-lived photochemical products leading to haze formation are examined at several latitudes over a Saturn year. Similarly, we assess its impact on phosphine abundance, a disequilibrium species whose presence in the upper troposphere is a tracer of convection processes in the deep atmosphere. Comparison to the corresponding rates for the clear atmosphere and for the case of Jupiter, where the solar insolation is known to be insignificant (~3 degree inclination), will also be presented. We will present our ongoing analysis of Cassini's CIRS, UVIS, and VIMS datasets that provide an estimate of the evolving haze content of the northern hemisphere (Figure 4) and we will begin to assess the implications for dynamical mixing. In particular, we will examine how the now famous hexagonal jet stream acts like a barrier to transport, isolating Saturn's north polar region from outside transport of photochemically-generated molecules and haze..

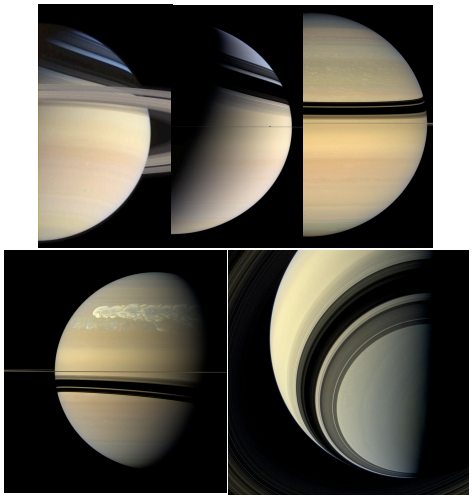

Figure 1. Saturn's atmosphere changes in response to the changing inclination of the ring plane relative to the Sun. (a) Saturn image taken on December 14, 2004. (b) Saturn image taken on March 16, 2006. (c) Saturn image taken on April 23, 2008. (d) Saturn image taken on July 6, 2011. (e) Saturn image taken on July 29, 2013. Images are courtesy of NASA/JPL/Space Science Institute.

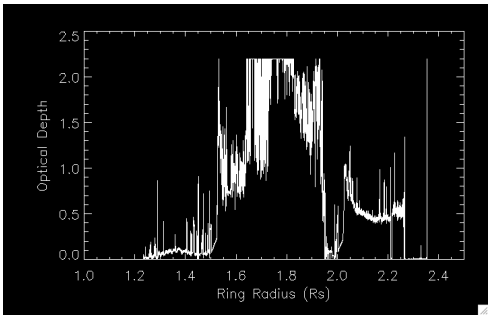

Figure 2. The optical depth of Saturn's rings in the ultraviolet (Josh Colwell, *pers. comm.*) The rings act like a periodic Venetian blind that will shield atmospheric molecules from solar photons.

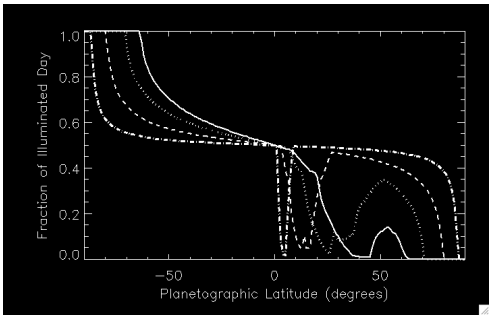

Figure 3. This plot illustrates the fraction of Saturn's day that is illuminated by the Sun as a function of solar declination, i.e. season. The curves correspond to sub-solar points of 26.7ºS (solid), 19.6ºS (dotted), 10.7ºS (dashed), and 3.5ºS (dot-dashed). Ultimately, this will determine the flux of photons allowed to enter the atmosphere relative to those of a clear, un-shaded atmosphere.

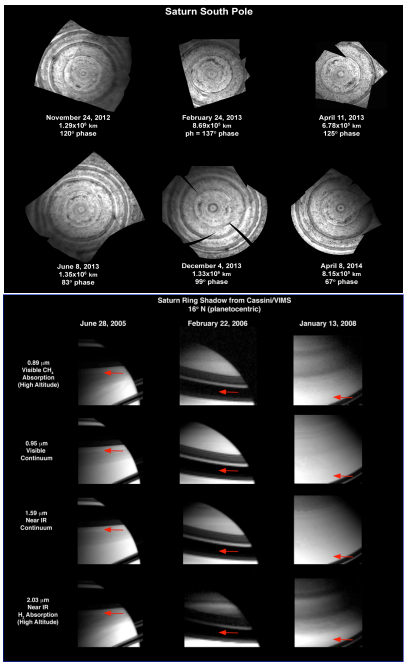

Figure 4. One of the aims of this exercise is to characterize the haze content Saturn's atmosphere. Several Cassini data sets from ISS (above) and VIMS (below) are being used to meet this goal.

Acknowledgements

The research described in this paper was carried out in part at the Jet Propulsion Laboratory, California Institute of Technology, under a contract with the National Aeronautics and Space Administration. Copyright 2015 California Institute of Technology. Government sponsorship is acknowledged..

References

[1] Edgington, S.G., A.A. Simon-Miller, R. Achterberg, G. Bjoraker, P. Romani, F.M. Flasar, J. Colwell, 2006. Adaptation of a 2-D Photochemical Model to Improve Our Understanding of Saturn's Atmosphere. *Bull. American. Astron. Soc.*, **38**, 499 (#11.23).

[2] Edgington, S.G., R.A. West, K.H. Baines, S.K. Atreya, E.H. Wilson, G.L. Bjoraker, L.N. Fletcher, and T. Momary, 2012. Photochemistry in Saturn's Ring Shadowed Atmosphere: Modeling, Observations, and Preliminary Analysis. *Bull. American. Astron. Soc.*, **38**, 499 (#11.23).

EPSC Abstracts
Vol. 10, EPSC2015-440, 2015
European Planetary Science Congress 2015

Europa's neutral and plasma plumes: Detectability during JUICE flybys

H. Huybrighs(1, 2), Y. Futaana(1), S. Barabash(1), M. Wieser(1), P. Wurz (3), A. and L. L. A. Vermeersen (2)
(1) Swedish Institute of Space Physics, Kiruna, Sweden; (2) Delft University of Technology, Delft, The Netherland; (3) University of Bern, Bern, Switzerland. (futaana@irf.se / Fax: +46-980-79025)

Abstract

We investigate the spatial distribution of the neutral and plasma particles by tracking their trajectories originating from the Europa plume. By assuming source characteristics of the water plume recently reported observation of Hubble Space Telescope [1], we first trace the produced neutral particles under the Europa's gravity field, and obtain the density distribution. These neutrals are then ionized using a time constant for the electron impact reactions, and the trajectories of the produced water molecule ions are traced under the Jovian corotational electromagnetic field. From the obtained neutral density and the plasma velocity distributions, we emulate the observations for two flybys of Europa, planned for the JUICE mission. The derived quantities are well above the detection limits of the developing sensors, PEP (Particle Environment Package) to be carried to Europa by the JUICE spacecraft, even if we assume a rather low-mass-flux plume.

1. Introduction

Europa is one of the Galilean moons of Jupiter. It is considered to harbor a sub-surface ocean beneath its icy surface (see for example a review by Schubert et al., 2004 [2] and references therein). Recently, observations of Hubble Space Telescope suggested the existence of a water plume at Europa [1]. From the obtained image, they estimated the total mass flux of ~7 tons/s. The observation implies the existence of a dense, localized source of neutral molecules, which can also produce a significant flux of ions. These ions may be a potential source, in addition to the exospheric particles sublimated or sputtered from the surface, of the hypothetical Europa tori [3, 4].

In this study, by using a simple particle tracing method combined with an electron impact ionization process model, we simulate the spatial distribution of the water molecule density and the water ion velocity distribution in the vicinity of Europa (<3 Re, where Re is the Europa's radius). Then, we evaluate whether the plume neutrals and ions can be detected by the NIM (Neutral gas and Ion Mass Spectrometer) and JDC (Jovian plasma Dynamics and Composition analyser) sensors, as parts of PEP (Particle Environment Package) instrument, on board the planned European Jupiter mission, JUICE.

2. Model

We adopted the plume characteristics, which are the inputs of our study, from the Hubble observation [1]. A test particle tracing method was selected for simplicity. Note that the mass flux reported by Roth et al. [1] is too high to be represented by the test particle model, in particular near the source region. However, for lower-flux plumes, the test particle approximation could be reasonable.

The neutral molecules only feel the Europa's gravity force. Therefore, all the particles follow the ballistic trajectory. Using $>10^9$ particles, the 3-D density map is produced. The main ionization mechanism in this environment is the electron impact ionization. Using the crosssection of water molecule against the electron impact ionization [5] and background electron density, new test particles representing the produced water ions are again traced under the Jovian corotational electromagnetic fields. The 6-D velocity distribution function for water molecule ions is then obtained.

The planned JUICE flyby trajectories [6] are used to calculate the time series of the neutral density and the plasma velocity distribution function. They are

converted to the NIM and JDC readouts to evaluate the detectability of the plume particles.

3. Results

The simulations show that even a very weak gas release of ~0.7 kg/s (10000 times less than what was reported in [1]) can produce sufficiently high signal to noise ratio (>100, if the closest approach is right above the plume) to be measured by the NIM sensor. Here the noise is mainly due to penetrating radiation. Obviously, the NIM sensor is capable of measuring the higher-flux plume. For plumes of lower mass flux plume, although the NIM is instrumentally capable to measure the density, the exospheric population becomes dominant.

The simulated ion velocity distribution function was also assessed against the JDC performance. The very low-flux plume (~0.7 kg/s right below the closest approach) will produce S/N~10. The flux is significantly asymmetric between the inbound and outbound trajectory, because the charged particles are flowing downtail-ward (the leading hemisphere direction) due to the Jovian co-rotation flow.

Acknowledgements

HH was partly supported by the Erasmus+ programme under the European Commission.

References

[1] Roth, L., J. Saur, K. D. Retherford, D. F. Strobel, P. D. Feldman, M. A. McGrath, and F. Nimmo, Transient water vapor at europa's south pole, *Science, 343(6167)*, 171–174, doi:10.1126/science.1247051, 2014.

[2] Schubert, G., J. D. Anderson, T. Spohn, W. B. McKinnon, Interior Composition, Structure, and Dynamics of the Galilean Satellites, in *Jupiter, the Planet, Satellites and Magnetosphere, eds. F. Bagenal, T. Dowling, W. McKinnon, Cambridge University Press,* pp 281–306, 2004.

[3] Lagg, A., N. Krupp, J. Woch, and D. J. Williams, In-situ observations of a neutral gas torus at Europa, *Geophys. Res. Lett., 30,* 1556, doi:10.1029/2003GL017214, 2003.

[4] Mauk, B. H., D. G. Mitchell, R. W. McEntire, C. P. Paranicas, E. C. Roelof, D. J. Williams, S. M. Krim- igis, and A. Lagg, Energetic ion characteristics and neutral gas interactions in Jupiter's magnetosphere, *J. Geophys. Res.,* doi:10.1029/2003JA010270, 2004.

[5] Itikawa, Y., and N. Mason, Cross sections for electron collisions with water molecules, *J. Phys. Chem. Ref. Data, 34(1),* 1–22, doi:10.1063/1.1799251, 2005.

[6] Grasset, O., M. K. Dougherty, A. Coustenis, E. J. Bunce, C. Erd, D. Titov, M. Blanc, A. Coates, P. Drossart, L. N. Fletcher, H. Hussmann, R. Jaumann, N. Krupp, J. P. Lebreton, O. Prieto-Ballesteros, P. Tortora, F. Tosi, and T. Van Hoolst, JUpiter ICy moons Explorer (JUICE): An ESA mission to orbit Ganymede and to characterise the Jupiter system, *Planet. Space Sci., 78*, 1–21, doi: 10.1016/j.pss.2012.12.002, 2013.

EPSC Abstracts
Vol. 10, EPSC2015-478, 2015
European Planetary Science Congress 2015

Simulating the density of $HC^{15}N$ in the Titan atmosphere with a coupled ion-neutral photochemical model

V. Vuitton (1), R. V. Yelle (2), S. J. Klippenstein (3), P. Lavvas (4) and S. M. Hörst (5)
(1) Institut de Planétologie et d'Astrophysique de Grenoble, Univ. Grenoble Alpes, CNRS, Grenoble, F-38000, France, (2) Lunar and Planetary Laboratory, Univ. of Arizona, Tucson, AZ 85721, USA, (3) Chemical Sciences and Engineering Division, Argonne National Lab., Argonne, IL 60439, USA, (4) Groupe de Spectrométrie Moléculaire et Atmosphérique, Univ. Reims Champagne-Ardenne, CNRS, Reims, F-51687, France, (5) Department of Earth and Planetary Sciences, Johns Hopkins Univ., Baltimore, MD 21218, USA (veronique.vuitton@obs.ujf-grenoble.fr)

Abstract

The $^{14}N/^{15}N$ ratio for HCN in the atmosphere of Titan has been measured to be 2 to 3 times as less as the corresponding ratio for N_2. Using a coupled ion-neutral photochemical model incorporating state-of-the-art chemistry and cross-sections for N_2, we show that the difference in the ratio of $^{14}N/^{15}N$ between HCN and N_2 can be explained exclusively by the photo-induced isotopic fractionation of $^{14}N^{14}N$ and $^{14}N^{15}N$, *without any further putative nitrogen input*.

1 Introduction

The $^{14}N/^{15}N$ ratio has now been retrieved in N_2 as well as in HCN. A summary of the available observations is given in Table 1. The HCN-derived values are a factor of 2-3 larger than the N_2-derived values, showing enrichment of the heavier isotope of nitrogen in HCN.

Photo-induced isotopic fractionation has been proposed to explain this ^{15}N enrichment [8]. When incorporating in a photochemical model high-resolution photoabsorption cross sections for $^{14}N^{14}N$ and $^{14}N^{15}N$, isotope-selective shielding allows more dissociative photons for $^{14}N^{15}N$ to penetrate deeper into Titan's atmosphere, resulting in higher photolytic efficiency for $^{14}N^{15}N$ than for $^{14}N^{14}N$, therefore, leading to a higher $HC^{15}N$ production rate.

However, previous calculations give a $HC^{14}N/HC^{15}N$ ratio of 23, which is smaller than the observed value by a factor of $\sim$3. An additional source of atomic nitrogen in the upper atmosphere was then invoked to obtain the observed ratio. With a $^{14}N/^{15}N$ = 183 - 260, the N input is constrained to be in the range $(1-2)\times10^9$ cm^{-2} s^{-1}. This value, in agreement with the understanding of N_2 dissociation by Saturnian magnetospheric ion/electron impact at that time, is now believed to be overestimated by about two orders of magnitude [5], which implies that the origin of the $^{14}N/^{15}N$ fractionation needs to be reevaluated.

2 Photochemical model

The 1-dimensional photochemical model of Titan used in this investigation is adapted from several elements described previously. The background atmosphere (including $^{14}N^{14}N$ and $^{14}N^{15}N$), eddy diffusion coefficient and aerosol distribution are based on Cassini observations [18, 6]. The chemical network includes hydrocarbons [16], nitrogen [19] and oxygen [4] bearing species and takes into account both neutral and ion chemistry [15]. Detailed calculations for the energy deposition of photons and photoelectrons are performed, which include high-resolution temperature-dependent cross-sections for the absorption and dissociation of $^{14}N^{14}N$ and $^{14}N^{15}N$ [5].

In order to make the reaction lists, we start from our ^{14}N chemistry and generate analogous reactions in which ^{14}N is replaced by ^{15}N. Because they do not impact N chemistry, we do not include reactions with oxygen species and negative ions. We also leave out reactions where ^{15}N bearing species would react with each other (i.e. $^{15}N + C_2N$ and $N + C_2^{15}N$ are taken into account but not $^{15}N + C_2^{15}N$). The total rate coefficient is taken to be that of the analogous ^{14}N reaction, i.e. we neglect mass-dependent kinetic isotope effects, since replacing a ^{14}N with ^{15}N represents only a 7% increase in mass. Reactions in which both reactants contain nitrogen, or in which a species contains more than one nitrogen atom, creates special problems and some general rules have to be applied, which is the main uncertainty behind this procedure.

Table 1: $^{14}N/^{15}N$ isotopic ratio in N_2 and HCN.

Formula				
N_2 (thermosphere)	193.5 ± 21.5 (a)			
N_2 (troposphere)	188 ± 16 (b)	147.5 ± 7.5 (c)	183 ± 5 (d)	167.7 ± 0.6 (e)
HCN (stratosphere)	65 ± 5 (f)	$72 \pm 9^{*}$; $94 \pm 13^{**}$ (g)	56 ± 8 (h)	76 ± 6 (i)

*Assuming the temperature profile from [7]; **Assuming the temperature profile from [2].
(a) INMS [17]; (b) INMS extrapolated to surface [17]; (c) INMS extrapolated to surface [9]; (d) GCMS [12]; (e) GCMS [13]; (f) IRAM [11]; (g) SMA [3]; (h) CIRS [14]; (i) Herschel [1].

3 Results and conclusions

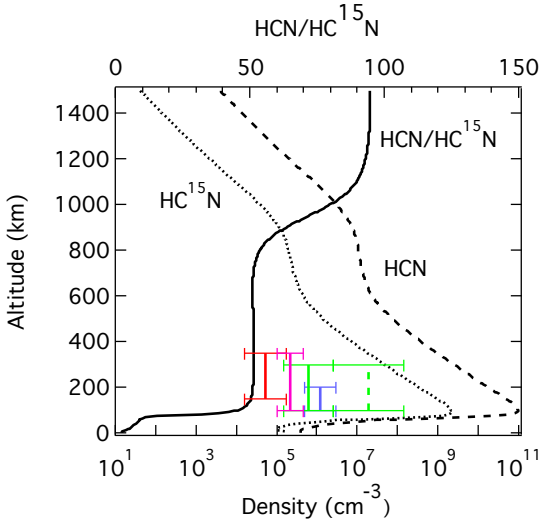

Figure 1: Modeled $HC^{14}N$ and $HC^{15}N$ vertical density profiles (bottom axis) and associated $HC^{14}N/HC^{15}N$ ratio (top axis). The boxes represent the observed $^{14}N/^{15}N$ isotopic ratio in HCN (see Table 1).

Figure 1 shows the simulated $^{14}N/^{15}N$ isotope ratio in HCN, which exhibits a constant value of 51 from 700 to 150 km. This profile is in good agreement with the CIRS value of 56 ± 8, which shows no evidence for vertical variations [14]. However, an average of the four consistent observations (the higher value of Gurwell [3] is at odds with the other values) gives a slightly higher value of $\sim$67. More observations are needed to constrain the vertical profile of $HC^{15}N$ at mid-latitudes as well as potential temporal or latitudinal variations. Observations of the $^{14}N/^{15}N$ in other species, in particular HC_3N, would be of great interest to further constrain the nitrogen chemistry on Titan.

Acknowledgements

VV and PL are grateful to CNES for providing funding in the framework of the Cassini-Huygens participating scientists program.

References

[1] Courtin, R. et al., A&A, 536, #L2, 2011.

[2] Coustenis, A. and Bézard, B., Icarus, 115, 126-140, 1995.

[3] Gurwell, M., ApJ., 616, L7-L10, 2004.

[4] Hörst, S.M. et al., JGR, 113, #E10006, 2008.

[5] Lavvas, P. et al., Icarus, 213, 233-251, 2011.

[6] Lavvas, P. et al., Icarus, 215, 732-750, 2011.

[7] Lellouch, E., Ann. Geophys., 8, 653-660, 1990.

[8] Liang, M.-C. et al., ApJ., 664, L115-L118, 2007.

[9] Mandt, K.E. et al., PSS, 57, 1917-1930, 2009.

[10] Mandt, K.E. et al., JGR, 117, #E10006, 2012.

[11] Marten, A. et al., Icarus, 158, 532-544, 2002.

[12] Niemann, H.B. et al., Nature, 438, 779-784, 2005.

[13] Niemann, H.B. et al., JGR, 115, #E12006, 2010.

[14] Vinatier, S. et al., Icarus, 191, 712-721, 2007.

[15] Vuitton, V. et al., Icarus, 191, 722-742, 2007.

[16] Vuitton, V. et al., ApJ., 744, #11, 2012.

[17] Waite, J.H. et al., Science, 308, 982-986, 2005.

[18] Yelle, R.V. et al., JGR, 113, #E10003, 2008.

[19] Yelle, R.V. et al., Faraday Discuss., 147, 31-49, 2010.

EPSC Abstracts
Vol. 10, EPSC2015-479, 2015
European Planetary Science Congress 2015

Dynamical tides in icy satellites with subsurface oceans

M. Beuthe, A. Rivoldini, A. Trinh, and T. Van Hoolst
Royal Observatory of Belgium, Brussels, Belgium (mbeuthe@oma.be)

1. Abstract

Subsurface oceans are a generic feature of large icy bodies, if not now, then at some point in their past evolution. Various datasets already point to the existence of oceans within Europa, Ganymede, Callisto, Titan, Enceladus, and Mimas, while other bodies like Ceres, Pluto, and Triton await their turn. Subsurface oceans partially decouple the crust and thus greatly enhance tidal effect, unless the crust is very thick and hard. Dynamical effects are usually neglected when computing tidal deformations of solid bodies. It is well known, however, that various oscillation modes have a major impact on tidal dissipation within shallow surface oceans [1]. We show here that the dynamical Love numbers of a non-rotating body exhibit a simple resonant behavior if the ocean is very shallow. We also examine how the resonance is affected by rotation.

2. Methods

As long as there is spherical symmetry, tidal effects can be formulated in terms of four scalars: the tidal potential and three Love numbers depending on the internal structure (density and rheology). Dynamical tides in a non-rotating body can thus be studied with Love numbers which are computed by solving the standard viscoelastic-gravitational equations used in seismic and normal modes analysis. At tidal frequencies, it is a very good approximation to neglect dynamical terms within solid layers while keeping them in the fluid layers. The problem is further simplified by considering an incompressible ocean, in which case either the membrane approach or the propagation matrix method is applicable [2].

Rotation breaks spherical symmetry by introducing Coriolis forces in the viscoelastic-gravitational equations. In that case, all tidal degrees are coupled and the three usual Love numbers do not completely parameterize tidal deformations. We will use numerical codes developed for Earth tides in order to estimate the effect of rotation on the resonance [3].

3. Results

The effect of the crust on dynamical tides is most easily studied with the membrane approach which sums up the rheology of the crust into two effective viscoelastic parameters [2]. The essential physics of the problem are captured by a three-layer model made of an infinitely rigid mantle, an incompressible and homogeneous ocean, and an incompressible crust having the same density as the ocean. In this model, the radial Love number is given by

$$h_2 = \frac{h_2^\circ}{1 + (\Lambda + \Lambda_\omega)\, h_2^\circ}, \qquad (1)$$

where $h_2^\circ = 5/(5-3\xi)$ is the fluid-crust Love number, $\xi = \rho/\rho_b$ being the ocean-to-bulk density ratio. Λ and Λ_ω are the membrane spring constant (complex) and the dynamical correction (real and negative), which are proportional to the effective shear modulus $\bar{\mu}$ and to the squared tidal frequency ω^2, respectively.

Resonance occurs if the ocean thickness is close to

$$D \sim \frac{\omega^2 R^2}{6g} \left(1 - \frac{3}{5}\,\xi + Re(\Lambda)\right)^{-1}, \qquad (2)$$

which is about 160 m for Europa if the crust is thin (so that Λ is negligible). Fig. 1 shows the effect of the res-

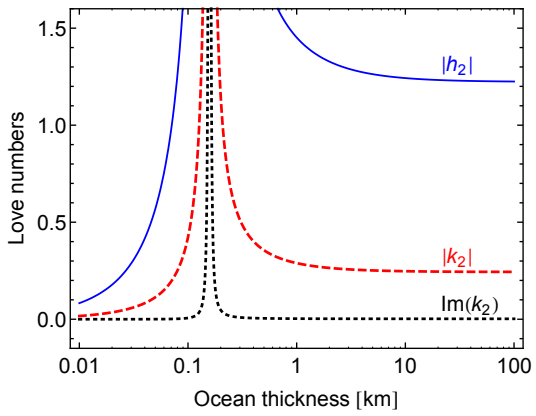

Figure 1: Love numbers of Europa in function of ocean thickness. The crust thickness is small (10 km).

onance on the Love numbers of Europa; $\mathrm{Im}(k_2)$ quantifies tidal dissipation within the crust. The resonance is not only important for very shallow oceans: it significantly decreases the tilt factor $\gamma_2 = 1 + k_2 - h_2$ if the ocean thickness is less than 20 km and may thus lead to underestimating the crust thickness deduced from combined measurements of k_2 and h_2 [4]. If the crust can be neglected ($|\Lambda| \ll 1$), the resonance corresponds to the free oscillation of a surface ocean, or surface gravity mode [5].

For small bodies like Enceladus (assuming a global ocean), the viscoelastic crust has a significant impact, since $|\Lambda| \gg 1$, on the resonant ocean thickness and on the damping of the resonance. We expect that including rotation will displace the resonance and introduce new resonant modes.

Acknowledgements

This work is financially supported by the European Space Agency in collaboration with the Belgian Federal Science Policy Office.

References

[1] Tyler, R. (2008), Nature 456, 770.

[2] Beuthe, M. (2015), arXiv:1504.04574v1.

[3] Wahr, J.M. (1981), GJRAS 64, 677.

[4] Wahr, J.M. et al (2006), JGR 111, E12005.

[5] Lamb, H. (1932), Hydrodynamics, 6th ed.

EPSC Abstracts
Vol. 10, EPSC2015-487, 2015
European Planetary Science Congress 2015

LOSS RATES OF EUROPA'S EXOSPHERE

A. Lucchetti (1,2), C. Plainaki (3), G. Cremonese (2), A. Milillo (3), T. Cassidy (4) , X. Jia (5), V. Shematovich (6)

(1) CISAS, University of Padova, Via Venezia 15, 35131 Padova, Italy (alice.lucchetti@oapd.inaf.it); (2) INAF-Astronomical Observatory of Padova, Vicolo dell'Osservatorio 5, 35131 Padova, Italy; (3) INAF-IAPS Roma, Istituto di Astrofisica e Planetologia Spaziali di Roma, Via del Fosso del Cavaliere, 00133 Roma, Italy; (4) University of Colorado, Laboratory for Atmospheric and Space Physics, 1234 Discovery Drive Boulder, CO 80303, USA; (5) Department of Atmospheric, Oceanic, and Space Sciences, University of Michigan, Ann Arbor, MI, USA; (6) Institute of Astronomy RAS, Moscow, Russia.

Abstract

Reactions in Europa's exosphere are dominated by plasma interactions with neutrals. The cross-sections for these processes are energy dependent and therefore the respective loss rates of the exospheric species depend on the speed distribution of the charged particles relative to the neutrals, as well as the densities of each reactant. In this work we perform a detailed estimation of the H_2O, O_2, and H_2 loss rates due to plasma-neutral interactions with the aim of calculating the total mass loss from the moon. We also investigate the role of the interactions between the planetary ions and the neutral populations in the loss of exospheric species. For completeness, in our estimations we also include photoreactions for both cases of quiet and active Sun.

Introduction

The exosphere of Jupiter's moon Europa includes mainly the following populations: H_2O, released through ion sputtering caused by the energetic ions of Jupiter's magnetosphere that impact the moon's surface ([1], [2], [3], [4]); O_2, and H_2, both species produced through chemical reactions among different products of H_2O radiolytic decomposition ([5], [6], [7], [2], [3], [8]); and some minor species like Na and K ([9], [10], [11], [12]) and H, O, HO_2, and H_2O_2 [13]. The understanding of the evolution of Europa's exosphere and the estimation of its total mass loss has as a mandatory prerequisite the understanding of the interactions between Jupiter's magnetospheric plasma and the satellite's neutral environment.

1. Loss processes

The interactions between the Jupiter's magnetospheric plasma (and the UV radiation) with Europa's neutral environment lead in general to ionization and/or dissociation of the exosphere constituents. As a result, a population of fresh ions can be produced and supply the plasma, contributing, in this way, to the further ionization of the neutral environment; moreover, the freshly dissociated molecules modify the composition of the exosphere creating inhomogeneities in the nominal neutral distribution around the moon.

1.1 Electron impact reactions

The thermal (20 eV) electron density at Europa's orbit varies significantly with magnetic latitude having a value of 38 cm^{-3} near a magnetic latitude of 10° as measured by the Voyager spacecraft [14] and a much larger value of 120 cm^{-3} as modeled for this Voyager epoch data in the centrifugal equatorial plane by [15]. The suprathermal electron density at Europa's orbit is 2 cm^{-3}. The dissociation and ionization rates for electrons impact processes are computed by [16]:

$$\nu = k(T_e)n_e$$

where n_e is the electron density and κ is the rate coefficient in cm^{-3} s^{-1} as a function of electron temperature T_e. The rate coefficient is determined by $\kappa = \int f(v)\sigma(v)dv$, where f(v) is the Maxwellian distribution of the measure electron temperature, and σ the experimentally cross section.

Electron impact reaction	Rate ($10^{-6}s^{-1}$)	Note
$H_2O + e \rightarrow OH + H + e$	1.17 - 3	[1,2]
$H_2O + e \rightarrow H_2O^+ + 2e$	0.68 - 1.71	[2]
$H_2O + e \rightarrow OH^+ + H + 2e$	0.087 - 0.123	[2]
$H_2O + e \rightarrow OH + H^+ + 2e$	0.07 - 0.08	[2]
$H_2O + e \rightarrow H_2 + O^+2e$	0.013 - 0.014	[3]
$O_2 + e \rightarrow O + O + e$	0.68 - 2	[4]
$O_2 + e \rightarrow O_2^+ + 2e$	0.57 - 1.2	[5]
$O_2 + e \rightarrow O^+ + O + 2e$	0.2 - 0.25	[5]
$H_2 + e \rightarrow H + H + e$	0.01 - 0.03	[6]
$H_2 + e \rightarrow H_2^+ + e$	0.44 - 1.1	[5]
$H_2 + e \rightarrow H^+ + H + 2e$	0.016 - 0.028	[5]

[1]Harb et al. (2001);[2]Itikawa & Mason (2005);
[3]Shirai et al. (2001);[4]Cosby (1993);
[5]Straub et al. (1996);[6]De La Haye (2005).

Table 1 *Electron impact rates. The range of electron impact rates are for the assumed plasma properties: low (high) core electron density = 38 cm^{-3} (120 cm^{-3}), core electron temperature = 20 eV, suprathermal electron density = 2 cm^{-3} , suprathermal electron temperature = 250 eV.*

1.2 Photoreactions

Photoreaction rates are given at 1 AU by [17]. These rates are inversely proportional to the square distance to the Sun. In Table 2 are reported the rates for quiet and active Sun at Europa's orbit (5.2 AU) for the H_2O, O_2, and H_2 Photo-Reactions.

Photo-Reaction	$\nu(10^{-6}s^{-1})$
$H_2O + h\nu \rightarrow H + OH$	$0.38 - 0.65$
$H_2O + h\nu \rightarrow H_2 + O(^1D)$	$0.022 - 0.055$
$H_2O + h\nu \rightarrow H + H + O$	$0.028 - 0.71$
$H_2O + h\nu \rightarrow H_2O^+ + e$	$0.012 - 0.031$
$H_2O + h\nu \rightarrow OH^+ + H + e$	$0.0021 - 0.0056$
$H_2O + h\nu \rightarrow OH + H^+ + e$	$0.00048 - 0.0015$
$H_2O + h\nu \rightarrow H_2 + O^+ + e$	$0.00022 - 0.00082$
$O_2 + h\nu \rightarrow O(^3P) + O(^3P)$	$0.0052 - 0.0082$
$O_2 + h\nu \rightarrow O(^3P) + O(^1D)$	$0.15 - 0.24$
$O_2 + h\nu \rightarrow O(^1S) + O(^1S)$	$0.0015 - 0.0035$
$O_2 + h\nu \rightarrow O_2^+ + e$	$0.017 - 0.044$
$O_2 + h\nu \rightarrow O + O^+ + e$	$0.004 - 0.013$
$H_2 + h\nu \rightarrow H(^1S) + H(^1S)$	$0.0018 - 0.004$
$H_2 + h\nu \rightarrow H(^1S) + H(2s, 2p)$	$0.0013 - 0.003$
$H_2 + h\nu \rightarrow H_2^+ + e$	$0.002 - 0.004$
$H_2 + h\nu \rightarrow H + H^+ + e$	$0.00035 - 0.0011$

Table 2. *Photoreactions rates*

1.3 Charge-exchange reactions

Ion-neutral reaction rates and rate coefficients are also determined by the same equations reported for electron impact reactions, but since ions are more massive than electrons, the relative bulk motion between the ions and neutrals is significant. The rate coefficient reduces to

$$\nu = n_i v_{flow} \sigma(v_{flow})$$

where n_i is the ion density, v_{flow} is the bulk flow velocity of the ions relative to the neutral gas. If the plasma is corotating with the magnetic field and neutrals are in the satellite exospheres or bound neutral tori, then the relative velocities are well approximated by the difference between the magnetic field corotational velocity and the Keplerian orbital velocity (about 100 km/s).

In addition, charge-exchange reactions between planetary ions and the neutral populations are considered. For example, dissociative ionization of H_2O and direct ionization of O_2 produced by the impact of magnetospheric electrons is primarily responsible for the formation of O_2^+ ions from the dominant O_2 atmosphere. The O_2^+ source creates a large density of ionospheric ions (10^2 – 10^4 cm^{-3}) with a characteristic flow speed of 20 km/s through the atmosphere [18].

Charge-exchange reaction	Rate $(10^{-6}s^{-1})$	Note
$O_2^+ + O_2 \rightarrow O_2 + O_2^+$	0.2 - 20	[1]

[1]Benyoucef & Yousfi (2014)

Table 3*. Charge-exchange rates between* O_2^+ *and* O_2*. The rate values correspond to a range density of* $10^2 – 10^4$ cm^{-3}

Discussion and Conclusions

Dissociative and direct ionization electron impact reactions rates seems to dominate the relative photodissociation rates by an order of magnitude. On the night side the photoreaction are negligible, but on the day side, depending on the position of Europa and on the plasma sheet, photoreactions can be a strong contribution. Charge-exchange reactions between the heavy-ion corotating plasma (O^+, O^{2+}, S^+, S^{2+}, S^{3+}, S^{4+}) and Europa's neutral environment must be studied in more detail to understand better their contribution. The loss rates calculations are very important for the estimation of the neutral environment of Europa's tenuous atmosphere. The variation of these values defines a local anisotropy of the neutral populations defining a specific morphology of Europa's atmosphere. These loss rates must be taken into account inside exosphere's models to better constrain observation emission measurements (e.g. VIS, UV,IR) and must also be taken into account in the modeling of Europa's plasma interaction with the Jovian magnetosphere.

Acknowledgements

The work in this paper has been performed in the context of the activities of the ISSI International Team #322: "Towards a global unified model of Europa's exosphere in view of the JUICE mission" http://www.issibern.ch/teams/exospherejuice/".

References: [1] Brown, W.L., et al, 1982. *Science*, *218*, 525-531. [2] Plainaki, C., et al., 2010. Icarus *210*, 385 – 395. [3] Plainaki, C., et al., 2012. Icarus *218*, 956 – 966. [4] Cassidy, T., et al., 2013. *PSS*, *77*, 64-73. [5] Johnson, R.E., 1990. *Enegetic charged particle interaction with atmosphere and surfaces.* [6] Shematovich, V., et al., 2005. *Icarus*, *173*, 480-498. [7] Cassidy, T., et al., 2010. *Space Sci. Rev*, *153*, 299-315. [8] Plainaki, C., et al., 2013. *PSS*, *88*, 42-52. [9] Brown & Hill, 1996. *Nature*, *380*, 229-231. [10] Brown, M.E., et al., 2001. *Icarus*, *151*, 190-195. [11] Leblanc, F. et al., 2002, *Icarus*, *159*, 132-144. [12] Leblanc, F., et al., 2005. *Icarus*, *178*, 367-385. [13] Baragiola, R.A., et al., 2003. *PSS*, *51*, 953-961. [14] Sittler & Strobel 1987. *JGR*, *92*, 5741-5762. [15] Bagenal, F. 1994. *JGR*, *99*, 11043-11062. [16] Burger, M.H., 2010. *Space Sci. Rev.*, *153*, 349-374. [17] Huebner et al., 1992. *Ap&SS*, *195*, 1-289. [18] Paranicas et al., 1998. *JGR*, *103*, 15001-15008.

EPSC Abstracts
Vol. 10, EPSC2015-514, 2015
European Planetary Science Congress 2015

Estimation of Ganymede's Topography, Rotation and Tidal Deformation – a Study of Synthetic Ganymede Laser Altimeter Observations

T. Steinke (1,2), A. Stark (1), G. Steinbrügge (1), H. Hussmann (1), J. Oberst (1)
(1) German Aerospace Center (DLR), Institute of Planetary Research, Berlin, Germany, (teresa.steinke@dlr.de),
(2) Karlsruhe Institute of Technology (KIT), Institute of Geophysics, Karlsruhe, Germany

Abstract

We implement an iterative least-squares inversion routine to study the estimation of several dynamic Ganymede rotation parameters by laser altimetry. Based on spherical harmonic expansions of the global topography we use simulated Ganymede Laser Altimeter observations representing the synthetic topography of the satellite. Besides the static topography we determine the dynamical parameters, such as the rotation rate, the amplitudes of physical librations, the spin pole orientation, and the tidal deformation. This parameters may strengthen implications for a liquid ocean beneath Ganymede's icy shell and, in addition, constrain geodetic frame parameters essential for various space-borne experiments.

1. Introduction

A major task for characterizing the habitability of the outer solar system is the exploration of subsurface oceans of icy satellites. Time-variable torques cause the satellite to respond according to their interior. Recent studies suggest that the responses observed at the satellite's surface may reveal structural and rheological characteristics of materials beneath the surface ice. The European Space Agency (ESA) is preparing a mission to the Jovian system with its final destination Ganymede. JUICE (JUpiter ICy moons Explorer) will orbit the satellite by 2033. The on board Ganymede Laser Altimeter (GALA) will provide global and local topographic mapping of Ganymede's surface. Since limited coverage with stereo imaging will be available the simultaneous estimation of the topography, rotation state and response parameters of the surface using laser altimeter data will be of great benefit.

2. Method

First, the JUICE's ground track at longitude λ_i and latitude θ_i of Ganymede's fixed reference system is calculated for each time epoch t_i resulting in a globally distributed laser spot pattern concentrated in the polar regions. The applied rotation model for Ganymede is defined by three time-dependent angles: the right ascension $\alpha(t_i)$ and the declination $\delta(t_i)$ (both describing the position of the bodies north pole towards the celestial reference system) and the prime meridian $\omega(t_i)$. To model the complex time evolution of the Ganymede's resonant rotation state we use a series expansion (derived from the standard IAU [2] formulation) up to second order in t_i centred at the time of arrival of the spacecraft in Ganymede orbit. Additionally, we add k time-variable libration modes

$$\omega_{\text{lib}}(t_i) = \sum_k A_{\text{lib,k}} \sin(f_{\text{lib,k}} t_i + \phi_{\text{lib,k}}), \qquad (1)$$

to the ω angle, where $A_{\text{lib,k}}$, $f_{\text{lib,k}}$ and $\phi_{\text{lib,k}}$ are the libration modes' amplitudes, frequencies and phases. In the second step, GALA observations described by the radial distance $r_{\text{obs,i}}$ from Ganymede's center to its surface at JUICE's ground track are modelled by the equation

$$r_{\text{obs,i}} = \sum_{n=0}^{n_{\max}} \sum_{m=0}^{n} \overline{P_{\text{nm}}}(\theta_i)\{C_{\text{nm}} \cos m\lambda_i + S_{\text{nm}} \sin m\lambda_i\} + h_2 V_{\text{pot}}(\lambda_i, \theta_i, t_i). \qquad (2)$$

Here $\overline{P_{\text{nm}}}$ is the fully normalized associated Legendre function of degree n and order m. Based on the Kaula power law we generate random static topography coefficients C_{nm} and S_{nm} up to degree $n_{\max} = 200$ whereas the dynamic tidal deformation is calculated by the Love number h_2 and a known tidal potential $V_{\text{pot}}(\lambda_i, \theta_i, t_i)$. [1] simulated BepiColombo Laser Altimeter data for Mercury to solve for the spherical harmonic topography coefficients C_{nm} and S_{nm}, the Love

number h_2 and the main libration amplitude A_{lib} for given phase and frequency. Here, in addition, we estimate the total rotation, including the orientation of the main spin axis and the rotation rate up to the considered second order. Since the simultaneous determination of rotation state and topography results in a highly non-linear inversion problem an iterative reduction of the misfit between the synthetic and estimated (obtained by updated starting values) observation vectors $r_{\text{obs,i}} - r_{\text{model,i}}$ is required. Due to polar and equatorial gaps of laser spots and a large degree of correlation we test regularisation of the normal matrix by a priori information and weighting techniques. In addition, the degree of the estimated spherical expansion is optimised to reduce the trade-off between cumulative error degree variances (commission error) and non-modelled remaining topography signal (omission error).

3. Results and Conclusion

We apply the inversion routine to several JUICE mission scenarios and observation errors (including orbit, pointing and instrument errors) and show the resulting measurement accuracy of the estimated parameters C_{nm}, S_{nm}, $A_{\text{lib,k}}$, h_2 and α, δ, ω up to the second order. While the determination of the orientation of the rotation pole, the rotation rate and short libration periods are promising, long periodic variations beyond the Ganymede orbit phase and the expected small quadratic terms of the rotation state may not be detectable.

References

[1] Koch, C., Christensen, U., Kallenbach, R.: Simultaneous determination of global topography, tidal Love number and libration amplitude of Mercury by laser altimetry. Planetary and Space Science, Vol. 56(9), pp. 1226-1237, 2008.

[2] Archinal, B.A., A'Hearn, M.F., Bowell, E., Conrad, A., Consolmagno, G.J., Courtin, R., Fukushima, T., Hestroffer, D., Hilton, J.L., Krasinsky G.A., Neumann, G., Oberst J., Seidelmann, P.K., Stooke, P., Tholen, D.J., Thomas, P.C., Williams, I.P.: Report of the IAU Working Group on cartographic coordinates and rotational elements: 2009. Celestial Mechanics and Dynamical Astronomy, Vol. 109(2), pp. 101-135, 2011.

EPSC Abstracts
Vol. 10, EPSC2015-524, 2015
European Planetary Science Congress 2015

Localized bending and heating at Enceladus' south pole

M. Beuthe
Royal Observatory of Belgium, Brussels, Belgium (mbeuthe@oma.be)

1. Abstract

Since the discovery in 2005 of geysers at the south pole of Enceladus, this midsize moon of Saturn has become famous as the most active icy world in the solar system and as a potential harbor for microbial life. All data gathered during flybys by the Cassini probe point to the existence of a subsurface ocean maintained by tidal heating in the icy crust. This explanation, however, is in conflict with geophysical models which only account for a tenth of the heat output. Such models are based on an approach designed for larger satellites, for which elastic effects are weaker and lateral inhomogeneities are less prominent. By contrast, lateral variations of interior structure are probably the key to understand Enceladus' geological activity. We will test the hypothesis that tidal dissipation is greatly enhanced by local bending of a thinner crust in the south polar region. More generally, we plan to develop a new and faster method to compute tidal dissipation in small bodies with lateral heterogeneities, consisting in modeling the crust as a two-dimensional spherical shell with variable thickness or rigidity and with depth-dependent rheology.

2. Problem

Enceladus' heat budget is an enigma. At the present day, neither internal radioactivity nor chemical reactions provide enough energy but tidal forces (due to the non-circular orbit) can generate high rates of dissipation, as demonstrated by the volcanism on Jupiter's moon Io. In support of this explanation, Enceladus' plume is brighter at the apocenter of the orbit when tidal forces tend to open the tiger cracks [1], although the timing of individual jets appears to be random [2]. In principle, tidal heating can occur at all depths within the satellite but significant ocean dissipation requires a too large obliquity while the core does not dissipate enough even if it is very soft. Tidal heating due to shear friction along fault lines could provide enough heat but it does not cause plume brightening at apocenter and predicts wide warm zones which have not been observed [3].

The most likely source of tidal heating arises from deformations and friction within the whole crust [4]. However, this mechanism has its own problems. In present models, the power output is too small (by up to a factor 10) and the heat transport to the surface is too efficient, resulting in the freezing of the subsurface ocean and the end of the high-dissipation regime [5, 6]. Adding anti-freeze agents such as ammonia to the ocean only slows down the freezing. One possible solution is to postulate that Enceladus is now in a transient regime in which the dissipated energy is the leftover from an orbital state of higher eccentricity and higher dissipation. Episodic heat production would mean that we observe Enceladus at a very special time. The active phase indeed only lasts a few millions years, with a dormancy period of the order of 100 millions years. The difference in time scale between active and dormant phases results from the rapid decrease of the orbital eccentricity when the body dissipates a lot, whereas the eccentricity increases very slowly when dissipation is low. There is thus a low a priori probability that our observations coincide with Enceladus being at the end of its active phase, when the eccentricity has fallen to a low level but the icy shell is still warm. While episodic heating is favored by astronomical constraints imposing a maximum steady-state dissipation rate of 1.1 GW [7], a recent analysis of astrometry data allows a much higher dissipation rate [8], so that this argument is not conclusive. We will thus examine an alternative solution to the problem of 'too little heat/freezing ocean'.

3. Method

Classical computations of tidal dissipation are based on an approach designed for much larger satellites such as Europa, where gravity dominates elastic effects (the crust follows the deformation of the ocean) so that tidal deformations are not much affected by lateral crustal inhomogeneities. In that case, dissipation is mostly due to viscoelastic lateral extension/compression of the crust of harmonic degree two,

with very little contribution from bending or twisting. However, Enceladus is small (252 km radius, a sixth of Europa's size) and its surface gravity is weak (0.1 m/s^2, less than a tenth of Europa's gravity) so that elasticity dominates gravity. Furthermore geologic activity is only present at the south pole, probably above a local underground sea under a thinner and weaker crust. We thus expect that tidal deformations have components of harmonic degrees other than two and that local viscoelastic effects with bending/twisting give a significant contribution to tidal heating. To date, there is only one model that self-consistently computes tidal dissipation in a three-dimensional viscoelastic body [6], but its complexity makes it difficult to examine all physically interesting cases.

We propose a new method - thin shell theory - for the computation of localized tidal dissipation in Enceladus, with the aim of finding the missing contribution to the crustal heat budget. Up to now, thin shell theory has only been used to predict elastic deformations, stresses and tectonics when the crust is uniform in thickness and rigidity. We have recently demonstrated, however, that the theory of thin shells with variable thickness that we developed for lithospheric flexure [9, 10] can be applied to large satellites such as Europa for the computation of tidal dissipation in a non-uniform crust [11]. There are no major technical hurdles to extend this work to a smaller body (Enceladus) where bending is important. Moreover, our recent work has shown that membrane theory (a special case of thin shell theory) can be modified in order to include the dependence on depth of the crustal rheology [12]. We will do the same in our thin shell approach, so that the rheology of Enceladus' crust will vary not only laterally but also radially, thus effectively in three dimensions, although the thin shell method remains intrinsically two-dimensional.

Acknowledgements

This work is financially supported by the Belgian Federal Science Policy Office through the Brain Pioneer contract BR/314/PI/LOTIDE.

References

[1] Hedman M. M. et al. (2013), Nature 500, 182.

[2] Hurford T. A. et al. (2012), Icarus 220, 896.

[3] Nimmo F. et al. (2014), AJ 148, 46.

[4] Hurford T. A. et al. (2007), Nature 447, 292.

[5] Roberts J. and Nimmo F. (2008), Icarus 194, 675.

[6] Behounkova M. et al. (2012), Icarus 219, 655.

[7] Meyer J. and Wisdom J. (2007), Icarus 188, 535.

[8] Lainey V. et al. (2012), AJ 752, 14.

[9] Beuthe M. (2008), GJI 172, 817.

[10] Beuthe, M. (2010), Icarus 209, 795.

[11] Beuthe M. (2013), abstract EPSC2013-725.

[12] Beuthe, M. (2015), Icarus 248, 109.

EPSC Abstracts
Vol. 10, EPSC2015-535, 2015
European Planetary Science Congress 2015

CO concentration in the upper stratosphere and mesosphere of Titan: non-LTE analysis of VIMS dayside limb observations at 4.7 μm

F. Fabiano (1,2), M. López Puertas (4), A. Adriani (3), M.L. Moriconi (3), E. D'Aversa (3), B. Funke (4), M.A. López-Valverde (4), M. Ridolfi (1) and B.M. Dinelli (2)
(1) Department of Physics and Astronomy - University of Bologna, Italy, (2) Institute of Atmospheric Sciences and Climate (ISAC-CNR), Bologna, Italy, (3) Institute for Space Atrophysics and Planetology (IAPS-INAF), Roma, Italy, (4) Instituto de Astrofísica de Andalucía (IAA-CSIC), Granada, Spain

Abstract

During the last 20 years, many works have focused on the atmospheric concentration of CO on Titan, giving contradictory results. In particular, no measurement of the CO abundance above 300 km has been done yet, due to the faint emission of CO above that altitude. On the other hand, such a study is particularly awaited as a confirmation of photochemical models that predict a uniform volume mixing ratio of CO in the whole Titan's atmosphere. Moreover, given that CO is the main reservoir of oxygen in Titan's atmosphere and its presence is linked to water, the matter is of astrobiological interest too.

The analysis of VIMS (Visual & Infrared Mapping Spectrometer, onboard Cassini) daytime limb measurements of Titan at 4.7 μm, corresponding to the vibrational bands of CO, allows such a study: CO molecules are significantly excited by solar radiation and the otherwise faint infrared signal of the upper atmosphere is large, allowing to probe this region too. On the other hand, the strong non-LTE behavior of CO infrared emission above 200 km, strongly coupled to N_2 and CH_4 vibrational levels, represents an extra complexity of the data analysis.

In order to deal with CO non-LTE emission, we have developed a non-LTE excitation/de-excitation model for the first two CO vibrational levels of the two most abundant isotopologues. We consider the contribution of absorption of radiation in the fundamental, first hot and first overtone bands and evaluate the possible contribution of different collisional processes, mainly the coupling with the first excited state of N_2 and with several levels of CH_4. The solution of the non-LTE problem is obtained through GRANADA [1], a non-LTE population algorithm based on *Lambda iteration* resolution strategy, eventually coupled to a Curtis-Matrix type approach. The result shows a significant over-population of the first vibrational level above 300 km and of the second level in the whole atmosphere. The possibility of further pathways for CO(1) (de)-excitation, mainly through vibrational energy transfer from/to the excited states of CH_4, through the route $CH_4(\nu^*) \Leftrightarrow N_2(1) \Leftrightarrow CO(1)$, is explored and seems to be crucial for establishing its population.

We then analyze the spectra acquired by VIMS between 2004 and 2013 in the 4.7 μm region, for daytime conditions. Considering the non-LTE populations obtained above, the retrieval of CO concentration is performed with the aid of Geofit Broad Band, a non-LTE *line-by-line* radiative transfer code coupled to a bayesian inversion method, initially developed for the Earth's atmosphere and later adapted to other planetary atmospheres [2]. The low signal-to-noise ratio and spectral resolution of the instrument considerably complicate the data analysis. Moreover, the scattered solar radiation is not negligible below 350 km and dominates over atmospheric emission below 200 km, and hence it is taken into account as well.

CO relative abundance profiles are finally obtained and discussed in the light of photochemical models predictions.

References

[1] B. Funke *et al.*, *Journal of Quantitative Spectroscopy & Radiative Transfer* **113**, 1771 (2012).

[2] A. Adriani *et al.*, *Icarus* **214**, 584 (2011).

EPSC Abstracts
Vol. 10, EPSC2015-538, 2015
European Planetary Science Congress 2015

Enceladus flybys in the view of energetic particles

N. Krupp (1), E. Roussos (1), A. Kotova (1,5), K.Khurana (2), G.H. Jones (3) and S. Simon (4)
(1) Max Planck Institute for Solar System Research, Göttingen, Germany (krupp@mps.mpg.de / Fax: +49-551-384979240);
(2) IGPP, UCLA, Los Angeles, CA, USA;
(3) MSSL-UCL, Holmbury St. Mary, Dorking, UK
(4) Georgiatech, Atlanta, GA, USA
(5) IRAP, Toulouse, France

Abstract

We report on particle measurements in the vicinity of Enceladus in the Saturnian magnetosphere taken onboard the Cassini Spacecraft between 2005 and 2015. Enceladus, embedded in Saturn's radiation belts has been investigated by Cassini during 23 close flybys including those where the spacecraft went through the south polar plumes of the moon.
This paper is an update of the results from the first 14 flybys published by [2]. We report on the results of energetic electron measurements in the energy range 27 keV to 21 MeV taken by the Low Energy Magnetospheric Measurement System LEMMS, part of the Magnetospheric Imaging Instrument MIMI onboard combined with measurements of the magnetometer instrument MAG and the Electron Spectrometer ELS of the Plasma instrument CAPS onboard the spacecraft.
The analysis showed that Cassini was connected to the plume material along field lines well before entering the high density region of the plume. Sharp absorption signatures as the result of losses of energetic electrons bouncing along those field lines, through the emitted gas and dust clouds, clearly depend on flyby geometry as well as on measured pitch angle/look direction of the instrument and we use those depletion signatures to map out the interaction region.
In addition we use A.I.K.E.F hybrid code simulation results near Enceladus [1] to better understand the "ramp-like" features where only a partial depletion has been observed further away from the moon followed by nearly full absorption of electrons closer in.
During some of the flybys MIMI data are consistent with the presence of dust in energetic electron data when Cassini flew directly through the south polar plume.

References

[1] Kriegel, H., Simon, S., Müller, J., Motschmann, U., Saur, J., Glassmeier, K., Dougherty, M. K.. The plasma interaction of Enceladus: 3D hybrid simulations and comparison with Cassini MAG data. Planet. Space, Sci. 57, 2113-2122, 2009.

[2] Krupp, N., Roussos, E., Kollmann, P., Paranicas, C. Mitchell, D.G., Krimigis, S.M. Rymer, A., Jones, G.H., Arridge, C.S., Armstrong, T.P., Khurana, K.K., The Cassini Enceladus encounters 2005-2010 in the view of energetic electron measurements, Icarus, 2012.

EPSC Abstracts
Vol. 10, EPSC2015-539, 2015
European Planetary Science Congress 2015

Access of energetic particles to Titan's exobase

L. Regoli (1,2,3), E. Roussos (3), M. Feyerabend (4,5), G. H. Jones (1,2), N. Krupp (3), A. J. Coates (1,2), S. Simon (5) and U. Motschmann (6)
(1) Mullard Space Science Laboratory (UCL), Holmbury St. Mary, UK, (2) Centre for Planetary Science at UCL/Birkbeck, London, UK, (3) Max Planck Institute for Solar System Research, Göttingen, Germany, (4) Institute of Geophysics and Meteorology, University of Cologne, Cologne, Germany, (5) Earth and Atmospheric Sciences, Georgia Tech, Atlanta, USA, (6) Institut für Theoretische Physik, Technische Universität Braunschweig, Germany

(regoli@mps.mpg.de)

Abstract

In this contribution we use a particle tracing code to trace energetic particles close to Titan in the specific magnetospheric conditions of the Cassini T9 flyby. The particles simulated are H^+ and O^+ ions with energies ranging from 1 keV to 1 MeV and the background electromagnetic field is represented by the output of the A.I.K.E.F. hybrid code for that specific flyby. These tools are used to generate 2D maps showing the access of the particles to the moon's exobase and those maps are subsequently used to normalize the fluxes measured by the Cassini MIMI/CHEMS instrument and estimate the energy deposition at specific positions around the moon. With this, we are able to estimate the importance that the asymmetries in the access of particles to the exobase has in the dynamics of Titan's ionosphere.

1. Introduction

Titan is the only moon in the Solar System known to host a complex and dense atmosphere. Even though the moon does not possess an internal magnetic field [2], the presence of the ionosphere as a conducting obstacle to the corotating plasma from Saturn's magnetosphere creates an induced magnetosphere around the moon. This whole environment is highly variable since Titan can be located outside the magnetosphere (in the unshocked solar wind), in the magnetosheath or in the outer magnetosphere, where in turn completely different plasma environments can be encountered, depending on whether Titan is located above, below or inside the bowl-shaped current sheet [1].

1.1 The flyby

For the present study, the T9 flyby was selected due to the asymmetric nature of the electromagnetic fields observed by the Cassini magnetometer (MAG).

During the flyby, Cassini passed at the moon's equatorial plane through the mid-range magnetic tail of the moon at a distance of 10411 km. The magnetic field presented a strong Saturn-directed component, suggesting that the moon was located below the current sheet.

With the help of a particle tracing software that integrates the Lorentz equation of motion in the specific background fields obtained from the hybrid code, the effects that the different asymmetries on the field have on the access of particles to the moon's exobase (1450 km above the surface) are investigated and the variabilities that this difference in access around the moon have on the energy deposition are discussed.

References

[1] Arridge, C. S., Khurana, K. K., Russell, C. T., Southwood, D. J., Achilleos, N., Dougherty, M. K., Coates, A. J. and Leinweber, H. K.: Warping of Saturn's magnetospheric and magnetotail current sheets, Journal of Geophysical Research, Vol. 113, 2008.

[2] Wei, H. Y., Russell, C. T., Dougherty, M. K., Neubauer, F. M. and Ma, Y. J.: Second example of a cited book, Example Publishing House, 2000.

EPSC Abstracts
Vol. 10, EPSC2015-564, 2015
European Planetary Science Congress 2015

JUICE: A European Mission to Jupiter and its Icy Moons

O. Witasse (1), the JUICE Science Working Team and the JUICE Project Team
(1) European Space Agency, Noordwijk, The Netherlands (owitasse@cosmos.esa.int)

JUICE Science Working Team: S. Barabash, P. Brandt, L. Bruzzone, E. Bunce, B. Cecconi, T. Cavalie, G.Cimo, A. Coustenis, G. Cremonese, M. Dougherty, L. Fletcher, R. Gladstone, O. Grasset, L. Gurvits, P. Hartogh, H. Hoffmann, H. Hussmann, L. Iess, R. Jaumann, Y. Kasaba, Y. Kaspi, N. Krupp, Y. Langevin, D. Lasi, I. Mueller-Wodarg, P. Palumbo, G. Piccioni, J. Plaut, F. Poulet, K. Retherford, H. Rothkaehl, O. Santolik, D. J. Stevenson, T. Van Hoolst, J.-E. Wahlund, P. Wurz

JUICE Project Team: N. Altobelli, A. Atzei, M. Baroni, A. Cardesin, C. Erd, D. Escolar, D. Frew, R. Furnell, F.J. Garcia-Huete, P. Gare, F. Panin, T. Paulsen, G. Sarri, A. Schnorhk, F. Torelli, I. Torralba-Elipe, H. Van de Kamp, C. Vallat, S. Verstaen, A. Wielders, O. Witasse

Abstract

JUICE - JUpiter ICy moons Explorer - is the first large mission in the ESA Cosmic Vision 2015-2025 programme [1]. The mission was selected in May 2012 and adopted in November 2014. The implementation phase starts in July 2015, following the selection of the prime industrial contractor. Planned for launch in June 2022 and arrival at Jupiter in October 2029, it will spend at least three years making detailed observations of Jupiter and three of its largest moons, Ganymede, Callisto and Europa.

Science Objectives

The focus of JUICE is to characterise the conditions that might have led to the emergence of habitable environments among the Jovian icy satellites, with special emphasis on the three worlds, Ganymede, Europa, and Callisto, likely hosting internal oceans [2]. Ganymede, the largest moon in the Solar System, is identified as a high-priority target because it provides a natural laboratory for analysis of the nature, evolution and potential habitability of icy worlds and waterworlds in general, but also because of the role it plays within the system of Galilean satellites, and its unique magnetic and plasma interactions with the surrounding Jovian environment [3]. The mission also focuses on characterising the diversity of coupling processes and exchanges in the Jupiter system that are responsible for the changes in surface, ionospheric and exospheric environments at Ganymede, Europa and Callisto from short-term to geological time scales. Focused studies of Jupiter's atmosphere and magnetosphere, and their interaction with the Galilean satellites will further enhance our understanding of the evolution and dynamics of the Jovian system.

The overarching theme for JUICE is: *The emergence of habitable worlds around gas giants*. At Ganymede, the mission will characterise in detail the ocean layers; provide topographical, geological and compositional mapping of the surface; study the physical properties of the icy crusts; characterise the internal mass distribution, investigate the exosphere; study Ganymede's intrinsic magnetic field and its interactions with the Jovian magnetosphere. For Europa, the focus will be on the non-ice chemistry, understanding the formation of surface features and subsurface sounding of the icy crust over recently active regions. Callisto will be explored as a witness of the early solar system trying to also elucidate the mystery of its internal structure.

JUICE will perform a multidisciplinary investigation of the Jupiter system as an archetype for gas giants. The circulation, meteorology, chemistry and structure of the Jovian atmosphere will be studied from the cloud tops to the thermosphere. The focus in Jupiter's magnetosphere will include an investigation of the three dimensional properties of the magnetodisc and in-depth study of the coupling processes within the magnetosphere, ionosphere and thermosphere. Aurora and radio emissions will be elucidated.

JUICE will study the moons' interactions with the magnetosphere, gravitational coupling and long-term tidal evolution of the Galilean satellites.

The Payload

The JUICE payload consists of 10 state-of-the-art instruments plus one experiment that uses the spacecraft telecommunication system with ground-based instruments. This payload is capable of addressing all of the mission's science goals [2], from *in situ* measurements of the plasma environment, to remote observations of the surface and interior of the three icy moons, Ganymede, Europa and Callisto, and of Jupiter's atmosphere. A *remote sensing package* includes imaging (JANUS) and spectral-imaging capabilities from the ultraviolet to the sub-millimetre wavelengths (MAJIS, UVS, SWI). A *geophysical package* consists of a laser altimeter (GALA) and a radar sounder (RIME) for exploring the surface and subsurface of the moons, and a radio science experiment (3GM) to probe the atmospheres of Jupiter and its satellites and to perform measurements of the gravity fields. An *in situ package* comprises a powerful suite to study plasma and neutral gas environments (PEP) with remote sensing capabilities via energetic neutrals, a magnetometer (J-MAG) and a radio and plasma wave instrument (RPWI), including electric fields sensors and a Langmuir probe. An experiment (PRIDE) using ground-based Very Long Baseline Interferometry (VLBI) will support precise determination of the spacecraft state vector with the focus at improving the ephemeris of the Jovian system.

The table below lists the JUICE instruments.

Acronym	Instrument
3GM	Radio-Science experiment
GALA	Laser Altimeter
JANUS	Imaging system
J-MAG	Magnetometer
MAJIS	Visible-Infrared Hyperspectral Imaging Spectrometer
PEP	Particle Environment Package
RIME	Ice Penetrating Radar
RPWI	Radio and Plasma Wave Instrument
SWI	Submillimetre Wave Instrument
UVS	Ultraviolet Imaging Spectrograph

Main Mission Milestones

The table below lists the main milestones of the JUICE mission. The trajectory related events are taken from the current baseline scenario.

Date	Event
May 2012	Mission selection by ESA
February 2013	Payload selection by ESA
November 2014	Mission adoption by ESA
July 2015	Start of the implementation phase
June 2022	Launch
January 2030	Jupiter Orbit Insertion
September 2032	Ganymede Orbit Insertion
July 2033	End of mission

References

[1] JUICE Definition Study Report, Reference ESA/SRE(2014)1,2014. http://sci.esa.int/juice/54994-juice-definition-study-report/

[2] Grasset, O., et al., JUpiter ICy moons Explorer (JUICE): An ESA mission to orbit Ganymede and to characterise the Jupiter system, Planetary and Space Science, Volume 78, p. 1-21, 2013

[3] Grasset, O., et al., 2013. Planetary protection requirements at Ganymede, Astrobiology 13, issue 10, 991-1004.

EPSC Abstracts
Vol. 10, EPSC2015-590, 2015
European Planetary Science Congress 2015

Seasonal variations in Titan's stratosphere observed with Cassini/CIRS after the northern spring equinox

S. Vinatier (1), N. Teanby (2), S. Lebonnois (3), B. Bézard (1), N. Gorius (4), A. Mamoutkine (4), R. Achterberg (5,4) and the CIRS Team

(1) LESIA, Observatoire de Paris-Meudon, France, (2) School of Earth Science, University of Bristol, UK, (3) Laboratoire de Météorologie Dynamique, Université Paris 6, France, (4) NASA Goddard Space Flight Center, Greenbelt, USA, (5) University of Maryland, College Park, USA (Sandrine.vinatier@obspm.fr)

Abstract

Since 2004, Cassini has made more than 110 Titan flybys, observing its atmosphere with instruments including the Cassini Composite InfraRed Spectrometer (CIRS). We know from CIRS observations that the global dynamics drastically changed after the northern spring equinox that occurred in August 2009 ([1], [2], [3], [4]). The pole-to-pole middle atmosphere dynamics (above 100 km) experienced a global reversal in less than 2 years after the equinox [4], while the northern hemisphere was entering spring. This new pattern, with downwelling at the south pole, resulted in enrichment of almost all molecules inside the southern polar vortex, while a persistent enhancement due to the northern winter downwelling circulation is still seen in the north pole region (see Fig. 1 for HCN in February 2012). From General Circulation Model calculations, this single circulation cell pattern should remain until 2025.

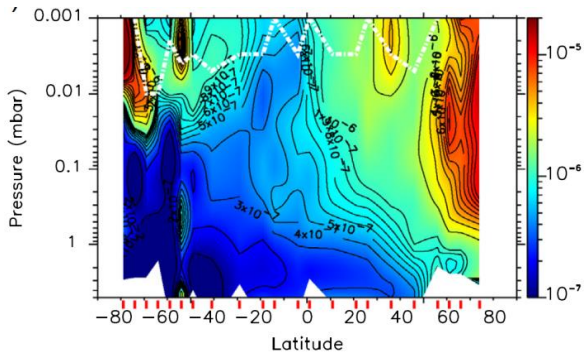

Figure 1: Pressure/latitude map of HCN mixing ratio in February 2012. White dashed line shows the levels above which constrains are poor.

We will present new 2015 CIRS limb observations analysis. We will show that many species (C_2H_2, HCN, HC_3N, C_6H_6, C_4H_2, CH_3CCH, C_2H_4) are now highly enriched near the south pole, by factors ~100 at 500 km compared to just a few years ago. Such large middle atmospheric enrichments were never seen before and are similar to in situ results from INMS at 1000 km [5].
We will also show that the north pole displays, for the first time since the beginning of the Cassini mission, a depletion of the molecular gas mixing ratios at altitudes higher than 300 km, while deeper levels remains enriched compared to mid-latitude regions.

References

[1] Teanby, N., et al.: Active upper atmosphere chemistry and dynamics from polar circulation reversal on Titan, Nature, 491, pp. 733-735, 2012.

[2] Achterberg et al.: Post-equinox variations of Titan's mid-atmospheric temperatures from Cassini CIRS observations, AAS Division for Planetary Science Meeting Abstract, 9-14 November 2014, Tucson, 2014.

[3] Coustenis et al.: Titan's south pole temporal evolution of HC3N and other trace gases, AAS Division for Planetary Science Meeting Abstract, 9-14 November 2014, Tucson, 2014.

[4] Vinatier et al.: Seasonal variations in Titan's middle atmosphere during the northern spring derived from Cassini/CIRS observations, Icarus, 250, 95-115, 2015.

[5] Cui et al.: Analysis of Titan's neutral upper atmosphere from Cassini Ion Neutral Mass Spectrometer measurements, Icarus, 200, 581-615, 2009.

EPSC Abstracts
Vol. 10, EPSC2015-635-1, 2015
European Planetary Science Congress 2015

Ion densities in Titan's ionosphere, multi-instrument case study

O. Shebanits (1,2), J.-E. Wahlund (1), N.J.T. Edberg (1), F.J. Crary (3), A. Wellbrock (4,5), A.J. Coates (4,5), D.J. Andrews (1), E. Vigren (1), K.E. Mandt (6), and J.H. Waite Jr (6)

(1) Swedish Institute of Space Physics, Uppsala, Sweden, (2) Department of Physics and Astronomy, Uppsala University, Uppsala, Sweden, (3) University of Colorado, Boulder, Massachusetts, USA, (4) Mullard Space Science Laboratory, University College London, Dorking, UK, (5) Centre for Planetary Sciences, University College London/Birkbeck, London, UK, (6) Space Science and Engineering Division, Southwest Research Institute, San Antonio, Texas, USA

Abstract

The Cassini s/c *in-situ* plasma measurements of Titan's ionosphere by Radio and Plasma Wave Science (RPWS) Langmuir Probe (LP), Cassini Plasma Spectrometer (CAPS) Electron (ELS) and Ion Beam (IBS) are combined for selected flybys (**T16**, **T29**, **T40** & **T56**) to further constrain plasma parameters of ionosphere at altitudes 880-1400 km.

1. Introduction

Saturn's largest moon Titan hosts an atmosphere with complex organic chemistry initiated in the ionosphere and responsible for the production of aerosols in Titan's signature orange haze [*1-10*]. Lower region of Titan's ionosphere has been shown to be populated by negative ions [*8, 11-15*] and dusty plasma/aerosols [*9, 15*], which are important for the complex organic chemistry of the moon [*7, 16*]. Altitude and solar zenith dependencies of the ion charge densities were analysed previously [*14, 15*]. However, the charge of the neg. ions and dust grains has so far only been predicted theoretically [*17*]. Also, the average mass of ions in the LP data analysis has previously been derived from INMS data which gives a good flyby-coverage but is limited to lighter pos. ions (<100 amu) [*15*]. CAPS/ELS and CAPS/IBS can both detect heavy ions, but lack the coverage, especially since the CAPS instrument has been turned off in June 2012. Since the all heavier ions are formed from lighter ones, the average masses of the heavier ions are expected to exhibit a dependency on the average masses of the lighter ions. This trend is indeed present (**Figure 1**) and effectively extends the legacy of now offline CAPS to all Titan flybys.

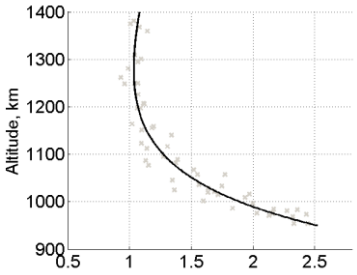

Figure 1. CAPS/IBS to INMS mean positive ion mass ratio

An immediate application is a correction of RPWS/LP-derived pos. and neg. ion charge densities, which reveals that previously reported densities [*15*] were severely underestimated (**Figure 2**). Combining the measurements of the negative ions/dust *density per charge* by CAPS/ELS with the negative ions/dust *charge density* by RPWS/LP gives a first empirical estimate of the negative ion/dust average charge to be ~2. Overall, the negative ion/dust *profiles* seem to match well between CAPS/ELS and RPWS/LP instruments (**Figure 2**).

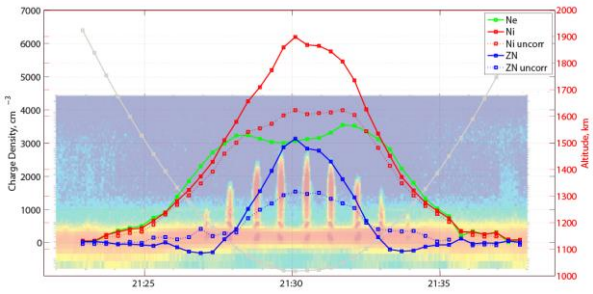

Figure 2. Example (T40) of RPWS/LP pos. (red, Ni) and neg. (blue, ZN) ion charge density correction with CAPS/ELS+IBS derived mass profiles. Dotted lines show the uncorrected densities; electron density (green, Ne) is shown for reference. Background: CAPS/ELS energy spectrum [*12*] with temporal scale adjusted to fit RPWS/LP.

Acknowledgements

The authors acknowledge funding and RPWS/LP instrument support by Swedish National Space Board and Cassini project support by NASA.

References

[1] T. E. Cravens, I. P. Robertson, J. H. Waite, R. V. Yelle, W. T. Kasprzak, C. N. Keller, S. A. Ledvina, H. B. Niemann, J. G. Luhmann, R. L. McNutt, W. H. Ip, V. De La Haye, I. Mueller-Wodarg, J. E. Wahlund, V. G. Anicich, V. Vuitton, Composition of titan's ionosphere. *Geophysical Research Letters* **33**, (Apr 11, 2006).

[2] T. E. Cravens, R. V. Yelle, J. E. Wahlund, D. E. Shemansky, A. F. Nagy, in *Titan from Cassini-Huygens*, R. Brown, J.-P. Lebreton, J. H. Waite, Eds. (Springer Netherlands, 2010), pp. 259-295.

[3] B. A. Magee, J. H. Waite, K. E. Mandt, J. Westlake, J. Bell, D. A. Gell, INMS-derived composition of Titan's upper atmosphere: Analysis methods and model comparison. *Planetary and Space Science* **57**, 1895 (Dec, 2009).

[4] K. E. Mandt, D. A. Gell, M. Perry, J. H. Waite, F. A. Crary, D. Young, B. A. Magee, J. H. Westlake, T. Cravens, W. Kasprzak, G. Miller, J. E. Wahlund, K. Agren, N. J. T. Edberg, A. N. Heays, B. R. Lewis, S. T. Gibson, V. de la Haye, M. C. Liang, Ion densities and composition of Titan's upper atmosphere derived from the Cassini Ion Neutral Mass Spectrometer: Analysis methods and comparison of measured ion densities to photochemical model simulations. *J Geophys Res-Planet* **117**, (Oct 12, 2012).

[5] J. H. Waite, Jr., H. Niemann, R. V. Yelle, W. T. Kasprzak, T. E. Cravens, J. G. Luhmann, R. L. McNutt, W. H. Ip, D. Gell, V. De La Haye, I. Muller-Wordag, B. Magee, N. Borggren, S. Ledvina, G. Fletcher, E. Walter, R. Miller, S. Scherer, R. Thorpe, J. Xu, B. Block, K. Arnett, Ion neutral mass spectrometer results from the first flyby of Titan. *Science* **308**, 982 (May 13, 2005).

[6] J. Cui, M. Galand, R. V. Yelle, V. Vuitton, J. E. Wahlund, P. P. Lavvas, I. C. F. Muller-Wodarg, T. E. Cravens, W. T. Kasprzak, J. H. Waite, Diurnal variations of Titan's ionosphere. *J Geophys Res-Space* **114**, (Jun 18, 2009).

[7] J. H. Waite, Jr., D. T. Young, T. E. Cravens, A. J. Coates, F. J. Crary, B. Magee, J. Westlake, The process of tholin formation in Titan's upper atmosphere. *Science* **316**, 870 (May 11, 2007).

[8] A. J. Coates, F. J. Crary, G. R. Lewis, D. T. Young, J. H. Waite, E. C. Sittler, Discovery of heavy negative ions in Titan's ionosphere. *Geophysical Research Letters* **34**, (Nov 28, 2007).

[9] P. Lavvas, R. V. Yelle, T. Koskinen, A. Bazin, V. Vuitton, E. Vigren, M. Galand, A. Wellbrock, A. J. Coates, J. E. Wahlund, F. J. Crary, D. Snowden, Aerosol growth in Titan's ionosphere. *Proceedings of the National Academy of Sciences of the United States of America* **110**, 2729 (Feb 19, 2013).

[10] H. B. Niemann, S. K. Atreya, S. J. Bauer, G. R. Carignan, J. E. Demick, R. L. Frost, D. Gautier, J. A. Haberman, D. N. Harpold, D. M. Hunten, G. Israel, J. I. Lunine, W. T. Kasprzak, T. C. Owen, M. Paulkovich, F. Raulin, E. Raaen, S. H. Way, The abundances of constituents of Titan's atmosphere from the GCMS instrument on the Huygens probe. *Nature* **438**, 779 (Dec 8, 2005).

[11] K. Ågren, N. J. T. Edberg, J. E. Wahlund, Detection of negative ions in the deep ionosphere of Titan during the Cassini T70 flyby. *Geophysical Research Letters* **39**, (2012).

[12] A. J. Coates, A. Wellbrock, G. R. Lewis, G. H. Jones, D. T. Young, F. J. Crary, J. H. Waite, Heavy negative ions in Titan's ionosphere: Altitude and latitude dependence. *Planetary and Space Science* **57**, 1866 (Dec, 2009).

[13] A. J. Coates, A. Wellbrock, G. R. Lewis, G. H. Jones, D. T. Young, F. J. Crary, J. H. Waite, R. E. Johnson, T. W. Hill, E. C. Sittler, Negative ions at Titan and Enceladus: recent results. *Faraday Discussions* **147**, 293 (2010).

[14] A. Wellbrock, A. J. Coates, G. H. Jones, G. R. Lewis, J. H. Waite, Cassini CAPS-ELS observations of negative ions in Titan's ionosphere: Trends of density with altitude. *Geophysical Research Letters*, (2013).

[15] O. Shebanits, J.-E. Wahlund, K. Mandt, K. Ågren, N. J. T. Edberg, J. H. Waite, Negative ion densities in the ionosphere of Titan–Cassini RPWS/LP results. *Planetary and Space Science* **84**, 153 (2013).

[16] V. Vuitton, P. Lavvas, R. V. Yelle, M. Galand, A. Wellbrock, G. R. Lewis, A. J. Coates, J. E. Wahlund, Negative ion chemistry in Titan's upper atmosphere. *Planetary and Space Science* **57**, 1558 (Nov, 2009).

[17] M. Horányi, T. W. Hartquist, O. Havnes, D. A. Mendis, G. E. Morfill, Dusty plasma effects in Saturn's magnetosphere. *Reviews of Geophysics* **42**, (2004).

EPSC Abstracts
Vol. 10, EPSC2015-644, 2015
European Planetary Science Congress 2015

On the possibility of Serpentinization on Enceladus

Silas Boye Nissen (1), **Ruth-Sophie Taubner** (2,3), Johannes J. Leitner (2,3,4), Maria G. Firneis (2,3)
(1) Astrophysics and Planetary Science, University of Copenhagen, Copenhagen, Denmark, (2) Research Platform: ExoLife, University of Vienna, Vienna, Austria, (3) Institute of Astrophysics, University of Vienna, Vienna, Austria, (4) SCI.E.S.COM., Hernstein, Austria. (boyenissen@nbi.ku.dk or ruth-sophie.taubner@univie.ac.at)

Abstract

This work studies the possibility of serpentinization at the water/rock boundary of Enceladus (pH 7–9, 25–50 bars, and 0–50 °C), and further estimates the hydrogen production rates. Thermodynamic databases were created with the DBCreate program [10], and geochemical modeling was applied with the EQ3/6 software package [2]. The chemical composition of the subsurface aquifer is assumed to be similar to the plumes. Nine scenarios were tested to specify the core composition. It is shown that serpentinization seems to be possible at the water/rock boundary on Enceladus if an iron-rich end-member is present in the core.

1. Introduction

Enceladus, an icy moon of Saturn, is considered a potential place for a second genesis of life in a rather easy accessible environment for future space missions[5]. Plumes erupting material out to Saturn's E ring have been detected[6]. This and the latest gravity data received by NASA's Cassini probe highly suggest a regional subsurface water reservoir to exist[1]. The Cassini mission has detected most of the necessary elements for life (C,H,N,O,P,S) in these plumes[9], and three ecosystems known from the Earth could in theory exist in the subsurface environment [4]. These ecosystems rely on a sufficient hydrogen source. On Earth, this molecule is known to be produced when the oceans interact with silicates in the mantle through a geochemical process called serpentinization. The aim of this work is first of all to examine whether serpentinization is possible on Enceladus at an assumed pressure of 25-50 bars [7] and a temperature of 0-50°C. If it is possible, then the second aim is to estimate the hydrogen production rate.

2. Methods

Geochemical modeling with the EQ3/6 software package has been applied [10], and thermodynamic databases have been created with the DBCreate program [2]. Due to the present lack of data on the chemical composition of the subsurface sea, it is assumed to equal the chemical composition of the plumes. Nine scenarios based on Enceladus being a captured comet or consisting of aggregated ring material are used to specify the core composition. These are different combinations of pyroxenes and olivines or no silicates, respectively. As an example the chemical evolution for the model with 1.0 mol fayalite is shown in Figure 1.

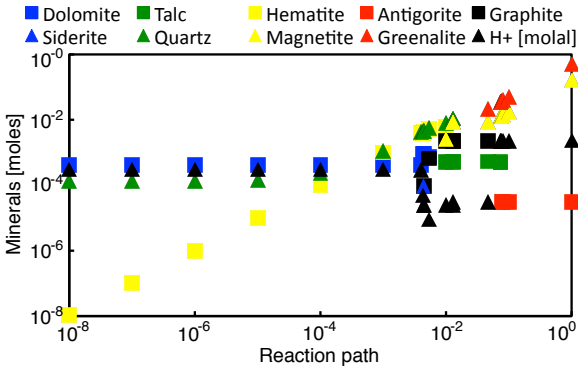

Figure 1: Moles of product minerals as a function of the reaction path for the model with 1.0 mol fayalite at 25 bars, 0 °C and pH 9. Carbonate minerals are blue, silicate minerals are green, oxide minerals are yellow, minerals in the serpentine group are red, graphite (C) and hydrogen are black. Notice: The hydrogen concentration is given in molality on the same scale.

3. Results

Minerals in the serpentine group are produced in the end of the reaction with antigorite and greenalite produced simultaneously. The hydrogen production rate

decreases in the central part and increases towards the end. Serpentines were only produced in the presence of an iron-rich end-member. In this case the hydrogen production increases in the end. To calculate the hydrogen production rates, numerical integration of hydrogen to the entire reaction in the different scenarios was applied. The results of the nine scenarios in the four different environments can be found in Table 1.

Table 1: Hydrogen production rates [mg H_2 / kg solution] for nine scenarios tested for four set of parameters.

pH	9	7	9	9
Pressure [bars]	25	25	50	25
Temperature [°C]	0	0	0	50
All five minerals[a]	1.9	1.9	1.8	1.9
All three pyroxenes[a]	2.1	2.1	2.1	2.2
Both olivines[a]	2.4	2.4	2.4	2.4
1.0 mol diopside	0.0	0.0	0.0	0.0
0.9 mol enstatite	0.0	0.0	0.0	0.02
2.8 mol ferrosilite	0.03	0.03	0.03	0.56
3.9 mol forsterite	0.0	0.0	0.0	0.0
1.0 mol fayalite	2.2	2.2	2.2	2.2
None minerals[b]	-	-	-	-

[a]The distribution of the minerals is equivalent to the distribution found in the nucleus of comet 9P/Tempel 1[3]. [b]Serpentinization did not occur in the model with no minerals.

4. Discussion

The complex aqueous solution assumed (based on the composition of the plumes) affects the serpentinization process on Enceladus. In addition, the pressure and temperature ranges might be too small to make a significant change on the hydrogen concentration. To improve the estimate of the hydrogen production rate, measurements for the silicate ions in the aqueous solution on Enceladus are needed.

5. Conclusions

This work shows that serpentinization seems to be possible at the low pressure and temperature likely found at the water/rock boundary on Enceladus. Hydrogen is only produced in the presence of an iron-rich end-member. In these scenarios, the hydrogen concentration is estimated to be around 2.0 mg/kg solution. Hence, the resulting available amount of hydrogen in the subsurface aquifer could be sufficient to serve as a substrate for hydrogenotrophic methanogenic life on Enceladus [8].

Acknowledgements

We would like to thank Wolfgang Bach from the Research Group "Petrology of the Ocean Crust" (University of Bremen) for his very helpful support on applying the geochemical modeling software.

References

[1] Iess, L. et al.: The Gravity Field and Interior Structure of Enceladus, Science, 344, pp. 78-80, 2014.

[2] Kong, X.-Z. et al.:. DBCreate: A SUPCRT92-based program for producing EQ3/6, TOUGHREACT, and GWB thermodynamic databases at user-defined T and P. Computers & Geosciences, 51, pp. 415-417, 2013.

[3] Lisse, C. M. et al.: Spitzer Spectral Observations of the Deep Impact Ejecta. Science, 313, pp. 635-640, 2006.

[4] McKay, C. P. et al.: The Possible Origin and Persistence of Life on Enceladus and Detection of Biomarkers in the Plume. Astrobiology, 8, pp. 909-919, 2008.

[5] McKay, C. P. et al.: Follow the Plume: The Habitability of Enceladus, Astrobiology, 14, pp. 352-355, 2014.

[6] Spencer, J. R. et al.: Cassini Encounters Enceladus: Background and the Discovery of a South Polar Hot Spot, Science, 311, pp. 1401-1405, 2006.

[7] Taubner, R.-S. et al.: The Inner Structure of Enceladus, Journal Origins of Life and Evolution of Biospheres, 2014 (submitted).

[8] Taubner, R.-S. et al.: Methanogenic Life in the Solar System: an Assessment of Methanogen (Eco-)physiology in the Context of Recent Astrobiological and Planetological Studies, Life (submitted).

[9] Waite, J. H. et al.: Liquid water on Enceladus from observations of ammonia and 40Ar in the plume, Nature, 460, pp. 487-490, 2009.

[10] Wolery, T. J.: EQ3/6: Software for Geochemical Modeling, Version 8.0, UCRL-CODE-2003-009, Lawrence Livermore National Laboratory, Livermore, California, 2002

EPSC Abstracts
Vol. 10, EPSC2015-652, 2015
European Planetary Science Congress 2015

Organic compounds from Enceladus' sub-surface ocean as seen by CDA

N. Khawaja (1), F. Postberg (1,2), R. Reviol (1), F. Klenner (1), L. Nölle (1), R. Srama (2)

(1) Institute of Earth Sciences, University of Heidelberg, Germany, (2) IRS, University of Stuttgart, Germany (nozair.khawaja@geow.uni-heidelberg.de)

Abstract

The ice and dust particles ejected into Saturn's E-ring provide direct insight into the composition of Enceladus' sub-surface ocean. This ocean is in contact with the rocky-core and there is evidence for hydrothermal activity [1][2]. Chemical species in the liquid are transported through vents and ejected out of Enceladus in the form of gas and ice particles. The volatile organic components found in the gas phase have already been thoroughly investigated [3]. Here we perform a compositional analysis of mass spectra from organic-rich ice grains and infer the composition of the refractory organic component of the plume. As expected, we find more complex organic molecules than in the gas. Among others we identify fingerprints of different aromatic compounds and amines.

1. Introduction

Enceladus is emitting a plume of gas and ice particles from its fractured South Polar Terrain (SPT), the so-called "Tiger Stripes". The source of Enceladus plume and of the E-ring is the moon's sub-surface ocean. The chemical species ascending from the liquid reservoir, transported through vents and ejected into space include organic molecules [3][4][5].

Three compositional types of ice grains have already been identified by the Cosmic Dust Analyzer (CDA) onboard Cassini spacecraft; Type-1—almost pure water, Type-2—organic rich and Type-3—salt rich [4][5].

In contrast to Type-1 and Type-3 spectra, which have already been well characterized, organic rich Type-2 spectra have not yet been investigated in detail. Type-2 spectra display great diversity indicating varying contribution of different organic species. A multitude of organic species has already been identified in the plume of gas [3]. By analyzing organic rich Type-2 grains we can access refractory organic compounds from Enceladus' sub-surface ocean. The composition of Type-2 spectra is inferred using a laboratory experiment that provides analogues for spectra from ice particle impacts. The simulation of a variety of organic compounds in a water matrix allows us to identify characteristic families among Type-2 spectra and attribute them to certain class of organic compounds.

2. Experimental setup

We simulate CDA Type-2 spectra with an experimental setup in our Heidelberg laboratory: Infrared Matrix Assisted Laser Desorption Ionisation Time of Flight Mass Spectrometer (IR-MALDI-TOF-MS). An aqueous solution of organic compounds is vertically injected in the form of a liquid microbeam of about 10 µm in diameter. The liquid beam is shot and ionized by a pulsed infrared laser with a wavelength of 2850 nm. The adjustable setup successfully simulates different impact energies of impinging ice grains onto the CDA metal target at different impact velocities. The generated cations are accelerated towards a reflectron-type Time-of-Flight mass spectrometer.

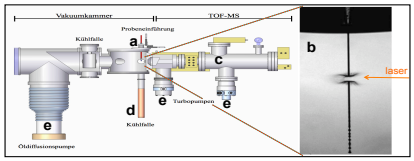

Fig. 1: Shown is the experimental setup to simulate CDA organic rich Type-2 spectra at different impact velocities. (a) beam site. (b) beam irradiated by laser. (c) mass spectrometer. (d) cryotrap. (e) pumps. [6]

3. Results

Among other compounds we have identified characteristic fragments patterns of two classes of organics: (i) aromatics (ii) amines. Typically fragment cations of aromatic compounds are stable at velocities up to 15 km/s and of amines up to velocities of 8 km/s.

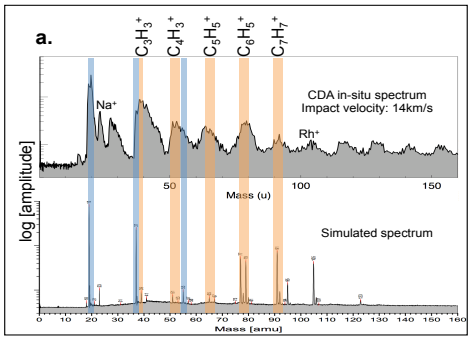

Fig. 2a: Characteristic fragments of aromatic compounds | An aqueous solution of benzoic acid (C_6H_5-COOH, 0.15% mol/kg) with benzyl alcohol (C_7H_7-OH, 2.5% mol/kg) is used to simulate the CDA in-situ spectrum of aromatic compounds. Orange stripes show characteristic fragments pattern ($C_nH_{\leq n}^+$) of aromatic compounds at mass lines 39, 51, 65, 77 and 91(u) (u = unified atomic mass unit), whereas blue stripes show pure water cluster species $H^+(H_2O)_{n=1-3}$. Generally Tropylium cations ($C_7H_7^+$: 91u) form from a benzyl group (C_7H_7-R) whereas Phenyl cations ($C_6H_5^+$: 77u) form from oxygen bearing aromatic compounds (C_6H_5-COR). Fragments from other organic species are also present but not labelled.

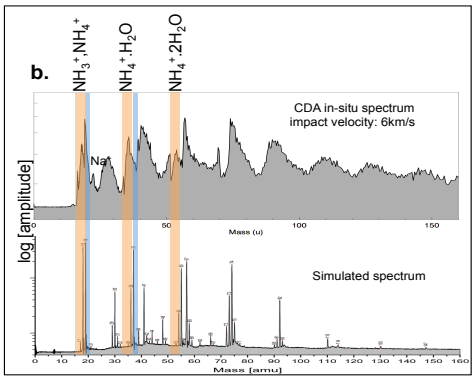

Fig. 2b: Characteristic mass lines of amines | An aqueous solution of butyl-amine (C_4H_9-NH_2, 5% mol/kg) is used to characterize amines in the CDA ice grain spectrum. Orange stripes show the characteristic pattern of amine compounds in a water matrix at mass lines 17, 18, 36 and 54 (u), whereas blue stripes shows pure water cluster species $H^+(H_2O)_{n=1,3}$. The major characteristic fragment of amines is the mass line at 18u (NH_4^+). The ammonium cation (NH_4^+) forms cluster species with water at mass lines 36u and 54u of the form $NH_4^+.(H_2O)_{n=1,2}$. Fragments from other organic species are also present but not labelled.

4. Summary and Conclusions

Our experimental setup in Heidelberg (IR-MALDI-TOF-MS) provides a better understanding of organic-rich CDA-TOF spectra of ice particles from Enceladus over a wide range of impact velocities. Among others two organic families, aromatics and amines could be identified in the ice matrix. Type-2 spectra show contributions from other, yet unspecified, organic species. This demonstrates that the analysis of Type 2 grains is a key element in understanding of Enceladus subsurface processes. Currently work is in progress to verify other organic families in the dataset. In future work we will quantify concentrations of organic compounds in the ice grains emitted from Enceladus.

Acknowledgements

This work is supported by DFG-Deutsche Forschungsgemeinschaft grants PO1015/2-1 and PO1015/4-1.

References

[1] Hsu, H.W. et.al.: Nature, Vol. 519, 207-210, 2015.

[2] Iess, L. et.al.: Science, Vol. 344, 78-80, 2014.

[3] Waite Jr., J. H. et.al.: Nature, Vol. 460, 487-490, 2009.

[4] Postberg, F. et.al.: Nature, Vol. 459, 1098-1101, 2009.

[5] Postberg, F. et.al.: Icarus, Vol. 193, 438-454, 2008.

[6] Beinsen, A.: Dissertation 2011, Georg-August-Universität Göttingen.

EPSC Abstracts
Vol. 10, EPSC2015-659, 2015
European Planetary Science Congress 2015

Longitudinal librations of Titan and Enceladus

T. Van Hoolst (1,2), R.M-Baland (3), M. Yseboodt (1), A. Trinh (1)
(1) Royal Observatory of Belgium, Brussels, Belgium, (2) Institute of Astronomy, KU Leuven, Belgium, (3) Université catholique de Louvain, Earth and Life Institute, Louvain-la-Neuve, Belgium, (tim.vanhoolst@oma.be)

1 Abstract

The rotation rate of Titan, the largest satellite of Saturn, and of Enceladus, the most geologically active satellite of Saturn, is on average equal to their orbital mean motion. Here we discuss small deviations from the average rotation synchronous with their orbital motion. We examine different causes at various time scales and assess possible consequences and the potential of using librations as a probe of the interior structure of the satellites.

2 Discussion

As a result of the significant non-spherically symmetric mass distribution of the satellites (Iess et al. 2012, Iess et al. 2014), the 1:1 spin-orbit resonance of Titan and Enceladus is stable. Small variations in the rotation rate around the equilibrium state are, nevertheless, expected as a result of different torques acting on the satellites. For Titan, deviations from the synchronous state have been reported several times (Lorenz et al. 2008, Stiles et al 2008, Stiles et al. 2010, Meriggiola et al. 2012). The measurements of the rotation variations are based on determinations of the shift in position of Cassini SAR radar images taken during different flybys. The results, however, are inconclusive and the spin variations are smaller for the latest studies. For Enceladus, it has been suggested that librations may play a role in the temporal variation in the plume activity (Nimmo et al. 2014).

Theoretical estimates show that variations in the rotation rate can occur for several reasons (Van Hoolst et al. 2013, Jara-Orué and Vermeersen 2014). First, the rotation of the Saturnian satellites changes with a period equal to their orbital period as a result of the gravitational torque exerted by Saturn. Second, free librations with periods much longer than the orbital period might be excited. Third, deviations from a Keplerian orbit perturb the rotation at additional frequencies. Fourth, dynamic variations in the atmosphere of Titan induce changes in Titan's rotation with a main period equal to half the orbital period of Saturn.

The librations contain information on the interior of the satellite, and in particular can be used to constrain several properties of the ice shell of Titan (Van Hoolst et al. 2013). Here, we report on different theoretical aspects of the librations and compare theoretical predictions with observational results. We consider the influence of the rheology of the ice shell and take into account Cassini measurements of the external gravitational field and of the topography of Titan and Enceladus. We also evaluate the librations induced by Titan's hydrocarbon seas and use the most recent results of Titan's atmosphere dynamics.

Acknowledgements

This work was financially supported by the European Space Agency in collaboration with the Belgian Federal Science Policy Office.

References

[1] Iess, L., and 10 colleagues, 2014. The Gravity Field and Interior Structure of Enceladus, Science 344, 78-80

[2] Iess, L., and 9 colleagues, 2012. The tides of Titan, Science, Vol. 337, 457-459

[3] Jara-Orué, H.M., Vermeersen, B.L.A., 2014. The forced libration of Europa's deformable shell and its dependence on interior parameters, Icarus 229, 31–44

[4] Lorenz, R.D. et al., 2008. Titan's rotation reveals an internal ocean and changing zonal winds. Science 319, 1649–1651

[5] Meriggiola, R., Iess, L., 2012. A new rotational model of Titan from Cassini SAR data. In: European Planetary Science Congress 2012, EPSC Abstracts EPSC2012-593.

[6] Nimmo, F., Porco, C., Mitchell, C., 2014. Tidally modulated eruptions on Enceladus: CASSINI observations and models. Astron. J. 148:46

[7] Richard, A., Rambaux, N., Charnay, B., 2014. Librational response of a deformed 3-layer Titan perturbed by non-Keplerian orbit and atmospheric couplings, Planetary and Space Science 93-94, 22–34

[8] Stiles, B.W. et al., 2008. Determining Titan's spin state from Cassini radar images. Astron. J. 135 (5), 1669–1680. http://dx.doi.org/10.1088/0004-6256/135/5/ (see also 2010, Astron. J. 139 (1), article id. 311, for an erratum)

[9] Van Hoolst, T., Baland, R.M., Trinh, A., 2013. On the librations and tides of large icy satellites. Icarus 226, 299–315

EPSC Abstracts
Vol. 10, EPSC2015-687, 2015
European Planetary Science Congress 2015

Simultaneous mapping of Titan's surface albedo and aerosol opacity from Cassini/VIMS massive inversion

Luca Maltagliati (1), Sébastien Rodriguez (1), Christophe Sotin (2,3), Thomas Cornet (4), Pascal Rannou (5), Stéphane LeMouelic (2), Anezina Solomonidou (3), Athena Coustenis (6) and Robert Brown (7).
(1) Laboratoire AIM, CEA/Saclay, Gif/Yvette, France. (2) LPG, Nantes, France. (3) JPL, Pasadena, CA, USA. (4) ESAC/ESA, Villanueva de la Cañada, Madrid, Spain. (5) GSMA, Reims, France. (6) LESIA, Meudon, France. (7) University of Arizona, Tucson, US.

Abstract

Titan still lacks information on the cartography of its surface albedo, due to the complications linked to the treatment of the atmospheric contributions on surface observations. We present in this paper the results of our massive inversion method that we developed to treat Cassini/VIMS hyperspectral data of Titan. Our minimization procedure is based on look-up tables (LUTs) we create from a state-of-the-art radiative transfer (RT) model [1]. This allows us to decrease the computational time by a factor of several thousands with respect to the standard radiative transfer applications. We will present the improvements on the RT modeling thanks to the acquisition of new information on Titan's aerosol properties and our results for the simultaneous mapping of Titan's surface albedo and aerosol abundance in some regions of interest.

1. Introduction

Knowledge of surface albedo of a body is essential to constrain its composition and, consequently, its geological history. This is particularly true for infrared observations, where a wealth of absorption bands of ices and minerals are located. However, albedo maps of Titan still do not exist. This lack of information, even more striking considering that the Cassini mission has been observing Titan since 2004, is due to the thick atmosphere of the Saturn's satellite. First of all, a series of methane absorption bands make the infrared spectrum opaque at most near-IR wavelengths. Titan's surface is thus only visible around 7 narrow spectral atmospheric windows centered at 0.93, 1.08, 1.27, 1.59, 2.01, 2.7-2.8 and 5 μm (Fig. 1). Moreover, the thick aerosol haze affects the whole spectral range, transparency windows included, in a complex way through absorption and scattering processes.

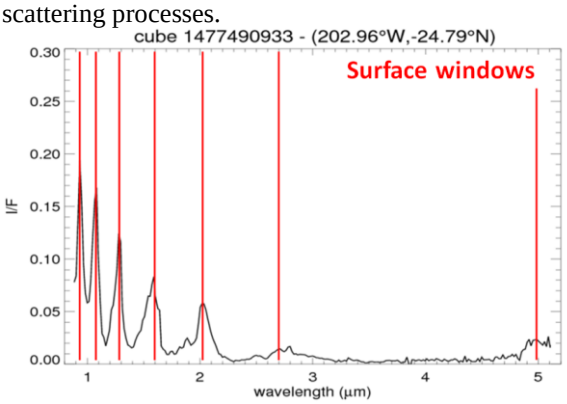

Figure 1: near-IR spectrum of Titan in nadir geometry from a pixel of a VIMS datacube.

The most rigorous way to treat the atmospheric effects on Titan in order to get the surface albedo is through radiative transfer models. They have, however, two main drawbacks. First, they are very demanding in computational time and thus inadequate to treat big datasets. Then, a precise description of aerosol properties is needed. Yet, up to recently we had direct measurements of Titan's aerosol properties only at the moment of the Huygens descent, thus linked to a specific place and time [2], when we know that the aerosol distribution depends on latitude and season [3][4].
In the next two Sections we describe how our method takes into consideration both these issues.

2. Massive inversion of VIMS data

The mapping spectrometer VIMS onboard Cassini is the best-suited instrument to extract maps of Titan's surface albedo with good spatial resolution. In the ~100 flybys of Cassini over Titan, VIMS has recorded ~ 40,000 hyperspectral images of the moon, gathering several millions of spectra. Considering

that the classical radiative transfer solvers, as the one employed by our reference RT model [1], process the minimization of a single spectrum on a timescale of the order of ~1-10 minutes, their employment to study the VIMS dataset is unreasonable.

Our approach is to apply our RT model not directly to the inversion, but to create lookup tables (LUTs) for different values of the model's input parameters: the three angles that define the geometry (incidence, emergence, azimuth), and the two physical characteristics (haze total opacity and surface albedo). We performed a thorough analysis in the parameters' space to obtain the optimized LUTs grid for the five parameters. At the end, 8 values are used for incidence and emergence, 6 for the azimuth, 4 for the haze opacity and 3 for the surface albedo, for a total of 4608 spectra in a LUT. Once a LUT is ready, it is fed to ad ad-hoc minimization routine that creates simultaneous maps of haze opacity and surface albedo. For a 64×64 datacube, these maps are obtained in less than a minute, a huge gain with respect to the ~10 days needed with classical minimization procedures with full RT (Fig. 2).

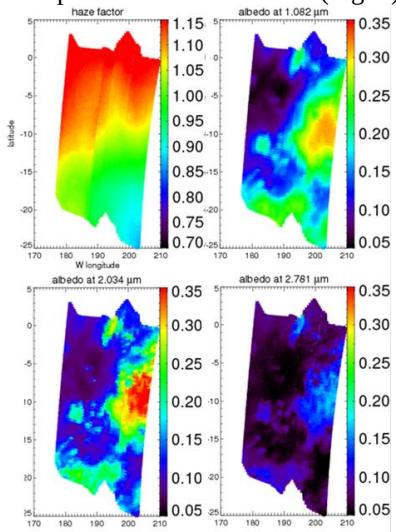

Figure 2: maps of haze opacity (top left) and albedo in different surface windows for a VIMS cube over the Huygens landing site.

3. Improving the aerosols with the T88 "EPF" observation

As mentioned above, in order to consider correctly the atmospheric contribution on the observations, the characteristics of the aerosols must be known as precisely as possible. On Titan the lack of direct observations is a significant drawback and the first results of our massive inversion showed a clear dependence of the output aerosol opacity with the geometry of the observation. In order to improve the aerosol description, we analyzed an "Emergence-Phase Function'' (or EPF) recently acquired by VIMS during the T88 flyby. It consists of 25 cubes targeting the same area at a constant incidence angle of ~51^{o} and with varying emergence and phase angles (from 0 to 60^{o}). We then changed the trend of the integrated aerosol extinction with wavelength and the aerosol phase function, previously fixed in our model [1] by the results of [2]. With this study we have constrained a new description of aerosols' extinction and phase function that improve significantly the reproduction of the EPF data by our model.

4. Conclusions

We apply our massive inversion method, with improved information from aerosol properties, to several datacubes of VIMS. We will study in particular the Huygens landing site, useful also for method validation by comparing our results with Huygens itself, and some regions of interest as for example the vast region (-40°-+40° latitude, -20°-+40° longitude) covered by two flybys (T13/T17) in quick succession.

Acknowledgements

The authors thank the Agence Nationale de la Recherche for the ANR Project "APOSTIC" n° 11BS56002 (France).

References

[1] Hirtzig M. et al., Icarus, 226, 470-486, 2013.

[2] Tomasko M.G. et al., PSS, 56, 669-707, 2008.

[3] Maltagliati L. et al., Icarus, 248, 1-24, 2015.

[4] West R.A. et al., GRL, 38, L06204, 2011.

EPSC Abstracts
Vol. 10, EPSC2015-703, 2015
European Planetary Science Congress 2015

A search for waves in Saturn's stratosphere with TEXES/IRTF

S. Guerlet (1), T.K. Greathouse (2) and T. Fouchet (3)
(1) Laboratoire de Météorologie Dynamique/IPSL/CNRS, Paris, France (2) South West Research Institute, San Antonio, Texas, USA (3) LESIA/Observatoire de Paris, Meudon, France (sandrine.guerlet@lmd.jussieu.fr)

Abstract

We report on the mapping of Saturn's stratospheric temperature in April 2015 using the Texas Echelon cross Echelle Spectrograph (TEXES, [1]) mounted on NASA's Infrared Telescope Facility (IRTF). Our goal is to study the thermal structure of Saturn's equatorial oscillation in 2015 and to search for the signature of thermal waves.

1. Introduction

In planetary middle atmospheres, waves play a critical role in the transport of momentum and energy. On Earth, interactions between vertically propagating waves and the mean zonal flow at the equator lead to a well-known dynamical phenomenon referred to as the Quasi-Biennial Oscillation (QBO) [2]. The QBO is characterized by an oscillation of the mean zonal wind and temperature of the equatorial stratosphere with a period of 22-34 months. At a given time, the vertical atmospheric profile shows a pattern of local minima and maxima of temperature alternating with height, as well as eastward and westward winds alternating with height. This pattern then propagates downwards over time.

An analoguous oscillation has recently been observed in Saturn's equatorial stratosphere [3, 4, 5], suggesting that equatorial oscillations are a common feature in planetary stratospheres. Ground-based observations have estimated the period of Saturn's oscillation to be 15 Earth years [3], hence half a Saturn year. However, the thermal structure of Saturn's stratosphere in 1980, derived from a re-analysis of Voyager observations, is inconsistent with a 15-year period for the oscillation [6]. In addition, the downward propagation of the oscillation may have been disturbed by the 2010 great storm.

Further observations of Saturn's vertical and meridional temperature gradients are thus needed to better characterize Saturn's equatorial oscillation and its period. In addition, observations resolving the longitudinal temperature field could reveal atmospheric waves, which properties (their horizontal and vertical wavelengths, phase velocities) are poorly documented. A better knowledge of the waves properties will help evaluate their role on the forcing of Saturn's oscillation, which mechanism is still poorly known.

2. Data analysis

Saturn was observed in the beginning of April, 2015 in two spectral regions and observing modes:

- High resolution (R$\sim$ 75,000) observations were performed in the methane ν_4 emission band (1245–1250 cm^{-1}) in nodding mode, with the TEXES slit oriented North/South and set at the central meridien of the planet. The longitudinal coverage was achieved by letting the planet rotate in the background.

- Medium resolution (R$\sim$15,000) scans of the planet were performed in the ethane band (815–822 cm^{-1}), achieving a much higher signal to noise ratio but with a less extended vertical sensitivity.

Temperature is first retrieved from the methane emission spectra, which probe the stratosphere between 10 and 0.01 mbar [7]. However, the signal to noise ratio is such that methane spectra acquired at different longitudes have to be co-added. Consequently, these observations are used to derive mean zonal temperature vertical profiles, at several latitudes.

On the other hand, temperature profiles can also be retrieved from the analysis of the ethane spectra, assuming a vertical profile for the ethane volume mixing ratio at a given latitude. Ethane abundance profiles are set to that retrieved from Cassini/CIRS observations, which revealed that ethane undergoes very little seasonal variations in the middle stratosphere [8].

Hence, these TEXES observations can be used to derive temperature variations with longitude and search for waves in Saturn's equatorial region.

Acknowledgements

S. Guerlet aknowledges funding by the French ANR under grant agreement ANR-12-PDOC-0013.

References

[1] Lacy, J. et al., Publ. Astron. Soc. Pacific Vol. 114, p.153–168, 2002.

[2] Baldwin, M.P. et al., Reviews of Geophysics, Volume 39, Issue 2, p. 179–229, 2001.

[3] Orton, G. et al., Nature Vol. 453, Issue 7192, p. 196–199, 2008.

[4] Fouchet, T. et al., Nature Vol. 453, Issue 7192, p. 200–202, 2008.

[5] Guerlet, S. et al., Geophys. Res. Let. Vol 38, Issue 9, 2011.

[6] Sinclair, J. et al., Icarus Vol. 233, p. 281-292, 2014.

[7] Greathouse, T.K. et al., Icarus Vol. 177, p. 18–31, 2005.

[8] Sylvestre, M. et al., submitted to Icarus

EPSC Abstracts
Vol. 10, EPSC2015-706, 2015
European Planetary Science Congress 2015

Fractal analysis of Ganymede grooves distribution and subsurface ocean depth

R. Pozzobon (1), F. Mazzarini (2) G. Cremonese (1) A. Lucchetti (3,1) C. Re (1) M. Massironi (4, 1)

(1) INAF-Astronomical Observatory of Padova,Italy (2) Istituto Nazionale di Geofisica e Vulcanologia, Italy (3) CISAS, University of Padova (4) Dipartimento di Geoscienze, University of Padova

Abstract

Jupiter's moon Ganymede is an icy body that presents a peculiar surface and interior. Data collected by Voyager and Galileo missions showed a complex tectonic history on its surface to hypothesize the presence of a subsurface ocean. Most of the structures on the satellite's surface appear to be dark heavily cratered material crosscut by extensional grabens filled with smooth light albedo young material, probably related to subsequent cryovolcanic infilling. In this work we present for the first time a fractal clustering analysis of these structures whose spatial relationship was used to verify their relationship to a fractured percolating network directly connected to the subsurface ocean. In addition we were able to calculate the depth of the ocean that likely feeds the grabens with cryovolcanic slush material responsible for resurfacing events. The obtained depth value of ~250 km is moreover in agreement with the ocean depth values of 250 km calculated with the study of auroras on Ganymede.

1. Introduction

Jupiter's moon Ganymede, the largest satellite in our solar system, is a fully differentiated body and the only known satellite with an internal dynamo field [1]. It possesses an iron core, the source region of the dynamo, a silicate mantle, and an ice mantle as the outer layer [2]. The key question about Ganymede is whether it possesses a subsurface water ocean under its icy crust. Magnetic field data returned by the Galileo mission suggest that both Ganymede has a conducting layer at a depth between 170 and 460 km in which a magnetic field is being induced [3]. The simplest explanation for these observations calls for subsurface oceans or layers of partially molten ice. Several theoretical models of Ganymede's interior suggest the possibility of a subsurface ocean (e.g. [4], [5], [6], [7]).

Recent observations of HST [8] have been used to search for an ocean within Ganymede by monitoring the variability of the locations of the auroral ovals. The observations require a minimum electrical conductivity of 0.09 S/m for an ocean assumed to be located between 150 km and 250 km depth or alternatively a maximum depth of the top of the ocean at 330 km.

1.1 Geologic context

Terrains on Ganymede could be divided into two different macro-units: dark heavily cratered terrains and light albedo smooth terrains that often presents planetary-scale smooth lanes and regional graben systems that crosscut dark materials. The lower crater density of light albedo material demonstrates their younger age. From Galileo SSI higher resolution images the lanes and grabens indeed appear furrowed and marked by parallel grooves most likely to be related to extensional tectonic features. It has been recently debated on the mechanism forming the light albedo material and the proposed models involve both fault-block tilting in extensional zones then disrupted or cryovolcanically flooded [9]. However there is no clear evidence on the depth of the source of the cryovolcanic material. On the basis of the wide dataset available on USGS servers (provided by the authors of the first geologic map of Ganymede, [10]) several grooves and furrows are visible both at planetary and local scales that could be analysed in terms of spatial distribution and clustering. We chose a window size of ~2000 km for our study area

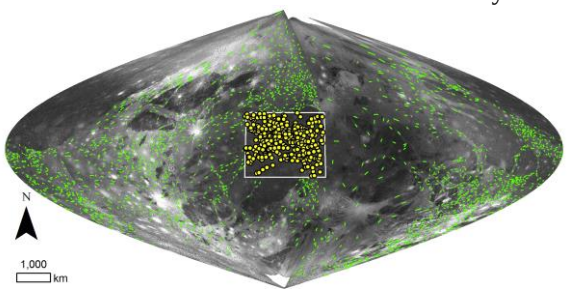

Figure 1: Global mosaic of Ganymede from Voyager and Galileo images with nominal resolution of 500 m/px. Sinusoidal projection centered on our study area (white square). In green are highlighted the representative segments of the grooves and in yellow their barycentre used for fractal clustering (modified from [10]).

comprised between 10°N-9°S and 10°E-50°E, barely corresponding to a region that presents pervasive fracturing. Here grabens containing grooves and furrows appear to be mutually intersected and randomly oriented. In addition, their distribution and orientation seem not to be influenced by larger light albedo lanes or regional-scale tectonism.

On the Ganymede Geologic map [10] these grooved graben were mapped considering their borders and their barycentre and representative segment highlight the azimuth of the grooves. According to [11] where it is demonstrated that in a volcanic environment the barycentre of a fracture is the locus where fluid expulsion is greater, we considered the barycenters of the graben segments as a representative point for cryovolcanic material emplacement that created light albedo material resurfacing.

2. Grooves fractal clustering

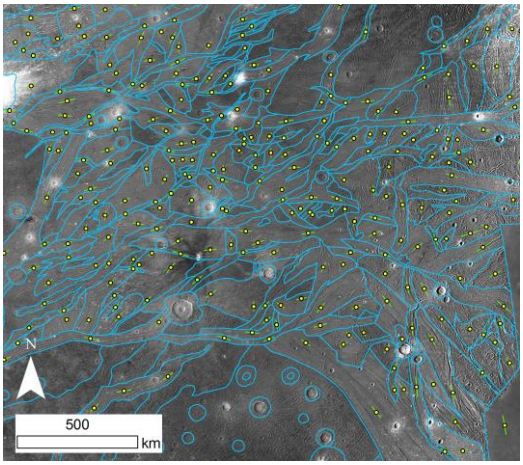

Figure 2: detail of the study area. In blue are highlighted the geologic contacts and the borders of the light albedo material. In green the representative segments of the grooves and in yellow their barycentre. (Modified from [10])

We collected the barycenter of 292 grooves and, assuming that fluids exploited grooves to move upward, we analyzed their spatial clustering. Such an approach has been used on Earth for volcanic vents (e.g. [12] and reference therein), and mud volcanoes [13]. The methodology has been successfully applied also to vent in Martian volcanoes [14] to investigate the plumbing system deep structure.

Basically, the correlation between emission point distribution and the properties of a fracture network is such that their spatial distribution may be studied in terms of self-similar (fractal) clustering [12]. A two-point correlation function method is used to measure the fractal dimension of the point population. For a population of N points the correlation integral C(l) is defined as the correlation sum that accounts for all the points at a distance of less than a given length l (e.g. Mazzarini and Isola, 2010 and reference therein). In this approach, the term C(l) is the number of pairs of points whose distance is less than l. The fractal distribution of C(l) is defined by $C(l)= cl^D$, where c is a normalization constant and D is the fractal exponent. This relationship holds within a defined range of lengths (the size range). The size range is bounded by a lower (Lco) and an upper (Uco) cutoff. [12] proposed and verified that the upper cutoff value would scale as the distance between the reservoirs at depth and the surface.

The analyzed population has an average Nearest Neighbor Distance (NND) of about 65 km and shows a fractal clustering with fractal intensity $c= 4x10^{-13}$, a fractal exponent D=2.0673 and a Lco= 75 km and Uco= 250 km. The error in estimating the cutoffs is of 10-20%. We thus forward an estimate for the depth of the reservoirs in the range 200-300 km.

3. Conclusions

For the first time we attempted to apply a fractal clustering method to the grooved terrain on Ganymede in order to obtain more information on the possible spatial relationships between the tectonic framework and the source of the cryovolcanic brines that likely contribute to the resurfacing. The analyzed population of structures show a fractal clustering spatial distribution that rule the possibility for cyovolcanic material to reach the satellite's surface. With this method we obtained an estimated depth of the fluid source in the 200-300 km range. We thus were able to confirm with an independent method the values of ocean depth obtained by studying the variability of auroras that locate the buried ocean at 150-250 km of depth below the icy crust [8].

Acknowledgements

This research was supported by: the Italian Space Agency (ASI) through the ASI-INAF agreement no.2013-056-RO.

References:[1] Kivelson, M.G. et al., 1996. *Nature*, 384, 537-541. [2] Anderson, J.D. et al., 1996 *Nature*, 384, 541-543. [3] Kivelson, M.G. et al., 2002, *Icarus*, 157, 507-522. [4] Sohl, F., et al. 2002. *Icarus*, 157, 104-119. [5] Hussmann, H. et al., 2006. *Icarus*, 185, 258-273. [6] Rambaux, N., et al., 2011, *A&A*, 527. [7] Vance, S. et al., 2014. *PSS*, 96, 62-70. [8] Saur, J. et al., 2015. *JGR Space Physics*, 120, 1715-1737. [9] Head, et al., 2002. *GRL*, volume 29, 1-4. [10] Collins, G.C., et al., 2013. Global geologic map of Ganymede: U.S. Geological Survey Scientific Investigations Map 3237. [11] Mazzarini, F., 2004, *Geophysical Research Letters*, v. 31. [12] Mazzarini, F., and I. Isola, 2010. *Geosphere*, 6, 567–582. [13] Bonini, M., and F. Mazzarini, 2010. Tectonophysics, 494, 32–47. [14] Pozzobon, R. et al., 2014. *Geological Society, London, Special Publications.*

EPSC Abstracts
Vol. 10, EPSC2015-709, 2015
European Planetary Science Congress 2015

Inner edge of the Jupiter equatorial current disk and the main auroral oval position

Igor I. Alexeev (1), Elena S. Belenkaya (1), Vladimir V. Kalegaev (1) and Aleksandr S. Lavrukhin (1, 2)

(1) Scobeltsyn Institute of Nuclear Physics M.V. Lomonosov Moscow State University, Moscow, 119992, Russia (alexeev@dec1.sinp.msu.ru)

(2) Department of Physics, M.V. Lomonosov Moscow State University, Moscow, 119992, Russia (lavrukhin@physics.msu.ru/ Fax: +7-4955-939-3553)

Abstract

The equatorial magnetodisk is one of the main contributors to the Jovian magnetospheric magnetic field. The magnetic moment of this current disk, as pointed out in [1], can be by 3 times more than planetary dipole magnetic moment. As a result, the Jupiter magnetospheric size is about 1.6 times bigger than that for the dipole case (80 R_J and 50 R_J, correspondingly). Magnetodisk is also connected with the other Jovian phenomenon, main auroral oval. The Jupiter main oval is placed in the region, where strong field-aligned currents (FACs) flow. To study magnetospheric projection of the main oval we will discuss the relative positions of the FAC, of the region where the rigid corotation of the magnetospheric plasma violates, the Alfvenic radius, and the inner edge of the equatorial azimuthal current disk position [2-6]. It will be demonstrated that the inner edge of the disk current is placed not at the Io orbit, but close to the Ganymede orbit. In this region the poloidal and toroid current systems are connected to each other. This conclusion is also supported by the Hubble aurora images, in which the Ganymede auroral spot is placed close to the main oval, sometime inside (poleward) and sometime outside (equatorward) of it.

1. Main auroral oval and equatorial current disk

The Alfven radius is a distance where the magnetic energy density is equal to the kinetic energy density, or rotation linear velocity equals to the Alfven velocity. In the other words, the Alfven radius is a radial distance, where transfer from the magnetic dominated magnetospheric region (beta<1) to the plasma dominated magnetospheric region (beta>1) takes place. This distance is critical for formation of the global magnetospheric current system in the Jovian magnetosphere [1]. In relation to incoming start of the Juno mission to the Jupiter system, the relationship between Alfven radius and the inner edge of the equatorial current disk will be discussed. The Ganymede magnetosphere is placed inside the equatorial Io plasma sheet and is formed as a result of the Ganymede magnetic field interaction with the Jovian magnetized magnetospheric plasma, which rigidly corotates with the Jupiter. We discuss the relative positions of the Ganymede orbit and the inner edge of the equatorial current disk, of the equatorial projection of the Jovian main auroral oval, and of the distance, where the rigid corotation is violated. The structure of Ganymede magnetosphere forming in the close vicinity of FAC region will be also considered. The position of the Ganymede relative to the strong FAC region (relative to the main oval magnetospheric projection) can be a reason of the Ganymede magnetosphere and Ganymede aurora dynamics. For mapping of the polar Jupiter region to the equatorial magnetospheric plane we use the paraboloid model of the Jovian magnetosphere. To estimate the errors of the analytical magnetic field model, we analyze the auroral spots, which are connected with the Ganymede and other Galileo moons. Because most of the existing magnetometer data are obtained near the equatorial plane (Galileo mission, and Pioneers and Voyagers flybys), the moon spots position [2, 5] present an unique possibility for the magnetic field mapping test.

2. Summary and Conclusions

We study the mapping of the Jupiter's main oval to the magnetospheric equatorial plane. The inner edge

of the equatorial current disk and the region of strong FACs (near the Ganymede orbit) are possible candidates. Accurate mappings of the Io and Ganymede orbits to the Jovian atmosphere in terms of paraboloid model during selected events shows that main oval is the rather projection of the inner edge of the magnetodisk that locates near the Ganymede orbit. The auroral spots at the Jupiter upper ionospheric level gives us a marker for the mapping of the main oval to the equatorial plane which is independent of the magnetic field model.

Acknowledgements

This presentation have been prepared with partial support by the FP 7 EU project "Integrated Medium for Planetary Exploration" (IMPEx), the project № 262863.

References

[1] Alexeev, I. I., E. S. Belenkaya: Modeling of the Jovian Magnetosphere, Annal. Geophys., 23, No 3, 809-826, 2005.

[2] Badman, Sarah V., Graziella Branduardi-Raymont, Marina Galand, Sébastien L.G. Hess, Norbert Krupp, Laurent Lamy, Henrik Melin, Chihiro Tao, Auroral Processes at the Giant Planets: Energy Deposition, Emission Mechanisms, Morphology and Spectra, Space Sci Rev, 187, 99–179, 2015.

[3] Belenkaya, E. M. Khodachenko: Accretion and Current Discs Controlled by Strong Magnetic Field, International Journal of Astronomy and Astrophysics, 2, 81-96, 2012.

[4] Belenkaya, E.S., S.Y. Bobrovnikov, I.I. Alexeev, V.V. Kalegaev, and S.W.H. Cowley: A model of Jupiter's magnetospheric magnetic field with variable magnetopause flaring, Planet. Space Sci., 53, 863-872, 2005.

[5] Belenkaya, Elena S., Khodachenko, Maxim L., Alexeev Igor I.: Alfvén Radius: A Key Parameter for Astrophysical Magnetospheres, in: Characterizing Stellar and Exoplanetary Environments, Editors: H. Lammer, M. Khodachenko, DOI 10.1007/978-3-319-09749-7, Springer Cham Heidelberg New York Dordrecht London, 239- 249, 2015.

[6] Khodachenko M.L., Alexeev I.I., Belenkaya E.S., and Lammer H.: Magnetodisk-dominated magnetospheres of close orbit giant exoplanets, ECLA European conference in laboratory astrophysics, Eds.: C. Stehl´e, C. Joblin, L.d'Hendecourt, EAS Publications Series, 2012. V. 58. P. 233-237, DOI: 10.1051/eas/1258037.

EPSC Abstracts
Vol. 10, EPSC2015-716, 2015
European Planetary Science Congress 2015

Energetic neutral atom imaging of Ganymede and Callisto by the Particle Environment Package (PEP) on the JUICE mission

M. Wieser (1), S. Barabash (1), Y. Futaana (1)
(1) Swedish Institute of Space Physics, Kiruna, Sweden (wieser@irf.se / Fax: +46-980-79025)

Abstract

Co-rotating plasma is constantly precipitating on the surface of the Jovian moons where not hindered by magnetic fields to do so. Ions reaching the surface are sputtering the surface and are themselves partially backscattered. Both processes result in energetic neutral atoms that will be observed by the Particle Environment Package (PEP) while in orbit around Ganymede or during flybys at Callisto.

1. Introduction

One of the six sensors of the Particle Environment Package (PEP) onboard JUICE is the Jovian Neutrals Analyzer (JNA). JNA is based on the successful energetic neutral atom (ENA) instrument flown on the Indian Chandrayaan-1 mission to the moon [1] and the ENA instrument on board of Mercury Magnetospheric Orbiter of the BepiColombo mission. JNA measures energetic neutral atoms (ENAs) energy, mass and angular resolved in the energy range from 10eV to 3.3keV with an angular resolution of 7° x 14.5°. JNA will map the energetic neutral atom emissions in the energy range from 10eV to 3.3 keV from Ganymede and Callisto allowing to infer plasma precipitation patterns at the surface of these moons. We present simulations of expected energetic neutral atom observations at Ganymede and Callisto based on laboratory experiments of ions impinging on water ice surfaces under Ganymede surface -like conditions.

2. Ice scattering experiments

Ions in the keV energy range impinging on icy surfaces of Ganymede and Callisto result in the production of sputtered and backscattered energetic neutral atoms. We characterized these processes in laboratory experiments mimicking Ganymede surface conditions (Figure 1). We obtained species resolved energy spectra and total yields of energetic neutral atoms emitted from ice for incident proton and oxygen ions up to 33keV/q energy.

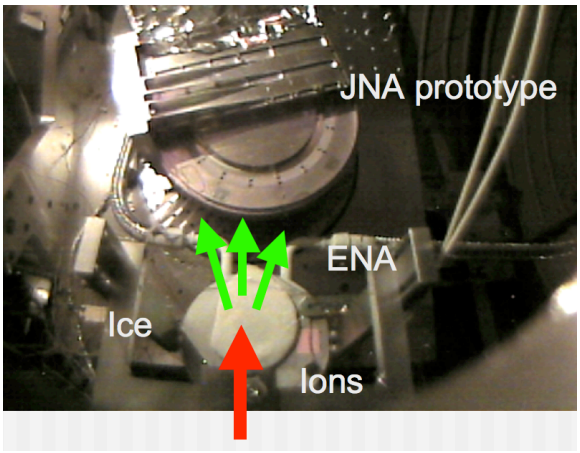

Figure 1: Setup for laboratory ice scattering experiment under Ganymede surface like conditions.

3. ENA emission maps

We combine models predicting the precipitating plasma flux onto the surface with the data from our laboratory experiment and the expected performance of the JNA sensor to obtain energetic neutral atom emission maps from Ganymede (Figure 2) and Callisto, as they will be observed by the JNA sensor.

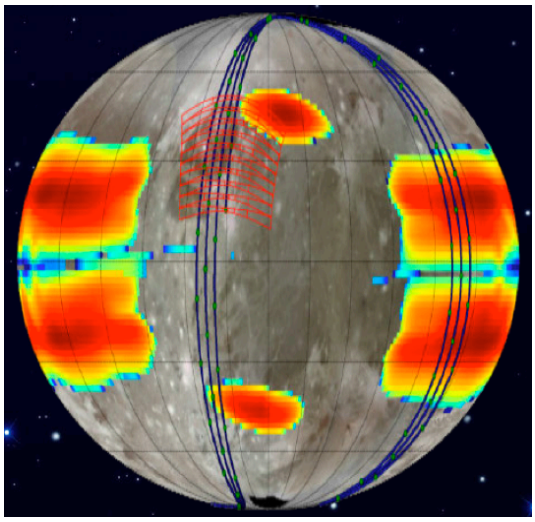

Figure 2: Simulated ENA emission map of Ganymede with superimposed orbit ground tracks and JNA field of view.

4. Summary

Energetic neutral atoms provide way to remotely investigate the plasma fluxes at the surface of Ganymede and Callisto. Models combined with laboratory experiments show that despite the harsh Jovian radiation environment, mapping of the precipitating plasma fluxes onto Ganymede and Callisto is possible using energetic neutral atom imaging.

References

[1] S. Barabash, A., et. al.. Current Science, 96(4):526–532, 2009.

EPSC Abstracts
Vol. 10, EPSC2015-732, 2015
European Planetary Science Congress 2015

Autumn at Titan's South Pole: The 220 cm^{-1} Cloud

D. E. Jennings (1), V. Cottini (1, 2), R. K. Achterberg (1,2), C. M. Anderson (1), F. M. Flasar (1), R. de Kok (3, 4), N. A. Teanby (5), A. Coustenis (6), S. Vinatier (6)
(1) Goddard Space Flight Center, Greenbelt, MD 20771, USA, (2) Department of Astronomy, University of Maryland, College Park, MD 20742, USA, (3) SRON Netherlands Institute for Space Research, Sorbonnelaan 2, 3584 CA Utrecht, The Netherlands, (4) Leiden Observatory, Leiden University, Postbus 9513, 2300 RA, Leiden, The Netherlands, (5) School of Earth Sciences, University of Bristol, Bristol BS8 1RJ, UK, (6) Laboratoire d'Etudes Spatiales et d'Instrumentation en Astrophysique (LESIA), Observatoire de Paris, CNRS, UPMC Univ. Paris 06, Univ. Paris-Diderot, 5, place Jules Janssen, 92195 Meudon Cedex, France. (donald.e.jennings@nasa.gov)

Abstract

Beginning in 2012 an atmospheric cloud known by its far-infrared emission has formed rapidly at Titan's South Pole [1, 2]. The build-up of this condensate is a result of deepening temperatures and a gathering of gases as Winter approaches. Emission from the cloud in the south has been doubling each year since 2012, in contrast to the north where it has halved every 3.8 years since 2004. The morphology of the cloud in the south is quite different from that in the north. In the north, the cloud has extended over the whole polar region beyond 55 N, whereas in the south the cloud has been confined to within about 10 degrees of the pole. The cloud in the north has had the form of a uniform hood, whereas the southern cloud has been much more complex. A map from December 2014, recorded by the Composite Infrared Spectrometer (CIRS) on Cassini, showed the 220 cm^{-1} emission coming from a distinct ring with a maximum at about 80 S. In contrast, emissions from the gases HC_3N, C_4H_2 and C_6H_6 peaked near the pole and had a ring at 70 S. The 220 cm^{-1} ring at 80 S coincided with the minimum in the gas emission pattern. The 80 S condensate ring encompassed the vortex cloud seen by the Cassini Imaging Science Subsystem (ISS) and Visible and Infrared Mapping Spectrometer (VIMS) [3, 4]. Both the 220 cm^{-1} ring and the gas "bull's-eye" pattern were centered on a point that was shifted from the geographic South Pole by 4 degrees in the direction of the Sun. This corresponds to the overall tilt of Titan's atmosphere discovered from temperature maps early in the Cassini mission by Achterberg et al. [5]. The tilt may be reinforced by the presumably twice-yearly (north and south) spin-up of the atmosphere at the autumnal pole.

The bull's-eye pattern of the gas emissions can be explained by the retrieved abundance distributions, which are maximum near the pole and decrease sharply toward lower latitudes, together with temperatures that are minimum at the pole and increase toward lower latitudes. The increasing temperatures overcome the decreasing gas abundances to produce emission in the narrow range around 70 S. This cannot, however, explain the maximum of emission at 80 S from the condensate ring. The coincidence at 80 S of the 220 cm^{-1} peak with the gas emission minimum may indicate where the condensation is taking place. The central, polar minimum in the cloud emission may be due to faster rain-out and smaller extinction cross-sections. Spectral maps from 2013-15 [6] show that the gas emission pattern has been evolving quickly, with noticeable changes from one flyby to the next (about one month). The bull's-eye structure appears to have been most prominent in early 2014 and by late 2014 the pattern was becoming more uniform. As Titan progresses through late southern Autumn we expect the morphology of the condensate cloud to take on a hood-like distribution similar to that in the north.

References:
1. Jennings, D. E., et al., ApJ, 754, L3, 2012.
2. Jennings, D. E., et al., ApJ Lett., in press.
3. West, R. A., et al., DOI 10.1016/j.icarus.2014.11.038, 2014.
4. de Kok, R. et al., Nature, 514, 65, 2014.
5. Achterberg, R. K., et al., Icarus, 197, 549, 2008.
6. Coustenis, A., et al., Icarus, submitted 2014.

EPSC Abstracts
Vol. 10, EPSC2015-771-1, 2015
European Planetary Science Congress 2015

Realistic ice sputtering experiments for the surfaces of Galilean moons

A. Galli (1), A. Pommerol (1), P. Wurz (1), B. Jost (1), J.A. Scheer (1), A. Vorburger (1,2), M. Tulej (1), N. Thomas (1), M. Wieser (3), and S. Barabash (3)
(1) Physikalisches Institut, University of Bern, Bern, Switzerland (andre.galli@space.unibe.ch), (2) Division of Physical Sciences, American Museum of Natural History, New York, USA, (3) Swedish Institute of Space Physics, Kiruna, Sweden

Abstract

We use an existing laboratory facility for space hardware calibration in vacuum to study the impact of energetic ions on water ice. The experiment is intended to simulate the conditions on the surface of Jupiter's icy moons. The first results of hydrogen, oxygen, and sulphur ions sputtering a sample of porous salty ice confirmed extrapolations from previous sputtering experiments obtained at different impact angles for non-porous water ice [3]. Here, we present additional measurements for a larger range of ion impact angles and different ice samples.

1. Introduction

The vast majority of celestial objects in the outer solar system are bodies with ice-rich surfaces. This includes icy moons like Europa, Ganymede, Callisto, Enceladus, and Triton, but also the Trans-Neptunian Objects and comets. The surface of these objects directly interacts with the space environment, resulting in sputtering, radiolysis, and sublimation. These processes lead to a tenuous, surface-bound atmosphere. Properties of ices at low pressures and temperatures, such as the sputtering efficiency due to ion bombardment, are difficult to predict theoretically and are not better constrained than one order of magnitude from laboratory experiments [5]. This limits the predictive capability of any surface and atmosphere model. The JUICE mission [1], scheduled to visit Europa, Ganymede, and Callisto in the years 2030–2032, will allow to directly sample the particles ejected from the surface and also to observe the atmosphere at infrared, visible, and ultraviolet wavelengths. The instruments' design would greatly benefit from better constrained parameters for surface release processes. For this purpose we use a facility at the University of Bern, Switzerland, to simulate ion sputtering processes on icy surfaces in vacuum.

2. Experiment set-up

In contrast to most previous ice sputtering experiments [2], we shoot ions at a 1 cm thick sample of porous water ice to simulate the regolith on the surface of an icy moon. This approach allows us to produce samples with chemical impurities and to study the impact of porosity on release processes. The experiments are performed in the MEFISTO test facility, which consists of a vacuum chamber and an electron-cyclotron-resonance ion source [4]. The ice samples are prepared with the technique described by [6]: we use an ultrasonic nebulizer to produce micrometer-sized droplets of salty water, which are then frozen to a porous sample of ice grains. The density of the ice sample ranges between 200 and 300 kg m^{-3}, corresponding to an average porosity of 0.75.
During experiments, the ice sample holder is mounted on a steel plate cooled with liquid nitrogen (see Fig. 1). The ice temperature of 90 K and the pressure in the vacuum chamber (10^{-7} mbar) are representative for conditions on the surface of Europa.

3. Results

We measured sputtering yields for singly charged hydrogen, oxygen, and sulphur ions, which are most relevant for the Jupiter system [7]. For sulphur, these are the first experimental data ever obtained. The first series of results were obtained for a very flat ion incidence angle of 15° (see Fig. 1) and at energies between 1 and 30 keV. The results at these settings agree with the predictions by Famá et al. 2008 [2]; the sputtering yield is indiscernible from the one for oxygen ions. Since the sputtering yields are consistent with previous laboratory measurements with compact ice layers on a microbalance, this implies that sputtering from porous water ice is similar to that from a dense sample. The particles ejected from the ice surface are purely molecular water. The relative abundance of ra-

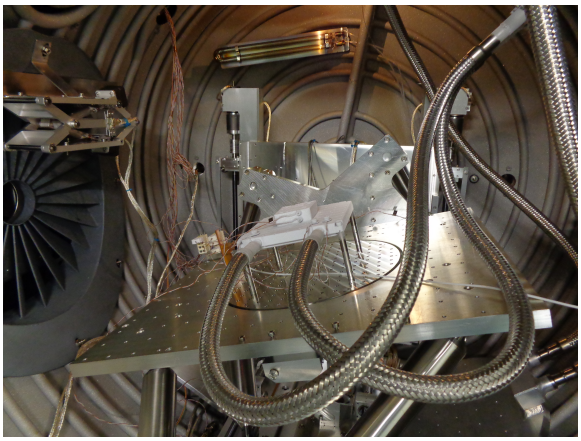

Figure 1: Picture of ice sample in MEFISTO vacuum chamber at the end of a sputtering experiment. The ion beam exiting the fan-shaped structure to the left hits the ice sample at a flat angle (15° by default).

diolysis products, such as molecular hydrogen or oxygen, is smaller than 2 % at our ice temperatures. Currently, surface charging of the ice sample due to the ion beam limits the number of unbiased sputter yield measurements per experiment [8]. An irradiated area of ice takes several hours to completely discharge, which is consistent with the permittivity of dry snow.

4. Conclusions

The MEFISTO facility can be used to study ion sputtering relevant for the icy moons of Jupiter. The first measured sputtering yields at shallow ion incidence angles followed theoretical extrapolations for a smooth surface [3]. We disentangle the potential effects of porosity and surface roughness on the sputtering yield with new experiments by increasing the ion incidence angle and by generating ice samples with much larger grains. The electron-cyclotron-resonance ion source also allows us to generate a beam of multiply charged ions to check if the sputtering yield depends on the charge state. Measures to limit the surface charging of the porous ice during ion sputtering are investigated to increase the number of data points per experiment.

Acknowledgements

The work by André Galli and Antoine Pommerol at the University of Bern has been supported by the Swiss National Science Foundation. The work in this study has been partially performed in the context of the activities of the ISSI International Team #322, www.issibern.ch/teams/exospherejuice/

References

[1] ESA: JUpiter ICy moons Explorer – Exploring the emergence of habitable worlds around gas giants – Definition Study Report, ESA/SRE(2014)1, September 2014, http://sci.esa.int/juice/54994-juice-definition-study-report.

[2] Famá, M., Shi, J., and Baragiola, R.A.: Sputtering of ice by low-energy ions, Surface Science 602, 156, 2008.

[3] Galli, A. et al.: Experimental study of surface erosion processes of the icy moons of Jupiter, Icarus, submitted, 2015.

[4] Hohl, M., Wurz, P., and Bochsler, P.: Investigation of the density and temperature of electrons in a compact 2.45 GHz electron cyclotron resonance ion source plasma by x-ray measurements, Plasma Sources Science and Technology 14, 692–699, 2005.

[5] Johnson, R.E. et al.: Radiation effects on the surfaces of the Galilean satellites, in: Bagenal, F. (Ed.), Jupiter: Atmosphere, Satellites and Magnetosphere. University of Arizona Press, Tucson, 2004.

[6] Jost, B. et al.: Experimental characterization of the opposition surge in fine-grained water-ice and high albedo analogs, Icarus, submitted, 2014.

[7] Paranicas, C. et al.: The ion environment near Europa and its role in surface energetics, Geophysical Research Letters 29, 18, 2002.

[8] Shi, J. et al.: Ion-induced electrostatic charging of ice at 15–160 K, Physical Review B 85, 035424, 2012.

EPSC Abstracts
Vol. 10, EPSC2015-784, 2015
European Planetary Science Congress 2015

Modelling of NIM/PEP/JUICE measurements of Callisto's ice-sputtered exosphere

Audrey Vorburger (1, 2), Peter Wurz (2), André Galli (2), Olivier Mousis (3), Stas Barabash (4), Helmut Lammer (5)
(1) Dept. of Earth and Planetary Sciences, Division of Physical Sciences, American Museum of Natural History, New York, USA (**avorburger@space.unibe.ch**), (2) Physikalisches Institut, University of Bern, Bern, Switzerland, (3) Aix Marseille Université, CNRS, Laboratoire d'Astrophysique de Marseille UMR 7326, 13388, Marseille , France, (4) Swedish Institute of Space Physics, S-981 28 Kiruna, Sweden, (5) Austrian Academy of Sciences, A-8042 Graz, Austria

Abstract

The JUpiter ICy moons Explorer (JUICE) mission [1], which is currently in implementation by the European Space Agency (ESA), is intended for the detailed investigation of the giant gaseous planet Jupiter and its three largest moons, Ganymede, Callisto and Europa. The Particle Environment Package (PEP), part of JUICE's science payload, contains 6 sensors for comprehensive in situ measurements of electrons, ions and neutrals found in the Galilean moons' vicinity [2]. One of the suite's sensors, the Neutral and Ion Mass spectrometer (NIM), will measure the neutral and ion composition of the exospheres of the three satellites during flybys and in orbit.

Whereas Callisto's surface has been mapped as early as in 1980 by the two Voyager missions, still little is known today about the nature of its atmosphere, due to its tenuousness also called exosphere. It is assumed that Callisto is not fully differentiated and that its surface composition consists of about half ice and half mineral contents [3]. Thus, composition measurements at Callisto offer the unique opportunity to measure the full spectrum of building blocks of the Jupiter system.

We present here modelled density profiles of Callisto's ice-sputtered exosphere based on new laboratory measurements of ice sputtering. The sputtering measurements were conducted in our laboratory on a sample of dense and porous salty ice, specifically manufactured to simulate sputtering of the Galilean moons' icy surfaces.

1. JUICE – PEP / NIM

The Neutral Ion Mass Spectrometer (NIM), one of the instruments of the Particle Environment Package (PEP), will conduct the first-ever direct sampling of the exospheres of Europa, Ganymede, and Callisto. NIM is capable of detecting exospheric neutral gas and thermal plasma at the Galilean moons with very high mass resolution and unprecedented sensitivity. The mass resolution is $M/\Delta M > 1100$ in the mass range 1–1000 amu and NIM's energy range is ≤ 5e V for neutrals and <10 eV for ions. The detection level for neutral gas is $1 \cdot 10^{-16}$ mbar for a 5-second accumulation time, which corresponds to a particle density of about 1 cm^{-3}. With such a detection limit, NIM will be capable of recording mass spectra during the satellites' flybys starting at 10^5 km altitude. NIM will thus during a single flyby record more than 1000 mass spectra with varying integration time, covering several hours of measurements.

2. Callisto's ice-surface composition

The surface of Callisto consists to about 50 % of an icy component. For this surface we implement two different composition models that find analogues in the initial gas phase conditions of the solar nebula: One composition represents the oxidizing state and the other represents the reducing states of the gas [4, 5]. The density curves we simulate incorporate first experimental results from a facility at the University of Bern used to simulate ion sputtering on the surface of the icy moons of Jupiter [6]. These experiments provide us with new, improved sputtering yields, which we can use to simulate ab initio density curves.

3. Monte Carlo simulation of Callisto's ice-sputtered exosphere

We present density profiles for all species present on Callisto's icy surface, as computed by our Monte-Carlo Model. The Monte-Carlo model used is an updated version of the model first presented in [7].

In this model, the trajectory of each individual particle is simulated from its point of origin until it either overcomes the parent body's gravitational attraction or changes its nature. As source processes we consider: 1) surface sublimation, 2) sputtering, and 3) photon-stimulated desorption, with emphasis on ice-sputtering. Particles are lost by one of the following sink mechanisms: 1) escape, 2) ionization, 3) fragmentation, or 4) surface adsorption. We ran 10^5 trajectories for each species.

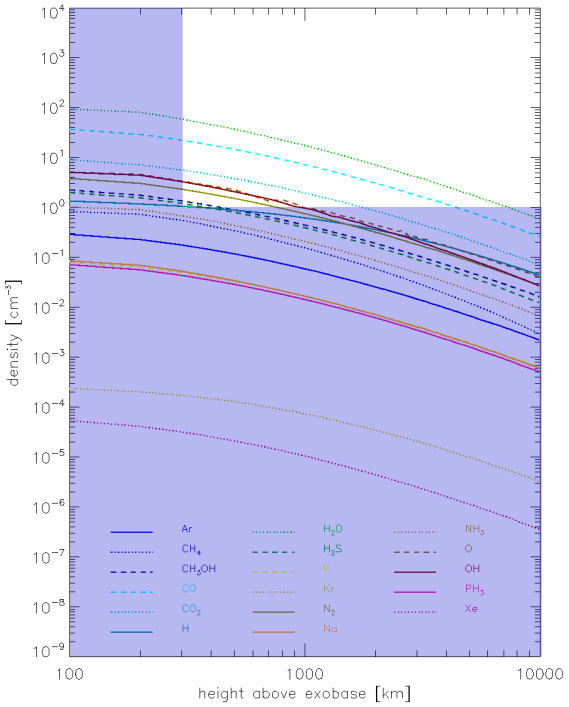

Figure 1: Example density profiles for the major constituents sputtered from the icy surface. Shown in blue is the minimal altitude reached by JUICE and NIM's nominal background.

4. NIM Simulations

In addition to the simulated density profiles, we also present mass spectra as we expect NIM to measure during the Callisto flybys based on the newest JUICE trajectory. Our mass spectra plots show that as far as 10^5 km above the surface, NIM is capable of detecting a signal from the most abundant species above its background level. The closer JUICE approaches the moon, the more species, and, notably, species released from the surface through different release processes will be detected by NIM. At closest approach, a single mass spectrum recorded during a time interval of 5s will exhibit mass peaks for almost all species released thermally and most species released by ion sputtering from the icy surface.

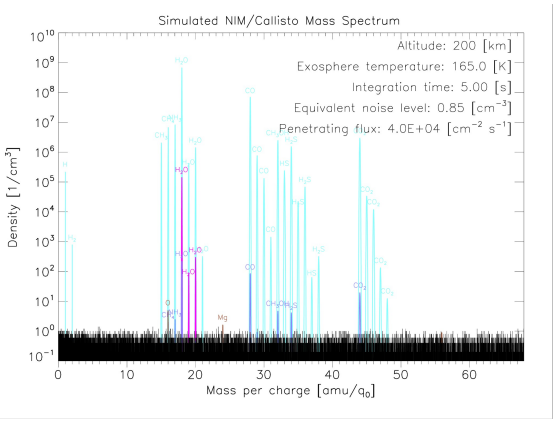

Figure 2: Example mass spectrum as expected to be recorded by NIM during closest approach (200 km) of Callisto. Cyan denotes sublimated, blue denotes ice-sputtered, brown denotes mineral-sputtered, and magenta denotes photo-desorbed species.

4. Discussion and Conclusion

The density profiles of the ice sputtered species start at rather low values (compared to their sublimated counterparts), but have smaller scale heights, due to their higher temperatures and eject velocities. In fact, the most abundant species are detectable to NIM starting at Callisto's Hill radius (~10^5 km). Since the JUICE flybys are as low as 200 km above Callisto's surface, NIM is expected to measure most of the sputtered particle populations. Our calculations show that NIM's sensitivity is high enough to allow the detection of particles sputtered from the icy as well as the rocky surfaces, and to distinguish between different composition models, mainly by observing the presence or absence of CO and CO_2 and by determining the N_2 to NH_3 ratio.

References

[1] Grasset, O., et al. (2013), Planet. Space Sci., 2013.

[2] Barabash, S., et al (2013), EPSC 2013

[3] Nagel, K., et al (2004), Icarus, 169.

[4] Johnson, T. V., et al. (2012), Astron. Astrophys., 757.

[5] Mousis, O., et al. (2012), The Astro. J. Letters, 751.

[6] Galli, A., et al. (2015), Icarus, submitted.

[7] Wurz, P., and H. Lammer (2003), Icarus, 164.

EPSC Abstracts
Vol. 10, EPSC2015-792, 2015
European Planetary Science Congress 2015

Saturn's Magnetosphere: Sub-corotation and Magnetosphere-Ionosphere Interaction

E.J.Smith(1) and M.K.Dougherty (2)
(1) Earth and Space Sciences, Jet Propulsion Laboratory, Pasadena, CA, 91109, USA (Edward.J.Smith@jpl.nasa.gov), (2) Space and Atmospheric Physics, Imperial College, London, ,United Kingdom (m.dougherty@imperial.ac.uk)

Our investigation using Cassini measurements of the azimuthal magnetospheric field component, B_Φ, has two complementary objectives. First, to test the validity of the model, introduced by Hill(1973) for Jupiter and modified by Cowley and Bunce (2003) to apply to Saturn, based on the outflow of plasma from the inner magnetosphere (Enceladus) and the interaction between the ionosphere and sub-corotating magnetosphere. Second, to replace assumed model parameters with values obtained from observation. We test the model quantitatively using the equation relating the ionospheric Pedersen current, I_P, the height- integrated Pedersen conductivity, Σ_P, the rotation rate of the neutral atmosphere, Ω_S^*, the Saturn Kilometric Rotation (SKR) rate of the magnetic field, Ω_S, the rotation rate of the magnetospheric field, ω, and G, a parameter dependent on the ionospheric co-latitude, θ_i, and the ionospheric magnetic field vector, B_i. The B_Φ measurements and Ampere's law are used to derive, I_P, as a function of θ_i. This analysis has so far been restricted to part of 13 identical Cassini orbits (August through October, 2008) inside a distance ,r, of 10 Saturn radii, R_S, and the midnight local time sector, 24 +/− 2 hours. This choice suppresses spatial changes in favor of temporal/ dynamical dependences.

It is found that I_P/G is well represented by a simple exponential, A exp(-B θ_i). Important implications are (1) the rotation rate of the neutral atmosphere, Ω_S^* is equal to Ω_S, the SKR magnetic field rotation rate, (2) parameter, A = Σ_P, (3) parameter, B =1-ω/ Ω_S, (4) I_P (θ_i), corresponding to the exponential, is found from A exp(-B θ_i)x G, and (5) although, for each orbit, the exponential fit has a correlation coefficient exceeding 0.99, implying A and B are constant, A and B undergo large variations from orbit to orbit as do all the above parameters revealing a significant magnetospheric- ionospheric variability with time. These results are used to test the model and are compared with published results using a complementary approach, energetic particle and plasma measurements of $V_\Phi = \omega r$.

EPSC Abstracts
Vol. 10, EPSC2015-803, 2015
European Planetary Science Congress 2015

Enceladus' internal ocean constrained from Cassini gravity and topography data

Lefèvre, A (1), **G. Tobie** (1), G. Choblet (1), O. Cadek (2), G. Mitri (1), M. Massé (1), M. Behounkova (2); (1): Laboratoire de Planétologie et Géodynamique, Université de Nantes, CNRS, France (gabriel.tobie@univ-nantes.fr) (2) Department of Geophysics, Charles University in Prague, Czech Republic

Abstract

The intense activity at the south pole of Enceladus hints at an internal water reservoir. The detection of sodium and potassium salts (about 1%) in icy grains emanating from Enceladus' south polar faults [1] indicates that the plume source is most likely connected to a salty subsurface ocean. The recent discovery of silicon-rich particles originating from Enceladus further indicates that hydrothermal interactions is currently occurring at the base of the ocean, and that hydrothermal products are quickly transferred to the plume source [2]. Based on topography and gravity data collected by the Cassini spacecraft [3, 4], this depth of ice/ocean interface is estimated to about 30-40 km underneath the South Pole. However the depth of ocean/rock interface as well as the extension of the ocean still remains unconstrained.

In order to provide further constraints on the ocean configuration, we develop an interior structure model consisting of a rock core, an internal ocean and an ice shell, which satisfies simultaneously the observed gravity and shape data [3, 5]. Our modelling approach is comparable to the approach we used to interpret the data of Titan [6]. However, as large-amplitude deflections of the ice/ocean and ocean/rock interfaces are required to explain the data, we employ here a full (non-linearized) description of the gravity potential [e.g. 7]. By assuming that the gravity disturbance due to surface topography is compensated by ice/ocean and/or ice/rock deflection, we map the depth of the ice/ocean interface and constrain the size and shape of the rock core, thus providing constraints on the total volume and lateral extension of the internal ocean. Possible correlations with main geological units as well as implications for the thermal history of Enceladus will be discussed at the conference.

Acknowledgements

This research received funding from the European Research Council under the European Community's Seventh Framework Programme FP7/2007-2013 grant agreement 259285 and from the Région Pays de la Loire, JUPILOIRE, Connect Talent programme.

References

[1] Postberg F. et al.: A salt-water reservoir as the source of a compositionally stratified plume on Enceladus, Nature, 474, 620-622 (2011).

[2] Hsu, H-W. et al.: Ongoing hydrothermal activities within Enceladus, Nature, 519, 207-210 (2015).

[3] Iess, L. et al.: The gravity field and interior structure of Enceladus, Science, 344, 78-80 (2014).

[4] McKinnon, W. B.: Effect of Enceladus' rapid synchronous spin on interpretation of Cassini gravity, Geophys. Res. Lett., in press.

[5] Nimmo, F. et al.: Geophysical implications of the long-wavelength topography of the Saturnian satellites, J. Geophys. Res., 116, E1101 (2011).

[6] Lefevre, A. et al. Structure and dynamics of Titan's outer icy shell constrained from Cassini data, Icarus, 237, 16-28 (2014).

[7] Martinec, Z.: The density contrast at the Mohorovicic discontinuity, Geophy. J. Int., 117, 539-544 (1994).

EPSC Abstracts
Vol. 10, EPSC2015-816, 2015
European Planetary Science Congress 2015

The latest on hydrothermal activity on Enceladus from Cassini and Laboratory work

F. Postberg (1,2), H.-W. Hsu (3), Y. Sekine (4), T. Shibuya (5) and the CDA Science Team

(1) Institute of Earth Sciences, University of Heidelberg, Germany, (2) Institute of Space Systems, University of Stuttgart, Germany (3) Laboratory for Atmospheric and Space Physics, University of Colorado, Boulder, USA, (4) Department of Earth & Planetary Science, University of Tokyo, Japan, (5) Laboratory of Ocean-Earth Life Evolution Research, Agency for Marine-Earth Science and Technology, Yokosuka, Japan

(Frank.Postberg@geow.uni-heidelberg.de)

1. Introduction

Various observations from the Cassini spacecraft [1,2,3], suggest the existence of subsurface water beneath the south polar region of Saturn's geologically active icy moon Enceladus. They provide information on the composition and physical conditions of water reservoirs occurring at shallow depth from which the plumes emerge [1,2,4], and about the dimensions of the south polar ocean beneath the ice crust at a depth of about 50km [3]. However, constraints on the physical and chemical conditions at the interface of the rocky core and the deep ocean are sparse. We report in situ measurements of tiny grains, so called stream particles, by Cassini's Cosmic Dust Analyser (CDA) in the Saturnian system.

CDA data shows that these nano-particles are composed of silica that were initially embedded in larger µm-sized icy grains emitted from Enceladus subsurface waters and released by sputter erosion in Saturn's E ring. Comprehensive long-term laboratory experiments and model calculations were carried out to investigate the reaction conditions at the bottom of Enceladus' ocean.

2. Results

We found that the formation of these nano-phase silica grains requires on-going hot hydrothermal rock-water interactions at Enceladus ocean floor [5]. Measurements and experiments both point at dissolved silica concentrations at the ocean floor in the order of at least 3 mMol. The formation process is already well known from hydrothermal sites and experiments on Earth [6,7,8,9] and could be reproduced by our experiments for Enceladus conditions. Colloidal nano-silica forms upon supersaturation during cooling of the hydrothermal liquid, and travels upwards towards the near surface waters fueling the plume where the temperatures are close to 0°C. Formation and stability of a nano-colloidal silica phase requires alkaline pH (8.5 – 10.5) and only tolerates a mild salinity, not higher than a few per cent. To sustain the formation of silica nanoparticles, the composition of Enceladus' core needs to be similar to that of carbonaceous chondrites. The high-temperature reactions need to persist in order to sustain the formation of nano-silica particles, which otherwise would readily dissolve in the ocean.

Two principle scenarios are investigated: 1) A chemically closed system where hydrothermal fluid and the Enceladus ocean quickly equilibrate and the oceanic composition is dominated by water–rock reactions. 2) A chemically open system where hydrothermal fluids are in disequilibrium with the surrounding ocean as it is the case on alkaline hydrothermal fields on Earth's ocean. pH values of hydrothermal fluids in a chemically closed system increase upon cooling. To form nano-silica this would require reaction temperatures > 150°C at a rock/water interface on Enceladus' ocean floor or inside a porous core. In the case the hydrothermal sites are chemically open to the icy crust through effective volatile exchanges, pH values of fluids and ocean are not determined simply by a change in dissolved species upon cooling. In this case the pH at the hydrothermal sites might be even higher than in the surrounding cool ocean and temperatures as low as 50°C are sufficient to allow nano-silica formation. Accordingly, the formation of silica nanoparticles is most likely sustained by geologically recent or ongoing hydrothermal activity.

3. Summary and Conclusions

Our results indicate hydrothermal reactions associated with a global-scale geoactivity that transports hydrothermal products from the core-mantle boundary up to the plume. Such high temperatures imply either that Enceladus formed shortly after the formation of the solar system or that the current activity was triggered by a recent heating event. In the case of a chemically closed system (scenario 1) hydrogen production would proceed efficiently, which could provide habitable environments for chemoautotrophic life. In the case of a chemically open system (scenario 2) steep gradients, not only in temperature but also in pH and composition of dissolved species, would allow similar conditions as on alkaline hydrothermal sites on Earth (E.g., 'Lost City'). These sites do not only sustain life independent from the sun but are also considered to be good candidates where life first emerged on Earth [10].

Acknowledgements

This work is supported by DLR and DFG-Deutsche Forschungsgemeinschaft grants PO1015/3-1 and PO1015/4-1.

References

1. Postberg, F. *et al.*, Sodium salts in E-ring ice grains from an ocean below the surface of Enceladus, *Nature*, 459, 1098-1101 (2009).
2. Postberg, F., Schmidt, J., Hillier, J., Kempf, S., and Srama, R., A salt-water reservoir as the source of a compositionally stratified plume on Enceladus, *Nature*, 474, 620–622 (2011).
3. Iess, L et al., The Gravity Field and Interior Structure of Enceladus, Science, 344, 78 (2014).
4. Schmidt, J., Brilliantov, N., Spahn, F., and Kempf, S., Slow dust in Enceladus' plume from condensation and wall collisions in tiger stripe fractures, *Nature*, 451, 685-688 (2008).
5. Hsu, H.-W., Postberg, F., Sekine, Y. et al., Ongoing hydrothermal activities within Enceladus, *Nature*, 519, 207-210 (2015).
6. Icopini, G. A., Brantley, S. L., and Heaney, P. J., Kinetics of silica oligomerization and nanocolloid formation as a function of pH and ionic strength at 25°C, *Geochim. Cosmochim. Acta*, 69, 293-303 (2005).
7. Conrad. C. F. *et al.*, Modeling the kinetics of silica nanocolloid formation and precipitation in geologically relevant aqueous solutions, *Geochim. Cosmochim. Acta*, 71, 531-542 (2007).
8. Tobler, D. J., Shaw, S., and Benning, L. G., Quantification of initial steps of nucleation and growth of silica nanoparticles: An in-situ SAXS and DLS study, *Geochim. Cosmochim. Acta*, 73, 5377-5393 (2009).
9. Tobler, D. J. and Benning, L. G., In situ and time resolved nucleation and growth of silica nanoparticles forming under simulated geothermal conditions, *Geochim. Cosmochim. Acta*, 114, 156-168 (2013).
10. Martin, W. F., Sousa, F. L., Lane,, N. Energy at life's origin. *Science*, 344, 1092 – 1093 (2014).

EPSC Abstracts
Vol. 10, EPSC2015-834-1, 2015
European Planetary Science Congress 2015

Tidal resonance in icy satellites with subsurface oceans

S. Kamata (1), I. Matsuyama (2), and F. Nimmo (3)
(1) Hokkaido University, Japan, (2) University of Arizona, USA, (3) University of California, Santa Cruz, USA
(kamata@mail.sci.hokudai.ac.jp / +81-11-706-3566)

Abstract

We extend the formulation for tidal deformation based on viscoelasto-gravitational theory to incorporate inertial effects. Although ocean dynamics is treated in a simplified fashion, we find a resonant configuration when the phase velocity of ocean gravity waves is similar to the orbital velocity. A static ocean formulation gives an accurate result only if the ocean thickness is larger than the resonant thickness by a factor of about one hundred, of order 10 km. The resonant configuration strongly depends on the properties of the shell, demonstrating the importance of the presence of a shell on tidal dissipation.

1. Introduction

Tidal dissipation is one of the major heat sources for the evolution of planetary bodies, particularly the satellites of the giant planets. Based on internal thermal and structural modeling, icy satellites of Jupiter and of Saturn are expected to possess an internal ocean underneath an icy shell. Pluto may also possess a subsurface ocean, and tidal dissipation due to the orbital motion of its satellite, Charon, may have heated Pluto in the past. Thus, a detailed investigation of the evolution of planetary bodies in the outer Solar System should consider tidal dissipation using an interior model consisting of an outer solid layer, internal liquid layer(s), and a solid (or liquid) core.

Previous studies of tidal dissipation in icy satellites using spherically-symmetric models can be classified into two types: those considering tidal dissipation in the solid part, and those considering tidal dissipation in the ocean. The former type has been applied to many satellites and planets [e.g., 1], though the effect of an internal liquid layer on tidal deformation has usually been treated in a simplified fashion. On the other hand, the latter type considers ocean dynamics [e.g., 2]. One important assumption in the latter models is that the surface topography follows an equipotential surface. This requires either that the ocean is at the surface or that the ice shell overlying the ocean is soft. In reality, none of the icy satellites has a surface ocean, and in some cases (such as Titan) the ice shell may not be sufficiently soft because the viscosity of ice is very high at low temperatures.

In this study, we extend the viscoelasto-gravitational theory and obtain a comprehensive equation system that can account for a thin subsurface ocean in viscoelastic planets (and satellites). We then apply our theory to icy satellites and investigate the effect of an icy shell on the resonant configuration.

2. Theory

Our formulation is based on the well-established elasto-gravitational theory considering deformation of a spherically symmetric, non-rotating, elastic, and isotropic body. In this theory, three equations (i.e., the equation of momentum conservation, the Poisson equation for the gravitational field, and the constitutive equation) are solved applying the spherical harmonic expansion. If we include and exclude the inertial term in the equation of momentum conservation, we obtain four- and two-component equation systems for a liquid layer, respectively. The latter equation system has been widely used in previous studies. In the following, we call the formulation using the four-component equation system a dynamic formulation while the two-component system a static formulation.

3. Tidal resonance

We first investigate the inertial effects using a five-layer Ganymede model [3]. Figure 1 shows the real part of the tidal Love number h_2 as a function of ocean thickness, $H_{\rm ocean}$. This figure clearly shows that our dynamic formulation leads to a resonance when $H_{\rm ocean} \sim 0.1$ km. We found that this thickness is close to the thickness that results in a phase velocity of gravity waves ($\approx \sqrt{gH_{\rm ocean}}$, g is gravitational acceleration) similar to the orbital velocity ($= \omega_{\rm orb}/k$, k is wavenumber). For this Ganymede

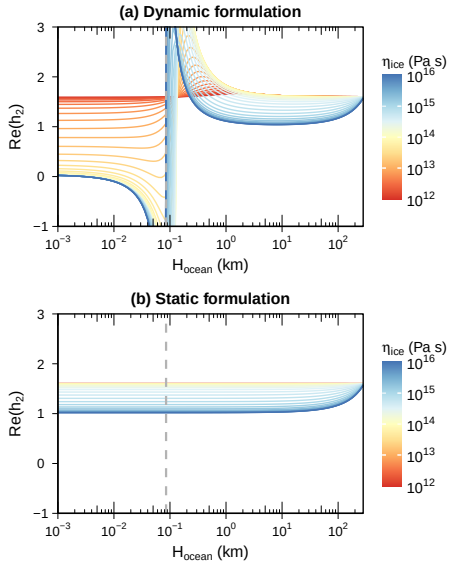

Figure 1: Real part of h_2 as a function of ocean thickness for a Ganymede model. The vertical dashed lines indicate the resonant thickness $H_{\rm res} \approx 85.2$ m.

model, a resonant thickness $H_{\rm res} \approx 85$ m. Figure 1 illustrates that an increase in the real part of h_2 can be seen even if $H_{\rm ocean}$ is several km. Thus, a static formulation would give a sufficiently accurate result only if $H_{\rm ocean} \gtrsim 100 H_{\rm res}$; a dynamical formulation should be used if $H_{\rm ocean} \lesssim 100 H_{\rm res}$.

4. Effect of a lid on tidal resonance

We then investigate the effect of varying lid parameters on the resonant configuration. Here, we use a very simple, incompressible three-layer Enceladus model, consisting of a viscoelastic shell, a liquid ocean, and an elastic mantle.

Figure 2 demonstrates the effect of a lid on the tidal resonance. If the shell thickness ($D_{\rm shell}$) is small or the shell viscosity ($\eta_{\rm ice}$) is moderate or high, there is always one resonant configuration (Figure 2 (c) and (d)). For a given $\eta_{\rm ice}$, an increase in $D_{\rm shell}$ leads to a smaller resonant ocean thickness. Because of non-zero rigidity, an icy shell acts as a membrane resisting deformation. This is similar in principle to surface tension acting at a liquid surface. The phase velocity of gravity waves taking surface tension into account is $\approx \sqrt{g H_{\rm ocean}\,(1 + Tk^2/\rho g)}$, where T is surface tension. Thus, an increase in T requires a decrease in $H_{\rm ocean}$ to lead to the same velocity.

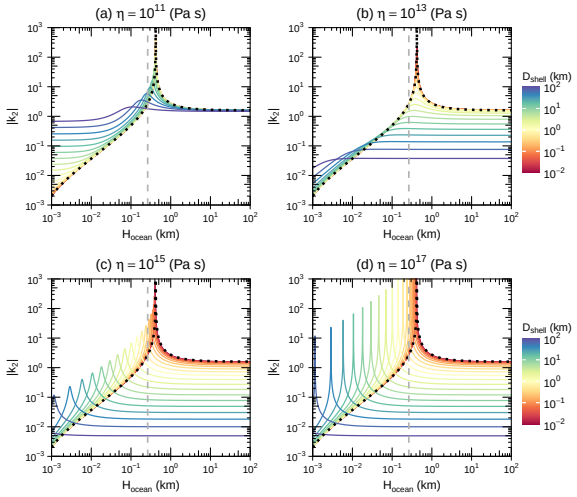

Figure 2: Absolute value of k_2 as a function of ocean thickness for an Enceladus model. The dotted curves are results for a surface ocean case ($D_{\rm shell} = 0$ km). The vertical dashed lines indicate the resonant thickness $H_{\rm res} \approx 263$ m.

5. Conclusions

We found that a dynamic ocean leads to a resonance while a static ocean does not. This resonance would be important for a satellite with a thin subsurface ocean since it would lead to significantly enhanced tidal heating in the solid lid. The static ocean formulation, which has been used in previous studies, would give an accurate Love number only if the ocean thickness is larger than the resonant thickness by a factor of about one hundred (or $\sim$10 km). A thicker or more rigid shell leads to a thinner resonant ocean thickness. These results highlight the importance of the effects of a solid lid for tidal dissipation in icy satellites with a subsurface ocean.

Acknowledgements

We thank J. Kimura, K. Matsumoto for fruitful discussions.

References

[1] Roberts and Nimmo, Icarus, 194, 675-689, 2008.

[2] Tyler, Nature, 456, 770-772, 2008.

[3] Moore and Schubert, Icarus, 166, 223-226, 2003.

EPSC Abstracts
Vol. 10, EPSC2015-867, 2015
European Planetary Science Congress 2015

Enceladus' long-period physical librations

B. Giese (1), N. Rambaux (2)
(1) DLR-Institute of Planetary Research, Berlin, Germany (Bernd.Giese@dlr.de), (2) IMCCE, Observatoire de Paris, Universite Pierre et Marie Curie, Paris, France.

Abstract

The predicted long-period librational response of Saturn's moon Enceladus [1] proceeds on the assumption that the spin pole is inertially fixed. Actually, the spin pole is expected to occupy a Cassini state [2] where it tracks the motion of the precessing orbit pole [3]. Here we show that this would result in additional long-period libration frequencies with appreciable amplitudes.

1. Orbit pole orientation

Enceladus' orbit pole precesses about the spin pole of Saturn at an average inclination of 0.0086° (Fig. 1). A frequency analysis reveals periodicities of 2.36 and 4.98 years suggesting that the precession is non-uniform.

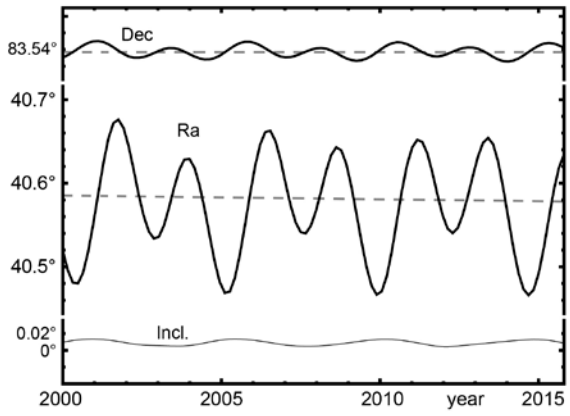

Figure 1: J2000 declination (Dec) and right ascension (Ra) of Enceladus' orbit pole determined from JPL ephemeris data [4]. Dashed lines indicate the orientation of Saturn's spin pole which averages the oscillating orbit pole orientation. The lower curve shows the inclination of the orbit pole to Saturn's spin pole. It varies between 0.0032° and 0.0139° at a mean value of 0.0086°.

2. Spin pole orientation

While uniform precession would, under stationary conditions, result in a coplanar configuration between Saturn's spin pole, Enceladus' orbit pole and its spin pole, non-uniform precession when fully damped drives the spin pole to a generalized Cassini state where each mode of the orbit pole precession has a corresponding mode of spin pole precession with rate and phase identical to the orbit modes but with different amplitudes [5]. However, as the spin precession rate parameter (see [5]) for Enceladus is ~9°/day and thus much higher than each orbit pole precession rate shown in Fig. 1, the resulting spin pole amplitudes must be close to those of the orbit pole and any obliquities thus must be close to zero, at least much smaller than the orbital inclination. Consequently, we have neglected any obliquities and assumed that the spin pole has the same dynamics as the orbit pole.

3. The librational response

With a perfect elliptical orbit and synchronous rotation Enceladus' long axis would, on a diurnal average, always point to Saturn. As Enceladus' orbit experiences strong perturbations notably by Dione this is no longer the case and torques by Saturn result which try to rotate Enceladus to compensate the misalignment. The degree of compensation (response) depends on the ratio of the free libration frequency to the frequencies of perturbation (forcing). For Enceladus, this ratio is on the order of 10^{-3} which implies that the (librational) response is in phase with the forcing and has the same amplitude. Thus to calculate the librational response of Enceladus we simply calculated the forcing under different conditions.

4. Results and discussion

In calculating the librational response we considered two rotational models: (i) the model of uniform rotation about a (inertially) fixed spin pole and (ii) the model of uniform rotation about a spin pole identical to the orbit pole (dynamic spin pole). Figure 2 shows the differences in the results: As expected, the librational response in case (ii) now includes the orbital periodicities of 2.36 and 4.98 years (§1), respectively. This leads to differences in the libration amplitudes of up to 0.1° as compared to case (i).

However, we note that our result here is based on the assumption that Enceladus' spin pole is fully damped. Only in that case a generalized Cassini state will be acquired [5]. Control point calculations as performed earlier [3, 6] may be used to verify the new results.

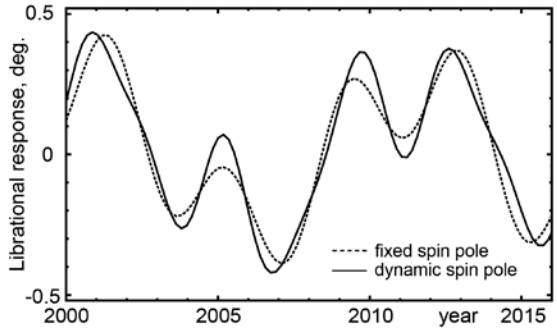

Figure 2: Predicted long period physical librations of Enceladus. The "fixed spin pole" result fully agrees with the results given in [1] (however with corrected parameter values [6] only).

References

[1] Rambaux, N.: Librational response of Enceladus, GRL, 37, L04202, doi:1029/2009GL041465, 2010.

[2] Chen, E.M.A. and Nimmo, F.: Obliquity tides do not significantly heat Enceladus, Icarus, 214, 779-781, 2011.

[3] Giese, B.: An upper limit of Enceladus' obliquity, EPSC, abstracts, Vol 9, 2014.

[4] Jacobson, R. A., 2014, http://naif.jpl.nasa.gov/pub/naif/generic_kernels/spk/satellites/sat365.bsp.

[5] Bills, B. G.: Free and forced obliquities of the Galilean satellites of Jupiter, Icarus, 175, 233-247, 2005.

[6] Giese, B. et al.: Enceladus: Evidence for librations forced by Dione , EPSC, abstracts, Vol 6, 2011.

EPSC Abstracts
Vol. 10, EPSC2015-881, 2015
European Planetary Science Congress 2015

EPSC
European Planetary Science Congress

Waves and eddies simulated by high-resolution Global Climate Modeling of Saturn's troposphere and stratosphere

A. Spiga[1], S. Guerlet[1], Y. Meurdesoif[2], M. Indurain[1], E. Millour[1], T. Dubos[1], M. Sylvestre[1,3], J. Leconte[4], T. Fouchet[3] [aymeric.spiga@upmc.fr] [1] Laboratoire de Météorologie Dynamique (UPMC/CNRS/X), Paris, France [2] Laboratoire des Sciences du Climat et de l'Environnement (CEA), Saclay, France [3] Laboratoire d'Études Spatiales et d'Instrumentation en Astrophysique (UPMC/CNRS), Meudon, France [4] Laboratoire d'Astrophysique de Bordeaux (CNRS), Floirac, France

Context The Cassini spacecraft, orbiting the Saturn's system since 2004, opened a new era for giant planets' exploration (1), and recently revealed that Saturn's hazy atmosphere is as dynamically active as Jupiter's colorful one. The longevity of the mission permitted a detailed analysis of tropospheric storms (2); an exceptionally detailed coverage of Saturn's great northern storm of 2010-2011, which eventually encircled the entire planet for months, and caused a sudden warming in the stratosphere (3); an assessment of the remarkable stability of the hexagonal polar jet (4); the seasonal monitoring of Saturn's equatorial oscillation (5), helping to build the analogy with the Quasi-Biennal Oscillation in the Earth's stratosphere (and a putative Quasi-Quadriennal Equatorial Oscillation in the jovian equatorial atmosphere). Those puzzling signatures in the stratosphere add to the outstanding questions related to the alternated jets structure in Saturn's troposphere: do jets' extent and forcing are deep in the interior, or confined to the weather layer? Are jets driven by sunlight or internal heat? Why such a strong prograde equatorial jet in Saturn?

Modeling challenges Based on the experience of telluric planets, the best step forward is to build a Global Climate Model for giant planets, obtained by coupling a solver for the Navier-Stokes equations for the atmospheric fluid on the sphere ("dynamical core") with realistic models for external forcings on the fluid: radiation, phase changes, chemistry ("physical packages"). Despite recent efforts which provided insights into the importance of wave-driven processes both in the troposphere and the stratosphere (6; 7; 8; 9), a Global Climate Model for giant planets complete enough to adress the theoretical challenges opened by observations is yet to emerge, for one or several of the following difficulties could not be overcome. ($\mathcal{D}_1$) ***Dynamical accuracy*** Through an inverse energy cascade named geostrophic turbulence, planetary-scale jets are forced by smaller-scale eddies arising from hydrodynamical instabilities. Relevant interaction scales (e.g. Rossby deformation radius) are 20° longitude on Earth but only 1° in giant planets, making eddy-resolving global simulations there 4 orders of magnitude more computationally expensive. ($\mathcal{D}_2$) ***Vertical extent*** Terrestrial experience shows that models need to extend from the troposphere to the stratosphere with sufficient vertical resolution to resolve the vertical propagation of waves responsible for large-scale structures in both parts of the atmosphere. ($\mathcal{D}_3$) ***Radiative computations*** The radiative transfer calculations necessary to predict the evolution of atmospheric temperature must be optimized for integrations over decade-long giant planets' years, while still keeping robustness against observations. ($\mathcal{D}_4$) ***Upper & lower boundaries*** Climate models do not extend deep enough to predict how tropospheric jets interact with interior convective fluxes and magnetic dynamo, and not high enough to model the photochemistry of key hydrocarbons impacting stratospheric winds and temperatures.

Our modeling efforts We started to build a Global Climate Model for Saturn which will be both versatile and powerful enough to overcome the four $\mathcal{D}_{1\rightarrow4}$ difficulties and address the outstanding questions and dynamical mysteries opened by Cassini and previous observational campaigns. Note that we leave apart here $\mathcal{D}_4$ which warrants further investigation on deep interior processes and upper atmosphere photochemistry. To address $\mathcal{D}_2$ and $\mathcal{D}_3$, we developed for Saturn an optimized seasonal radiative package validated against measurements (10). Our model's radiative computations are based on a versatile correlated-k method, suitable for any planetary composition (11) with k-coefficients derived from detailed line-by-line computations with the latest spectroscopic databases. The spectral discretization of the model was optimized for Saturn, with additional computations corresponding to this environment: aerosol layers, ring shadowing, internal heat flux. To address $\mathcal{D}_1$ and $\mathcal{D}_2$, we use

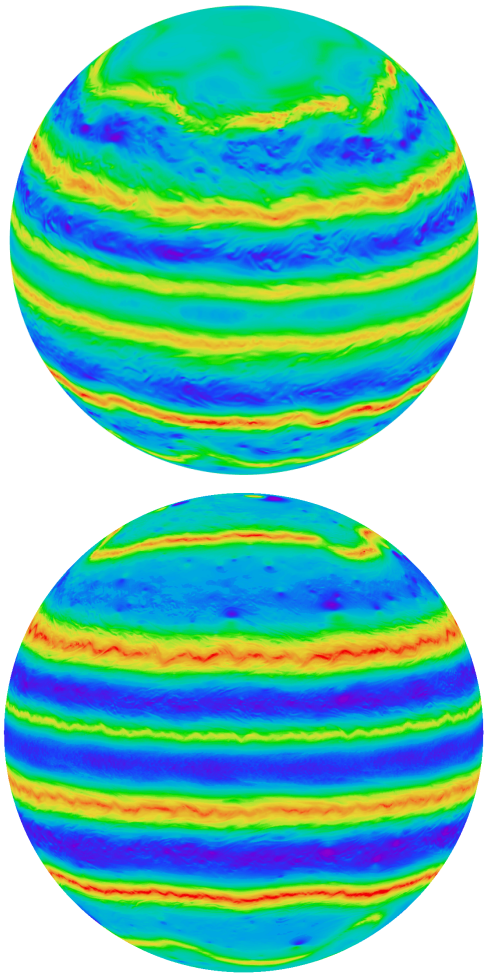

Figure 1: *Zonal winds predicted at 0.5 bar (yellow/red: prograde jets, blue/violet: retrograde jets) by our Global Climate Model for Saturn. Our simulations used the unprecedented horizontal resolutions of* $1/4^\circ$ *(top) and* $1/8^\circ$ *(bottom) longitude and* 64 *vertical levels from troposphere to stratosphere. In the top plot, jets' instabilities and filamentation can be noticed; in the bottom plot, the even finer horizontal resolution allows the model to reproduce the propagation of gravity waves on the flanks of the jets, as well as the possible emergence of traveling vortices (cf. blue/green spots in the northern hemisphere).*

DYNAMICO, developed in LMD as the next state-of-the-art dynamical core for Earth and planetary climate studies. DYNAMICO is tailored for massively parallel High-Performance Computing resources, thanks to an original icosahedral mapping of the planetary sphere which ensures excellent conservation and scalability properties up to 10^5 cores (12).

Results and perspectives An exceptional allocation on a new petaflops acquisition by the French inter-university computing center (CINES) allowed us to run our Global Climate Model for Saturn down to unprecedented resolutions of $1/4^\circ$ and $1/8^\circ$ (Figure 1). Our high-resolution Global Climate Model runs for Saturn show a detailed view into a striking variety of eddies and vortices, as well as the arising of alternated banded jets, the formation of a polar vortex, the deformation of the polar jet into polygonal structures (though not a stable hexagon). We will discuss during the EPSC conference the characteristics of both eddies and eddy-driven features, both in the troposphere (jets) and in the stratosphere (equatorial oscillations). Through spectral analysis, we determine the nature of the waves (Rossby, Kelvin, ...); through dynamical analysis, the instabilities which give birth to those disturbances (e.g. barotropic or baroclinic). We will describe how close our simulations are to the observed features by Cassini and other observational campaigns, and assess which processes are in need to be improved in our Global Climate Model. Our high-resolution simulations for Saturn not only open new perspectives for fundamental knowledge of atmospheric waves and instabilities, but also offer a step forward to the overarching goal of providing the community with a model capable to interpret past and future observations of gas giants' atmospheres.

Bibliography

[1] C. C. Porco, E. Baker, et al. Cassini Imaging Science: Initial Results on Saturn's Atmosphere. *Science*, 307:1243–1247, 2005.

[2] A. R. Vasavada, S. M. Hörst, et al. Cassini imaging of Saturn: Southern hemisphere winds and vortices. *Journal of Geophysical Research (Planets)*, 111:5004, 2006.

[3] L. N. Fletcher, B. E. Hesman, et al. Thermal Structure and Dynamics of Saturn's Northern Springtime Disturbance. *Science*, 332:1413–, 2011.

[4] A. Sánchez-Lavega, T. Río-Gaztelurrutia, et al. The long-term steady motion of Saturn's hexagon and the stability of its enclosed jet stream under seasonal changes. *Geophys. Res. Lett.*, 41:1425–1431, 2014.

[5] S. Guerlet, T. Fouchet, et al. Evolution of the equatorial oscillation in Saturn's stratosphere between 2005 and 2010 from Cassini/CIRS limb data analysis. *Geophys. Res. Lett.*, 38:9201, 2011.

[6] T. E. Dowling, M. E. Bradley, et al. The EPIC atmospheric model with an isentropic/terrain-following hybrid vertical coordinate. *Icarus*, 182:259–273, 2006.

[7] Y. Lian and A. P. Showman. Generation of equatorial jets by large-scale latent heating on the giant planets. *Icarus*, 207:373–393, 2010.

[8] J. Liu and T. Schneider. Mechanisms of Jet Formation on the Giant Planets. *Journal of Atmospheric Sciences*, 67:3652–3672, 2010.

[9] A. J. Friedson and J. I. Moses. General circulation and transport in Saturn's upper troposphere and stratosphere. *Icarus*, 218:861–875, 2012.

[10] S. Guerlet, A. Spiga, et al. Global climate modeling of Saturn's atmosphere. Part I: Evaluation of the radiative transfer model. *Icarus*, 238:110–124, 2014.

[11] R. D. Wordsworth, F. Forget, et al. Is Gliese 581d habitable? Some constraints from radiative-convective climate modeling. *Astron. Astrophys.*, 522:A22, 2010.

[12] T. Dubos, S. Dubey, et al. DYNAMICO, a hydrostatic icosahedral dynamical core designed for consistency and versatility. submitted to Geoscientific Model Development, doi:10.5194/gmdd-8-1749-2015, 2015.

EPSC Abstracts
Vol. 10, EPSC2015-893, 2015
European Planetary Science Congress 2015

"Blood Stains" on Tethys: Evidence for Recent Activity?

P. M. Schenk (1), B. J. Buratti (2), P. K. Byrne (1), W. B. McKinnon (3), F. Nimmo (4) and F. Scipioni (1)
(1) Lunar & Planetary Institute, Houston TX, (2) Jet Propulsion Lab, Pasadena, CA, (3) Washington Univ., Saint Louis, MO
(4) Univ. California, Santa Cruz, CA (schenk@lpi.usra.edu)

Abstract

A distinctive set of arcuate, reddish-colored lineaments has been identified on Tethys. These markings are slightly darker than adjacent cratered terrains but have a flatter green–IR spectral slope. The lineaments form an arcuate pattern centered on the tidal axis with Saturn. High-resolution image data show only the faintest traces of surface distortions, collocated with small, low-albedo spots <1 km in diameter. One possibility is that these markings may be nascent fractures, accompanied by relatively reddish discoloration from venting and deposition of material from the interior.

1. Introduction

Tethys is unusual among icy moons for its low bulk mean density of 0.985 g/cm^3, suggesting a low rock mass fraction and/or high porosity. Tethys also has an intense fracture history [1], including Ithaca Chasma as well as several hundred arcuate and linear troughs, grooves, and cracks. A distinctive set of linear features has been recognized on Tethys in areas viewed by Cassini under high solar illumination conditions (Fig. 1). These markings are characterized by a strong "reddish" color signature: a slightly lower albedo and flatter spectral signature in the green–IR range (Fig. 2).

1.1 IR-Lineations

There are at least three prominent sets in the northern anti-Saturn hemisphere, centered on the anti-Saturn meridian (Fig. 3). Each set consists of ~5–10 parallel lineations a few kilometers across and 50–250 km long. The lineations are remarkably curvilinear (i.e., non-sinuous), do not follow great circles, and are not deflected by major impact structures: they cross the floor of the 400-km-diameter, 8–10-km-deep Odysseus impact basin as if it were not there.

Although spatially limited, sub-Saturn hemispheric color imaging at low-phase angle clearly shows a similar set of arcuate, reddish lineations on that hemisphere, which is dusted by E-ring particles from Enceladus [2].

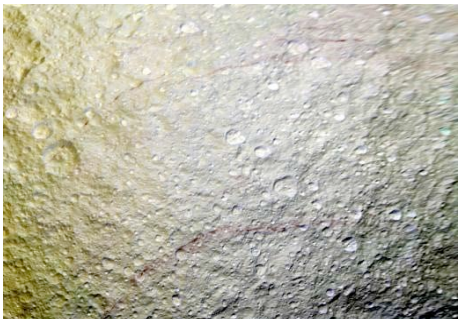

Figure 1: Color view of Tethys showing IR lineations (reddish arcs). Cassini IR3, green, UV3 composite.

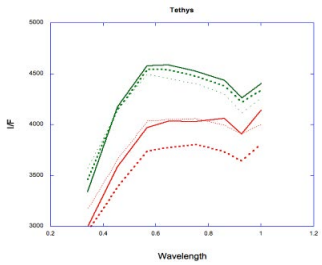

Figure 2: Spectral plot showing IR lineaments (red) and adjacent cratered plains (green).

One set of lineaments (~25° N, 185°W) has been imaged at high resolution. Mapping at ~90–125 m/pixel (Fig. 4) (together with stereo and lower resolution color imaging) shows no discrete scarp, ridge, or other tectonic manifestation along the ~100 km portion of the feature so imaged. Instead, a faint discoloration and intermittent distortion of the surface has been identified (Fig. 5). This set ignores topography. Further, 22 dark spots 200–800 m in diameter lie along this set of lineaments. These spots are characterized by very low albedos, sharp boundaries, and no evidence of raised rims consistent

with an impact origin. Of these 22, 60% (15) are situated at the bottom of impact craters.

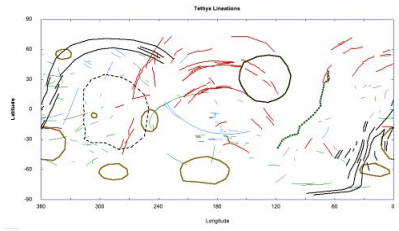

Figure 3: Global map of fractures, ridges, and lineations on Tethys. IR lineations are shown in red. Odysseus is circled at upper center.

2. Origin of IR-Lineaments

The spatial pattern of IR lineaments on Tethys shows a remarkable symmetry (Fig. 3), centered on the current tidal axis with Saturn. A lack of correlation with local geology might suggest an exogenic origin. Conversely, there are no rayed craters at the radial centers of these features. Further, the locations of the patterns on both the sub- and anti-Saturn hemispheres, and the lineaments' parallel orientations, argue against a disrupted comet origin (à la SL9). Hence we explore a possible endogenic origin.

Figure 4: High-resolution, 90 m/pixel mosaic of IR lineaments, merged with IR3–Gr–UV3 color mosaic.

The lineaments have no systematic orientation relative to Odysseus, indicating that stresses arising from the relaxation of that basin are not responsible for these features. Other stress mechanisms might have produced the pattern we observe. The IR lineaments match patterns of strain predicted to result from a non-synchronous rotation stress state, although this is unlikely for a cold, triaxial body like Tethys. The pattern less obviously fits a polar wander-induced stress state, but further testing of the proper rotation magnitude and path is required. Formation due to tidal recession stresses is another candidate scenario being tested.

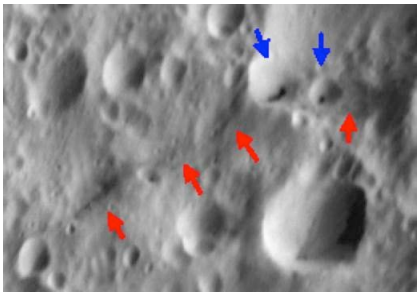

Figure 5: Enlargement of high-resolution view showing lineament (red arrows). Small dark spots are visible (blue arrows), which form within 10 km of the IR lineament.

The lack of obvious tectonic deformation despite the strong color signature is unusual (although features may exist below the current resolution limit). The lineaments could be reactivated ancient fractures, producing a temporal discoloration. At present there is no topographic or morphologic signature to support this. If tectonic, the lineaments might be still forming, with deformation only on a scale below that which we can resolve.

The coloration, and collocated dark spots, are consistent with active alteration of the surface, given that E-ring accumulation is expected to remove intrinsic color signatures in a geologically short time period. Low-volume but persistent outgassing and emplacement of volatiles from the interior, the colors of which are distinct from the evolved surface and/or result from exposure to the space environment, may be responsible. Differences in particle sizes of the outgassed material may add to this spectral distinctiveness.

References

[1]. Schenk, P., Moore J. M. Topography of Midsize Icy Satellites 2: Tethys and the Effects of Odysseus, Lunar Planet. Sci. Conf., 45, abstr. **2598.**

[2]. Schenk, P., D. Hamilton, R. Johnson, W. McKinnon, J. Schmidt, M Showalter, Plasma, plumes, and rings: Global color patterns on Saturn's midsize icy satellites, Icarus, 211, 740-757, 2011.